

Master of Science Thesis

---

# The Effect of Leading Edge Thickness on the Maximum Drag Coefficient of Airfoils at $90^\circ$ Angle of Attack

Experimental and Computational Analysis of Designed Profiles  
subjected to Extreme High Angles of Attack

M. Van Roosbroeck

---

September 10, 2014



# **The Effect of Leading Edge Thickness on the Maximum Drag Coefficient of Airfoils at 90° Angle of Attack**

**Experimental and Computational Analysis of Designed Profiles  
subjected to Extreme High Angles of Attack**

Master of Science Thesis

For obtaining the degree of Master of Science in Aerospace Engineering  
at Delft University of Technology

M. Van Roosbroeck

September 10, 2014



**Delft University of Technology**

Copyright © Aerospace Engineering, Delft University of Technology  
All rights reserved.

DELFT UNIVERSITY OF TECHNOLOGY  
DEPARTMENT OF AERODYNAMICS

The undersigned hereby certify that they have read and recommend to the Faculty of Aerospace Engineering for acceptance the thesis entitled **“The Effect of Leading Edge Thickness on the Maximum Drag Coefficient of Airfoils at 90° Angle of Attack”** by **M. Van Roosbroeck** in fulfillment of the requirements for the degree of **Master of Science**.

Dated: September 10, 2014

Supervisors:

---

Dr.ir. B.W. Van Oudheusden

---

Ir. W.A. Timmer

---

Dr.ir. A.H. van Zuijlen

---

Dr. D. Ragni



---

# Preface

With this thesis the master phase of my study Aerospace Engineering at the Delft University of Technology is concluded. I would like to thank all the people that supported me during my entire time at the university and without them I would not have been able to reach this goal. First of all, I would like to thank my parents and friends who made all of this possible and who have supported me in difficult times.

Secondly, I would like to express my gratitude to my supervisors Ir. Nando Timmer and Dr.ir. Sander van Zuijlen for there time, advice, support and patience during this project. Also I would like to thank Nicholas Balaesque and the staff of WindGuard who made it possible to conduct a second wind tunnel experiment in Bremerhaven. Furthermore my gratitude goes to all the technical staff at the low speed laboratory in Delft, especially to ing. Stefan Bernardy and Leo Molenwijk who assisted me during my wind tunnel experiments in Delft.

Michael Van Roosbroeck  
Delft, September 2014



---

# Summary

The need for energy is an ever increasing problem and most resources that are used today will be exhausted or no longer tolerated by the human kind in the future Omer (2008). Anticipating on the energy demand the development of wind turbines has taken a big leap and to improve the design process efficient and accurate aerodynamic modelling is required. During start-up, stopping and standstill of the turbine, the blades experience very high angles of attack. The flow physics behind this topic is not fully understood yet. In this research it is investigated what the relation is between the leading edge thickness of the airfoil and the maximum drag coefficient, this is done by means of experimental and numerical simulation.

For this investigation specially designed models are created to analyse the effect of the leading edge thickness. The parameter identifying the leading edge thickness is chosen to be the  $y/c$  ordinate at  $x/c = 0.0125$ . The models created will have a leading edge thickness ranging from zero (flat plate) to a maximum of 0.035 and have a chord length of 0.20 meter. All trailing edges are similar to a flat plate, with a constant thickness for the last 20% of the chord, such that only the effect of the leading edge is taken into account. The flat plate will be used as a reference since from literature it is known that the maximum drag coefficient is 1.96 - 2.01 depending on the source. Furthermore also the existing DU91-W2-250 model is used which is equipped with pressure orifices.

A first wind tunnel experiment is conducted in the Low Turbulence Tunnel (LTT) at the Delft Technical University. The designed models are connected to the balance system above the wind tunnel, this set-up implies two gaps at both ends are present and only one end is supported. As a consequence of the single support the Reynolds number is limited to 150 000. A second wind tunnel experiment is performed by WindGuard (WG) in Bremerhaven, their wind tunnel has the interesting characteristic of having the similar height (1.25 m) but a larger width (2.75 m) which has a big effect on the blockage correction that is needed afterwards. Furthermore, they also have the possibility to clamp the model at both sides which makes it possible to run the test at higher Reynolds numbers (up to 600 000). Besides the balance measurements of the designed models the DU91-W2-250 is tested at both facilities using the pressure orifices. The pressure data will be used to assess the effect of the Reynolds number on the aerodynamic characteristics and to validate the use of  $\theta = 0.96$  as Maskell correction factor, based in the aspect ratio.

From the wind tunnel tests it is concluded at first that there is no significant effect of the

Reynolds number on the aerodynamic characteristics in the deep stall region. This means that in general it is allowed to compare both wind tunnel tests in the deep stall region although the Reynolds number is different. Secondly, it is found for both tests that the maximum drag coefficient decreases linearly with increasing leading edge thickness. However, both wind tunnel experiments do not yield the same values. For the flat plate values of 1.95 and 2.01 are found after correction in the LTT and WG respectively which are in agreement with earlier investigations.

In addition to the wind tunnel experiment also CFD is used to investigate the relation between the leading edge thickness and the drag coefficient at  $90^\circ$  angle of attack based on force coefficients. Besides the force coefficients also pressure distributions and flow visualisations are used to explain why the drag reduces. Given that the CFD was not the main research area in this investigation only basic evaluations of different numerical settings are done like for example the mesh refinement and the preconditioning factor. In the end a 2D simulation is found to work the best with external boundary conditions. This means that no 3D effects are taken into account and that the flow is not bounded by a physical wall like in the wind tunnel. This eliminates the need for corrections but means that it only can be compared to the wind tunnel results after they are corrected. These two shortcomings in the CFD simulation are also given as recommendations for further research.

The CFD simulations confirm the linear decrease of the maximum drag coefficient with increasing leading edge thickness but more important are the flow visualisations and pressure distributions which explain why there is this decrease in drag coefficient. It is found that at the leading edge, facing the incoming wind, there is a suction force which increases with increasing leading edge thickness. It is this suction force that reduces the drag and increases the lift. Forward moving of the separation point is causing this increase in suction force.

Although in general a similar trend is found by the two wind tunnel experiments and the CFD simulations no identical results are obtained regarding the lift and drag coefficients. One reason that could cause the discrepancies is due to the blockage correction. A Maskell correction factor of 0.96 is used in the entire research based on the aspect ratio. However, from pressure measurements of the DU91-W2-250 it is derived that a value of 0.7 should be used in the LTT and this based on the base pressure and the uncorrected drag coefficients. Since no pressure data is available for the designed models it is not possible to determine the Maskell correction factor on the base pressure but only according to the aspect ratio. Therefore concerning the wind tunnel tests it would be recommended to equip the models with pressure orifices such that a better estimation can be done of the Maskell correction factor.

---

# Table of Contents

<b>Preface</b>	<b>v</b>
<b>Summary</b>	<b>vii</b>
<b>List of Figures</b>	<b>xiii</b>
<b>List of Tables</b>	<b>xvii</b>
<b>1 Introduction</b>	<b>1</b>
<b>2 Aerodynamic Characteristics at High Angles of Attack</b>	<b>3</b>
2.1 Flat Plate Theory . . . . .	3
2.1.1 Flow structure . . . . .	3
2.1.2 Aerodynamic Characteristics . . . . .	4
2.2 Prediction models . . . . .	6
2.2.1 Flat plate models . . . . .	6
2.2.2 AERODAS model . . . . .	8
2.3 Bluff body blockage correction . . . . .	13
2.3.1 Blockage effect . . . . .	13
2.3.2 Hackett and Cooper correction . . . . .	13
<b>3 Wind tunnel experiment</b>	<b>17</b>

3.1	Objectives . . . . .	17
3.2	LTT Windtunnel . . . . .	18
3.3	WindGuard . . . . .	19
3.4	Models . . . . .	20
3.4.1	DU91-W2-250 . . . . .	20
3.4.2	Design of models . . . . .	21
3.5	Measurement devices and data acquisition . . . . .	23
3.5.1	Dynamic pressure calibration curve . . . . .	23
3.5.2	Pressure tap measurement . . . . .	23
3.5.3	Balance system . . . . .	24
3.5.4	Data acquisition and handling . . . . .	24
<b>4</b>	<b>Experimental results</b>	<b>27</b>
4.1	DU91-W2-250 model . . . . .	27
4.1.1	Time averaged pressure measurement . . . . .	27
4.1.2	High speed data . . . . .	32
4.1.3	WindGuard . . . . .	33
4.2	DUT models . . . . .	35
4.2.1	Aerodynamic characteristics . . . . .	35
4.2.2	Leading edge thickness vs $C_{d_{max}}$ . . . . .	38
4.3	Comparison WindGuard data . . . . .	40
<b>5</b>	<b>CFD Analysis</b>	<b>45</b>
5.1	Theoretical Background . . . . .	46
5.1.1	Navier-stokes equations . . . . .	46
5.2	Computational Domain . . . . .	47
5.2.1	Domain . . . . .	47
5.2.2	Mesh . . . . .	48

5.3	Flow Solver . . . . .	50
5.3.1	Turbulence model . . . . .	50
5.3.2	Numerical parameters . . . . .	51
<b>6</b>	<b>CFD Results</b>	<b>53</b>
6.1	Evaluation of computational variables . . . . .	53
6.1.1	Mesh . . . . .	54
6.1.2	Preconditioning . . . . .	56
6.1.3	Boundary conditions . . . . .	58
6.1.4	Overview computational settings . . . . .	59
6.2	Force coefficients . . . . .	60
6.2.1	Flat plate . . . . .	60
6.2.2	DUT airfoils . . . . .	61
6.3	Flow analysis . . . . .	62
6.3.1	Pressure distribution . . . . .	63
6.3.2	Flow visualisation . . . . .	65
<b>7</b>	<b>Comparison Experiments - CFD</b>	<b>69</b>
7.1	DU91-W2-250 . . . . .	69
7.2	DUT airfoils . . . . .	70
7.2.1	Flat plate . . . . .	70
7.2.2	Leading edge thickness vs $C_{d_{max}}$ . . . . .	71
<b>8</b>	<b>Conclusion and Recommendations</b>	<b>75</b>
8.1	Conclusion . . . . .	75
8.2	Recommendations . . . . .	77
	<b>Bibliography</b>	<b>79</b>
<b>A</b>	<b>AERODAS</b>	<b>81</b>

<b>B</b>	<b>Maskell correction factor</b>	<b>85</b>
<b>C</b>	<b>Windguard</b>	<b>87</b>
<b>D</b>	<b>Meshes</b>	<b>91</b>
<b>E</b>	<b>Pressure along surface</b>	<b>93</b>

---

## List of Figures

2.1	Streamlines around a plate normal to the flow, Fail et al. (1957) . . . . .	4
2.2	Strouhal number vs angle of attack for various Re numbers, Chen and Fang (1996)	5
2.3	Ideal flat plate lift and drag coefficient . . . . .	5
2.4	Bulge effect Montgomerie (1996) . . . . .	7
2.5	Drag coefficient of wedges Hoerner (1965) . . . . .	7
2.6	Drag coefficient vs radius of rounded edge according to Montgomerie and Lindenburg	9
2.7	AERODAS model for lift and drag coefficient . . . . .	9
2.8	Lift and drag coefficient vs $\alpha$ , measurement and Aerodas model (NACA63215) .	11
2.9	Lift and drag coefficient vs $\alpha$ , measurement and Aerodas model (LS(1)-0417) . .	12
2.10	Lift and drag coefficient vs $\alpha$ , measurement and Aerodas model (DU96-W-180) .	12
2.11	Lift and drag coefficient vs $\alpha$ , measurement and Aerodas model (DU97-W-300) .	12
2.12	Comparison of separated flow corrections for 3D normal flat plates, AGARD-336. (1998) . . . . .	14
2.13	Comparison between the Maskell correction factor based on the aspect ratio (AR) and on the base pressure ( $C_p$ ), DU91-W2-250 at $Re = 5 \times 10^5$ . . . . .	15
3.1	Low Turbulence, Low speed windtunnel . . . . .	18
3.2	Side view of the WindGuard wind tunnel . . . . .	19
3.3	View from inside the test section of the wind tunnel at WindGuard . . . . .	20
3.4	DU91-W2-250 profile . . . . .	20

3.5	DUT models . . . . .	21
3.6	flat plate . . . . .	23
3.7	Schematic overview of the wind tunnel setup . . . . .	26
4.1	Uncorrected Lift, drag and moment coefficient of the DU91-W2-250 for Reynolds numbers $2 \times 10^5$ , $5 \times 10^5$ and $7 \times 10^5$ . . . . .	28
4.2	Uncorrected pressure distribution at $\alpha = -10^\circ$ , DU91-W2-250 . . . . .	29
4.3	Uncorrected pressure distribution for Reynolds numbers $2 \times 10^5$ , $5 \times 10^5$ and $7 \times 10^5$ 30	30
4.4	Uncorrected pressure coefficient DU91-W2-250 at $90^\circ$ . . . . .	31
4.5	Corrected lift and drag coefficient DU91-W2-250, at $Re = 2 \times 10^5$ , $5 \times 10^5$ and $7 \times 10^5$ 31	31
4.6	High speed data and fourier transform . . . . .	32
4.7	Strouhal number for DU91-W2-250 at $Re = 2 \times 10^5$ and $5 \times 10^5$ . . . . .	33
4.8	Force coefficient DU91-W2-250 based on balance and pressure measurements, $Re = 5 \times 10^5$ . . . . .	33
4.9	Pressure distribution at $90^\circ$ angle of attack according to the LTT ( $Re = 5 \times 10^5$ ) and WG ( $Re = 6 \times 10^5$ ), DU91-W2-250 . . . . .	34
4.10	Experimental and theoretical flat plate drag and lift coefficient, $Re = 1.5 \times 10^5$ . . . . .	36
4.11	Corrected lift and drag coefficient in deep stall region for the DUT models, $Re = 1.5 \times 10^5$ . . . . .	37
4.12	Corrected moment coefficients of all the models, $Re = 1.5 \times 10^5$ . . . . .	38
4.13	Lift and drag coefficient at $90^\circ$ angle of attack in relation to the leading edge thickness , $Re = 1.5 \times 10^5$ . . . . .	39
4.14	Flat plate data from WindGuard ( $Re = 6 \times 10^5$ ), LTT ( $Re = 1.5 \times 10^5$ ) and Ideal flat plate theory . . . . .	41
4.15	The effect of one gap on the lift and drag coefficient of the flat plate, $Re = 6 \times 10^5$ 42	42
4.16	Lift and drag coefficient of the DUT-20-25, WindGuard ( $Re = 6 \times 10^5$ ) and LTT ( $Re = 1.5 \times 10^5$ ) . . . . .	43
4.17	The lift and drag coefficient at $90^\circ$ angle of attack in relation to the leading edge thickness according to: WindGuard ( $Re = 6 \times 10^5$ ) , LTT ( $Re = 1.5 \times 10^5$ ) . . . . .	44
5.1	Extend of modelling for certain type of models Hossain (2012) . . . . .	46

5.2	Computational domain and triangulation . . . . .	48
5.3	Mesh . . . . .	49
6.1	Pressure distribution at 90° angle of attack for different setting of preconditioning (Including reference of measurement Fage et al. (1927)) . . . . .	55
6.2	Pressure distribution and residual of a flat plate at 90° angle of attack for different setting of preconditioning (Including reference of measurement Fage et al. (1927)) . . . . .	57
6.3	Pressure distribution of a flat plate at 90° angle of attack for different boundary conditions . . . . .	58
6.4	Theoretical and numerical lift and drag coefficient for the flat plate, $Re = 1.5 \times 10^5$ . . . . .	61
6.5	Lift and drag coefficient vs the leading edge thickness, $Re = 1.5 \times 10^5$ . . . . .	62
6.6	Pressure distribution for all the DUT airfoils, AOA = 90° . . . . .	63
6.7	Pressure distribution along the surface contour, $Re = 1.5 * 10^5$ . . . . .	65
6.8	streamlines around the DUT-10-35 . . . . .	66
6.9	Streamlines near the leading edge for different profiles . . . . .	68
7.1	Corrected pressure distribution at 90° angle of attack according to LTT ( $Re = 5 \times 10^5$ ), WG ( $Re = 5 \times 10^5$ ) and CFD ( $Re = 6 \times 10^5$ ) for the DU91-W2-250 profile . . . . .	70
7.2	Lift and drag coefficient based on the wind tunnel measurements, Ideal flat plate theory and CFD . . . . .	71
7.3	Lift and drag coefficient with respect to the leading edge thickness based on wind tunnel measurements and CFD . . . . .	72
A.1	AERODAS max drag coefficient for various airfoil thickness and AR Spera (2008) . . . . .	83
A.2	post-stall lift coefficient for different aspect ratios Spera (2008) . . . . .	84
B.1	Effect of the Maskell correction factor on the Pressure coefficient of the DU91-W2-250 at an AOA of 90°, $Re = 5 \times 10^5$ . . . . .	85
C.1	Lift coefficient for all DUT airfoils from WG ( $Re = 6 \times 10^5$ ) and LTT ( $Re = 1.5 \times 10^5$ ) . . . . .	88
C.2	Drag coefficient for all DUT airfoils from WG ( $Re=6 \times 10^5$ ) and LTT ( $Re=1.5 \times 10^5$ ) . . . . .	89
C.3	Moment coef. for all DUT airfoils from WG ( $Re=6 \times 10^5$ ) and LTT ( $Re=1.5 \times 10^5$ ) . . . . .	90

---

D.1	Coarse mesh . . . . .	91
D.2	Medium mesh . . . . .	91
D.3	Mesh with wake refinement . . . . .	92
D.4	Mesh 4 . . . . .	92
E.1	Pressure distribution along the surface contour, $Re = 1.5 \times 10^5$ . . . . .	93
E.2	Pressure distribution along the surface contour, $Re = 1.5 \times 10^5$ . . . . .	94

---

## List of Tables

2.1	Aerodas parameters . . . . .	11
4.1	Overview of $C_{d,max}$ and $C_l@90^\circ$ for different airfoils Timmer (2010) . . . . .	38
4.2	Overview of $C_{d,max}$ and $C_l@90^\circ$ for the DUT models . . . . .	39
4.3	Drag coefficient for the flat plate and drag reduction according to W.A. Timmer, LTT and WindGuard . . . . .	44
6.1	Effect of mesh on the lift and drag coefficient at $90^\circ$ , DU91-W2-250 . . . . .	56
6.2	Input parameters for the numerical simulations . . . . .	60
6.3	Lift and drag coefficient from front and rear surface separate . . . . .	64
7.1	Drag coefficient for the flat plate and drag reduction according to W.A. Timmer, LTT, WindGuard and CFD . . . . .	73



---

# Nomenclature

## Symbols

<b>Symbol</b>	<b>Description</b>	<b>Units</b>
$\alpha$	Angle of attack	[°]
$\beta$	Control angle	[°]
$\beta$	Preconditioning factor	[-]
$\gamma$	'Camber' angle	[°]
$\epsilon$	Wedge angle	[°]
$\epsilon$	Dissipation rate	[ $m^2/s^2$ ]
$\mu$	Dynamic viscosity	[kg/ms]
$\nu$	Kinematic viscosity	[ $m^2/s$ ]
$\mu_t$	Turbulent eddy viscosity	[kg/ms]
$\theta$	Maskell blockage correction factor	[-]
$\phi$	Angle of the balance system	[°]
$\Phi$	Streamline	[-]
$\rho$	Density	[ $kg/m^3$ ]
$\tau_{ji}$	Stress tensor	[ $kg/ms^2$ ]
$A$	Half length of the horizontal axis of an ellipse	[m]
$A_0$	Angle of attack at which $CL_1 = 0$	[°]
$ACL_1$	Angle of attack at maximum pre-stal lift	[°]
$ACD_1$	Angle of attack at maximum pre-stall drag	[°]
$b$	Characteristic length	[m]
$b_f$	Corner fillet width	[m]
$B$	Half length of the vertical axis of an ellipse	[m]
$c$	Chord	[-]
$C$	Cross-sectional area for the test section	[ $m^2$ ]
$C_\mu$	Empirical constant	[-]
$C_d$	Drag coefficient	[-]
$C_{D_c}$	Corrected drag coefficient	[-]
$C_{D_u}$	Uncorrected drag coefficient	[-]

$C_l$	Lift coefficient	[-]
$C_{D_cM1}$	Corrected drag coefficient including the wake distortion	[-]
$\Delta C_{DM}$	Drag increment due to the wake distortion	[-]
$C_n$	Normal force coefficient	[-]
$C_p$	Pressure coefficient	[-]
$C_{pb}$	Base pressure coefficient	[-]
$C_{p,l}$	Lower surface pressure coefficient	[-]
$C_{p,u}$	Upper surface pressure coefficient	[-]
$C_t$	Tangential force coefficient	[-]
$CL1$	Lift coefficient in the pre-stall regime	[-]
$CL1max$	Maximum pre-stall lift coefficient, at $\alpha = ACL1$	[-]
$CL2$	Lift coefficient in the post-stall regime	[-]
$CD0$	Minimum drag coefficient, at $\alpha = A0$	[-]
$CD1$	Drag coefficient in the pre-stall regime	[-]
$CD1max$	Maximum pre-stall drag coefficient	[-]
$CD2$	Drag coefficient in the post-stall regime	[-]
$CD90$	Drag coefficient at 90 degree angle of attack	[-]
$CD2D$	2D drag coefficient of flat pate according to Hoerner	[-]
$CD3D$	3D drag coefficient of flat pate according to Hoerner	[-]
$f$	Frequency	[Hz]
$h$	Tunnel height	[m]
$h_{eq}$	Equivalent tunnel height	[m]
$h_f$	Corner fillet height	[m]
$k$	Turbulent kinetic energy	[ $m^2/s^2$ ]
$p$	Pressure	[ $N/m^2$ ]
$p_0$	Static free-stream pressure	[ $N/m^2$ ]
$\Delta P_b$	Wind tunnel control pressure	[ $N/m^2$ ]
$q_0$	Dynamic pressure of the free-stream	[ $N/m^2$ ]
$q_c$	Corrected dynamic pressure	[ $N/m^2$ ]
$q_u$	Uncorrected dynamic pressure	[ $N/m^2$ ]
$r$	Radius	[m]
Re	Reynolds number	[-]
$S$	Aera of the model	[ $m^2$ ]
$S1$	Slope of linear segment of the pre-stall lift curve	[1/deg]
St	Strouhal number	[-]
$t$	Thickness	[m]
$t$	Time	[sec]
$T_u$	Turbulence intensity	[-]
$u_i$	Instantaneous velocity component	[m/s]
$u_i'$	Fluctuating velocity component	[m/s]
$u_\tau$	Friction velocity	[m/s]
$U_i$	Time averaged velocity component	[m/s]
$U_{ref}$	Free-stream velocity	[m/s]
$V_0$	Free-stream velocity	[m/s]
$y$	Distance form the airfoil's surface	[m]
$y^+$	Non-dimensional distance from the wall	[-]

**Acronyms**

2D	Two dimensional
3D	Three dimensional
AOA	Angle of attack
AR	Aspect ratio
CAD	Computer-aided design
CFD	Computational fluid dynamics
CFL	Courant-Friedrichs-Lewy
LE	Leading edge
LES	Large eddy simulation
LTT	Low turbulence tunnel
RANS	Reynolds averaged Navier-Stokes
StC	Stall coefficient
WG	WindGuard



---

# Chapter 1

---

## Introduction

The need for energy is an ever increasing problem and most resources that are used today will be exhausted or no longer tolerated by the human kind in the future Omer (2008). Sustainable energy remains a hot topic all over the world and wind power is until today still one off the best known, most widely applied forms of sustainable energy and in the future even more use will be made of wind power. Wind turbines will become part of our environment and to use them to the maximum of their capabilities full understanding of the forces is required. Anticipating on the energy demand the development of wind turbines has taken a big leap and to improve the design process efficient and accurate aerodynamic modeling is required. During start-up, stopping and standstill of the turbine, the blades experience very high angles of attack. The flow physics behind this topic are not fully understood yet. In the past research is performed on the relation between the thickness of the leading edge and the drag coefficient at 90 degrees. Ostowari and Naik (1985) performed wind tunnel experiments and Montgomerie (1996) and Lindenburg (2003) both established empirical relations based on flat plates and bluff bodies to describe the effect of the nose rounding on the drag coefficient. It is however found that testing at such high angles of attack goes together with high blockage ratios and fluctuating forces which makes it prone to errors.

The goal of this project is to redo this investigation with custom made profiles to identify the effect of the leading edge thickness on the maximum drag coefficient in a systematic way. The leading edge thickness is defined as the  $y/c$  ordinate at  $x/c = 0.0125$ , as it is defined by Timmer (2010). The research will be done based on measurements performed in two different wind tunnels (one at the Technical University of Delft and the other one at WindGuard, a german company). Different models are designed with increasing leading edge thickness starting from a flat plate which will be used as a reference to a maximum of 0.035. Furthermore an attempt is made to use CFD which will give the opportunity to create flow visualization and pressure distribution. The research question is thus to identify and explain the effect of the leading edge thickness on the drag coefficient of an airfoil at  $90^\circ$  angle of attack.

In total 8 chapters are present in this report. It starts with a general introduction about flow behaviour around a flat plate inclined vertically to the wind, furthermore some existing relations that express the influence of the leading edge thickness to the maximum drag coefficient are discussed. The introducing chapter concludes with a short overview of the blockage correction method according to Hackett and Cooper. The third chapter explains the wind tunnel test, set-up and measurements techniques together with the design of some specific profiles. The results of these wind tunnel tests are then discussed in chapter 4. In chapter 5 the basics behind the CFD computation are explained while in chapter 6 the results are given. A comparison between the CFD results and the wind tunnel results is given in chapter 7. Then finally in the last chapter a conclusion and some recommendations are given.

---

## Chapter 2

---

# Aerodynamic Characteristics at High Angles of Attack

Airfoils in deep stall behave differently than in case when the flow is fully attached. Testing of airfoils in deep stall also requires extra caution regarding the corrections. In this introducing chapter an overview is given of typical flow phenomena and existing models to predict the drag coefficient in deep stall. Furthermore also the Hackett and Cooper correction method, used for blockage correction, is shortly explained.

### 2.1 Flat Plate Theory

For airfoils positioned at high angles of attack and especially at 90 degrees angle of attack there is a good resemblance with a flat plate inclined vertically to the flow. More research is performed by [Fail et al. \(1957\)](#); [Viterna et al. \(1981\)](#); [Hoerner \(1965\)](#) on flat plates and therefore it is useful as a reference to validate the later results. In this section the flow structure behind a flat plate (or a bluff body in general) is described together with the aerodynamic characteristics.

#### 2.1.1 Flow structure

Airfoils or flat plates positioned at high angles of attack (Fully separated upper surface) show strong resemblance with a bluff body. For bluff bodies the drag force it is mainly originating from pressure drag rather than from viscous drag which means that a strong wake is present behind the body. In case of an airfoil or flat plate this is also the case. An investigation by [Fail et al. \(1957\)](#) shows that the flow is characterised by a bubble behind the plate, see figure 2.1.

The bubble is closed by a so called "bubble boundary" indicated by streamline  $\Phi = 0$ . Inside this bubble a circular flow is present causing variation in static pressure. Outside the bubble boundary there is a wake boundary, in between these two boundaries a so called vortex street grows.

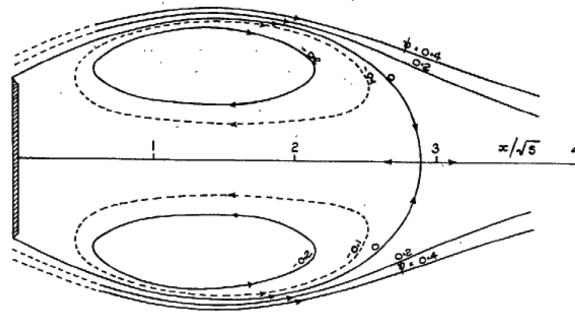


**Figure 2.1:** Streamlines around a plate normal to the flow, Fail et al. (1957)

This vortex street is caused due to unstable vortices which roll up at each side of the plate. The vortex shedding is a repetitive phenomena which happens alternately from the top and the bottom. This happens with a certain shedding frequency ( $f$ ) for a given object with characteristic length ( $b$ ) and submerged in a flow with a given free stream velocity ( $V_0$ ). A non-dimensional number, called the Strouhal number ( $St$ ), can be introduced which gives the relation between the convective time scale (determined by the free stream velocity) and the time scale of the unsteady fluctuations (determined by the shedding frequency) (Scarano, 2012). It is also given that steady flow is characterised by a small Strouhal number while strongly unsteady flow results in a large Strouhal number.

$$St = \frac{fb}{V_0} \quad (2.1)$$

It is shown by Fage et al. (1927) that the free stream velocity is directly proportional to the shedding frequency, this results in a constant Strouhal number at a certain angle for various airspeeds. They also show that the Strouhal number decreases with increasing angle of attack ( $\alpha$  up to  $90^\circ$ ). A more recent investigation by Chen and Fang (1996) shows the influence of low range Reynolds number on the Strouhal number ( $Re$  up to 32000). The effect of the  $Re$  number on the Strouhal number (characteristic length is the chord) for an inclined flat plate can be seen in figure 2.2

It can be seen that for angle of attack larger than  $40^\circ$  there is no effect at all from the Reynolds number on the Strouhal number. Furthermore, it is found that the influence of the angle of attack is strongly reduced in the deep stall region.

## 2.1.2 Aerodynamic Characteristics

Given the earlier research the flat plate will be used as a reference to validate the wind tunnel test and CFD calculation. Besides earlier research also the ideal flat plate theory, given by

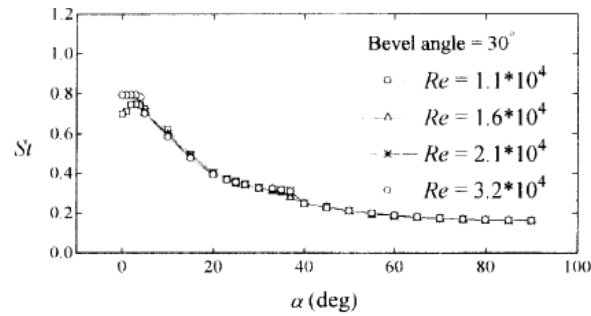


**Figure 2.2:** Strouhal number vs angle of attack for various Re numbers, [Chen and Fang \(1996\)](#)

[Hoerner \(1965\)](#) will be used as a mean of validation. The equations governing the ideal flat plate theory are given below.

$$C_l = 2 * \sin\alpha * \cos\alpha \quad (2.2a)$$

$$C_d = 2 * \sin^2\alpha \quad (2.2b)$$

In the literature ([Lindenburg \(2003\)](#)) many different values for the maximum drag coefficient of a flat plate normal to the flow are given. [Hoerner \(1965\)](#) gives 1.98 while [Viterna et al. \(1981\)](#) gives a value of 2.01 and other references show even higher values going up to 2.06 [Ostowari and Naik \(1984\)](#) for the maximum drag coefficient. According to the ideal flat plate theory the maximum drag coefficient is equal to two.

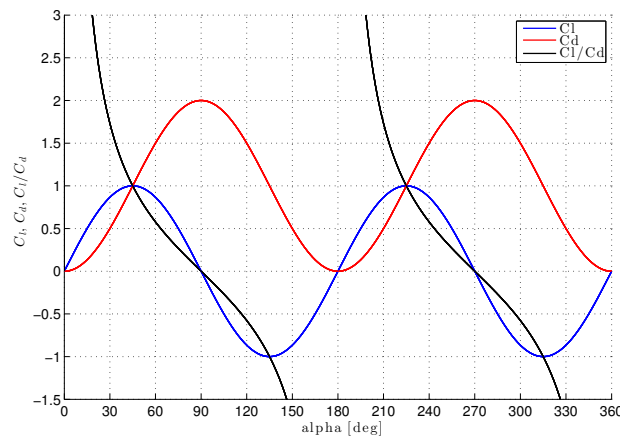


**Figure 2.3:** Ideal flat plate lift and drag coefficient

In figure 2.3 it can be seen that the maximum drag coefficient is achieved at  $90^\circ$  angle of attack and the lift coefficient at this point is zero. Furthermore it is shown that the drag coefficient is symmetric around 90 degrees while the lift coefficient is anti-symmetric. It should be noted that the drag coefficient reduces to zero at  $0^\circ$  which means that no viscous effects are taken into account.

## 2.2 Prediction models

In this section different models or techniques are discussed which are established in the past to estimate the effect of geometrical characteristics on the drag coefficient at 90° angle of attack or in the deep stall region. First the models of Montgomerie and Lindenburg are discussed, both are based on investigations by Hoerner (1965) on bluff bodies. Afterwards the AERODAS model by Spera (2008) is treated which is based on experimental data of airfoils.

### 2.2.1 Flat plate models

Due to the resemblance between airfoils in deep stall and flat plates researchers have developed models using these 2D drag and lift coefficients of flat plates to estimate the drag coefficients for airfoils.

Montgomerie (1996) is one of those researchers that used the flat plate coefficients. The goal of his developed model is to estimate the drag coefficient distribution over a wing at 90 degrees to the wind. In order to do so Montgomerie makes use of Hoerner (1965) data and created a curve which is described by the following equation:

$$CD_{90} = CD_{3D} + (CD_{2D} - CD_{3D}) * e^{-20(c/b)} \quad (2.3)$$

Where  $CD_{90}$  is the drag coefficient of an airfoil at 90° angle of attack with a certain aspect ratio ( $b/c$ ),  $CD_{2D}$  and  $CD_{3D}$  are the 2D and 3D drag coefficients of a flat plate according to Hoerner (1.98 and 1.17 respectively) and  $c/b$  is the inverted aspect ratio.

Of course there are differences between wind turbine blades and a flat plate, even at 90° angle of attack, some of these differences and their effect on the drag coefficient are also discussed by Montgomerie. Given the goal of this investigation only the effect of a rounded leading edge and bulge are discussed.

The effect of the rounded leading edge is determined using three objects with significant different leading edge shape. The characteristic determining the rounded leading edge is chosen to be  $r/c$ , the radius of the rounded leading edge over the chord length. The three objects (flat plate, oval, and cylinder) have a  $r/c$  of 0, 0.25 and 0.5 and have a drag coefficient of 1.98, 1.6 and 1.17 respectively. These objects have both edges rounded which results in more drag reduction. In case only the leading edge is rounded Montgomerie gives the following reduction in drag at 90 ° angle of attack.

$$\Delta C_{d,RoundedLE} = -0.83 \frac{r_{LE}}{c} \quad (2.4)$$

A second geometrical characteristic that has an effect on the drag coefficient is the bulge effect. In figure 2.4 the bulge is identified as interpreted by Montgomerie. The right hand side

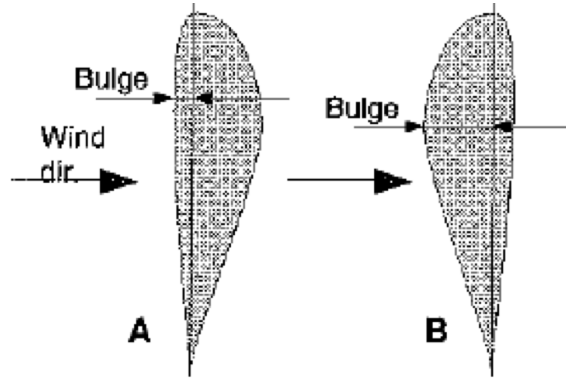


Figure 2.4: Bulge effect [Montgomerie \(1996\)](#)

of the figure shows a larger bulge in the direction of the flow, which according to [Montgomerie](#) prepares the flow better to go around the leading edge and therefore reduces the drag. A clear relation between bulge and drag could however not be established due to the lack of data. Furthermore it is possible that the bulge and the rounded leading edge are effected by each other since in order to have a certain amount of bulge a minimum nose radius is required. Another empirical model is created by [Lindenburg \(2003\)](#) and implemented in the so-called StC (Stall Coefficient) program. Based on [Hoerner's](#) investigation about bluff bodies, [Lindenburg](#) started with concluding that the downwind side does not significantly influence the drag coefficient if it does not extend deep into the wake. For simplicity [Lindenburg](#) takes a drag coefficient of 2 for a flat plate normal to the flow based on values from [Hoerner \(1965\)](#), [Ostowari and Naik \(1984\)](#) and [Viterna et al. \(1981\)](#). In addition to this flat plate coefficient [Lindenburg](#) provides us with a formula to include a certain wedge angle. This angle has the same effect on the trailing and leading edge. The effect of a wedge angle is in the past investigated by [Hoerner \(1965\)](#) and the result can be seen in figure 2.5. For  $\epsilon = 90^\circ$  (normal flat plate) the value of 1.98 is found, smaller angles result in a lower drag coefficient.

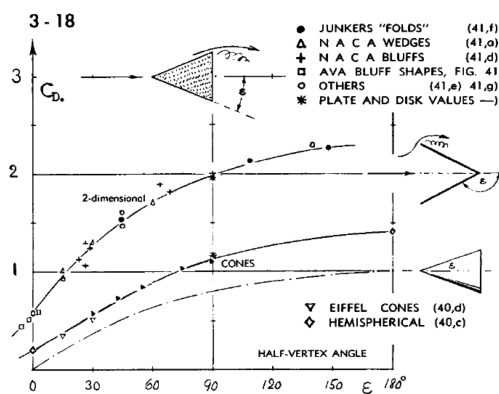


Figure 2.5: Drag coefficient of wedges [Hoerner \(1965\)](#)

[Hoerner](#) gives a mathematical expression to determine the influence of the wedge angle of a triangle.

$$C_d = 1.98 - 0.4\gamma - 0.16\gamma^2 \tag{2.5}$$

The variable parameter  $\gamma$  is related to the wedge angle by the following relation:  $\gamma = 90^\circ - \epsilon$ . So in case when  $\epsilon = 90^\circ$  (flat plate)  $\gamma$  becomes zero and the drag coefficient returns to the original 2D flat plate value.

Lindenbug modified this expression to make it possible to use it for airfoils by dividing the wedge angle in two parts so that the leading edge and trailing edge both can have their own angle. These angles can simulate the camber of the airfoil. Equation 2.5 now becomes:

$$C_d = 2 - 0.2(\gamma_{nose} + \gamma_{tail}) - 0.08(\gamma_{nose}^2 + \gamma_{tail}^2) \quad (2.6)$$

Lindenbug (2003) also provides a way to deal with the (leading) edge radius. It is assumed that the trailing edge is sharp and that the flow leaves the airfoil in a well defined direction while the rounded leading edge causes an amount of suction, deflecting the flow more downwards which would lead to a reduction in drag.

Based on measurements of different bluff bodies with different radii (Hoerner) Lindenbug established an expression to determine the drag including the effect of an oval-type edge radius.

$$C_d = 1.98(1 - 0.4(r_{nose} + r_{tail})/c) \quad (2.7)$$

The nose radius of an airfoil is more of an elliptical shape and according to Lawson et al. (1979) the drag reduction for relative flat ellipses is stronger than for the oval-type as described by Hoerner. Assuming a sharp trailing edge Lindenbug uses the following expression in his StC program.

$$C_d = 1.7 + (0.3 - \gamma_{nose}(0.2 + 0.08\gamma_{nose})) * (1 - 1.8\sqrt{r_{nose}/c}) - \gamma_{tail}(0.2 + 0.08\gamma_{tail}) \quad (2.8)$$

In order to compare Lindenbug's results with Montgomerie's method it is assumed that there is no camber ( $\gamma = 0$ ). This reduces equation 2.8 to:

$$C_d = 1.7 + 0.3 * (1 - 1.8\sqrt{r_{nose}/c}) \quad (2.9)$$

In figure 2.6 the difference between the two methods is depicted. It can be observed that Lindenbug expects more drag reduction due to a rounded edge than Montgomerie up to a nose radius which is 45 % of the chord. Montgomerie also expects a linear decrease while Lindenbug expects a stronger reduction for the smaller radii.

## 2.2.2 AERODAS model

In the beginning of this section it is shown that Lindenbug and Montgomerie both established a model to determine the drag coefficient of an airfoil at  $90^\circ$  angle of attack based on flat plate theory and bluff body data. Spera (2008) discusses a more advanced model to determine the drag and lift coefficient of airfoils over a wide range of angles of attack. The main difference with the two previous models is that this model is based on real airfoil data rather than flat plate theory in the deep stall region. The aerodynamic coefficients in the pre-stall and post-stall regimes are modelled separately, as function of the angle of attack. In figure 2.7(a) the lift model is illustrated and determined according to the following expressions.

$$If \alpha \geq A_0 : CL = max(CL1, CL2) \quad (2.10a)$$

$$If \alpha < A_0 : CL = min(CL1, CL2) \quad (2.10b)$$

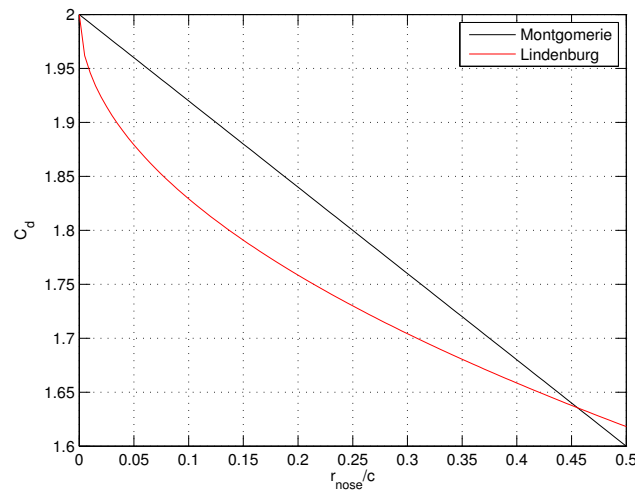
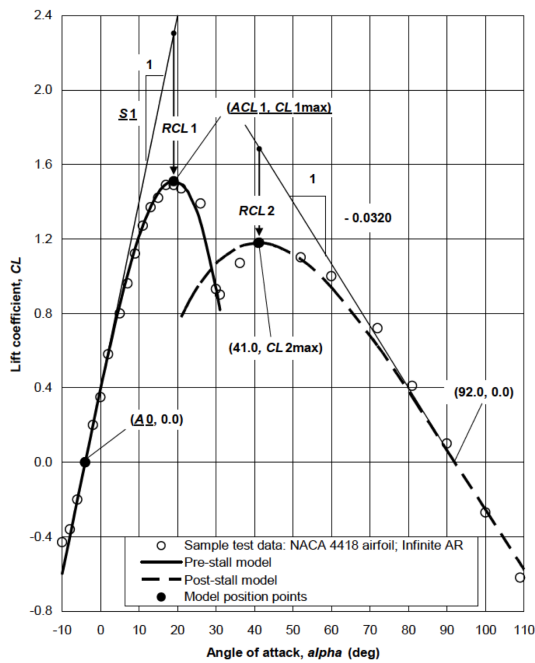


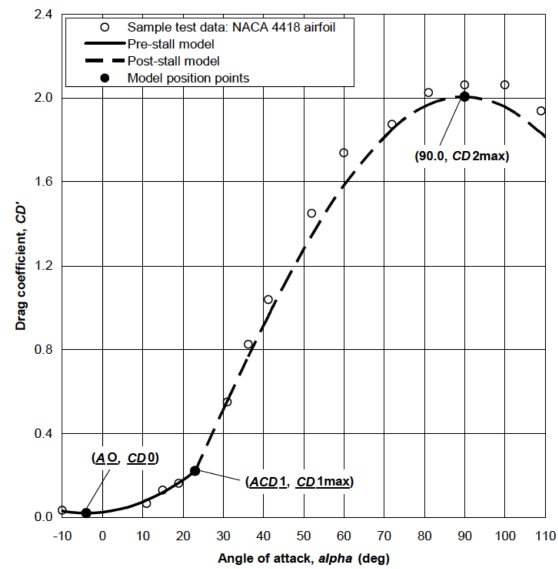
Figure 2.6: Drag coefficient vs radius of rounded edge according to Montgomery and Lindenburg

The model for the drag coefficient is illustrated in figure 2.7(b), determined as follows.

$$If \alpha < A0 : CD = max(CD1, CD2) \tag{2.10c}$$



(a) Lift coefficient model Spera (2008)



(b) Drag coefficient model Spera (2008)

Figure 2.7: AERODAS model for lift and drag coefficient

where

- A0 Angle of attack at which  $CL1 = 0$
- CL1 Lift coefficient in the pre-stall regime

CL2	Lift coefficient in the post-stall regime
CD1	Drag coefficient in the pre-stall regime
CD2	Drag coefficient in the post-stall regime

In figure 2.7 seven parameter are underlined, these are the required input parameters which are:

A0	angle of attack at which $CL1 = 0$
ACL1'	angle of attack at maximum pre-stall lift(deg)
CL1max'	maximum pre-stall lift coefficient, at $\alpha = ACL1'$
S1'	slope of linear segment of pre-stall lift curve (1/deg)
CD0	minimum drag coefficient; at $\alpha = A0$
ACD1'	angle of attack at maximum pre-stall drag (deg)
CD1max'	maximum pre-stall drag coefficient; at $\alpha = ACD1'$

The prime indicates that the parameter is sensitive to aspect ratio changes, the value for the infinite aspect ratio is here designated. Five of the seven parameter are dependent on the aspect ratio and need to be adjusted before the model can be used for finite aspect ratio airfoils. Many reference values for aerodynamic coefficients are given for infinite aspect ratio airfoils, this results in no exposed tips that can effect the flow over the span. In order to use this data for finite aspect ratio airfoils it needs to be modified. Spera bases his approach on the method given by Jacobs and Anderson (For the aspect ratio adjustment see [Spera \(2008\)](#)). In the Post-stall regime our attention will go to the maximum drag at  $90^\circ$  angle of attack, and the corresponding lift.

In the pre-stall region Cl and Cd are based on the input parameters that are given above, which are experimentally determined for each airfoil individually. The equations used for Cl1 and Cd1 can be found in the work of Spera. The post-stall coefficients CL2 and CD2 are based among others on CD2max and CL2max. These two parameters are determined using empirical relations that give a curve fit through different data sets (Lindenburg, Ostowari and Naik, Hoerner) and power performance test. It is assumed that the drag coefficient is a function of the airfoil's thickness and aspect ratio. The equations used for the post stall coefficients and the empirical relations can be found in appendix A. It should be noted that in the work of Spera a faulty expression for the CD2 was given, this will be pointed out and corrected in the appendix A as well.

In order to see how well this model of Spera performs, it is applied to four different airfoils (NACA63-215. LS(1)-0417, DU96-W-180 and the DU97-W-300). The required input parameters are obtained from measurement performed by [Bloy and Roberts \(1993\)](#); [Satran and Snyder \(1977\)](#); [Timmer \(2010\)](#). Now to determine the lift and drag curve over a wide range of angle of attack (-10 to 110 degrees) more equations are necessary than those discussed in appendix A. The entire model description can be found in the work of [Spera \(2008\)](#).

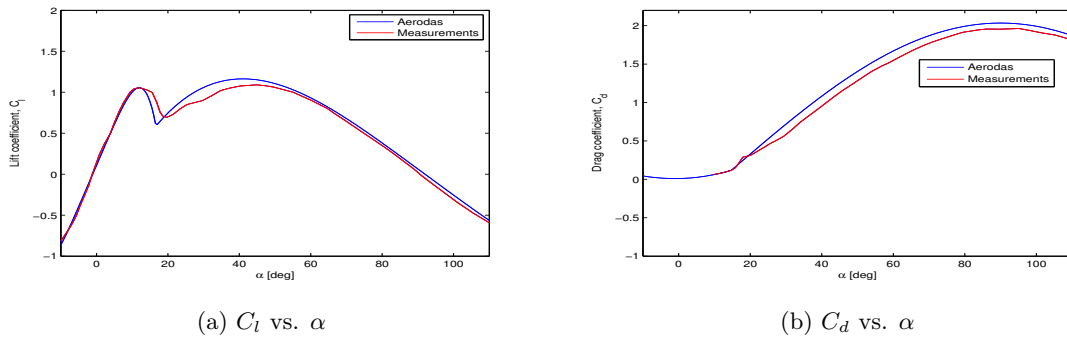
The input parameters needed for the model for each airfoil are summarised in table 2.1 and

determined from measurement data. All measurements were conducted in a closed wind tunnel with models spanning the entire section to create a two dimensional effect and thus resulting in an aspect ratio of infinity.

**Table 2.1:** Aerodas parameters

Parameter	Naca 63-215	LS(1)-0417	DU96-W-180	DU97-W-300
A0	-1.07°	-4.4°	-2.82°	-2.3°
ACL1	12°	16.2°	9.6°	13.3°
CL1max	1.055	1.43	1.246	1.597
S1	0.1011	0.1101	0.1051	0.115
CD0	0.01	0.008	0.0096	0.02
ACD1	14.7°	12°	18°	22°
CD1max	0.1172	0.022	0.16	0.19
t/c	15 %	17%	18%	30%

In figure 2.8 the results are given for the Naca 64-215 airfoil. For the lift coefficient it can be seen that CL2max is overestimated and is reached to soon. The post-stall drag coefficient is in the entire range overestimated.



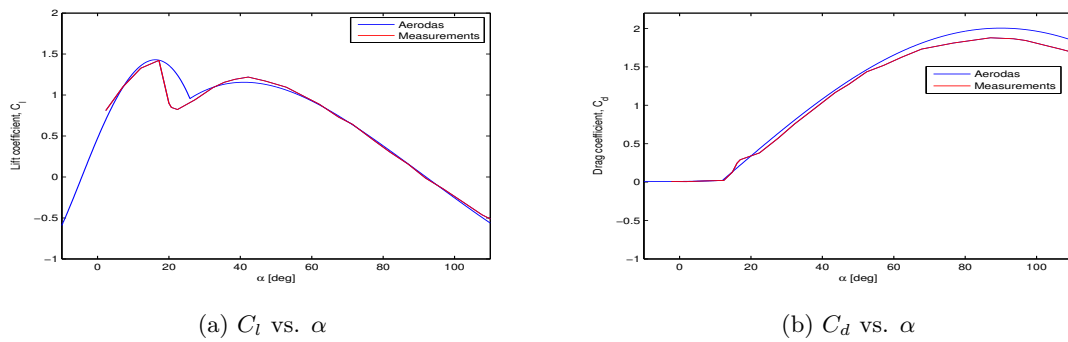
**Figure 2.8:** Lift and drag coefficient vs  $\alpha$ , measurement and Aerodas model (NACA63215)

Figure 2.9 depicts the results for the LS(1) - 0417 airfoil. CL2max is now slightly underestimated but it is reached at a similar angle of attack as during the measurements. For the post-stall drag coefficient an overestimation is found in the entire region.

The results of the DU96-w-180 airfoil are given in figure 2.10. It is found that the CL2max is correctly calculated also for the Post-stall drag good results are found. Only near the maximum drag coefficient a small overestimation is found.

Finally for the DU97-w-300, the thickest profile, the results are depicted in figure 2.11. In this case the post-stall lift and drag coefficients are underestimated.

From the result of these four airfoils it can be concluded that the AERODAS model is not able to accurately predict the post-stall coefficients. The post stall data is determined by the



**Figure 2.9:** Lift and drag coefficient vs  $\alpha$ , measurement and Aerodas model (LS(1)-0417)

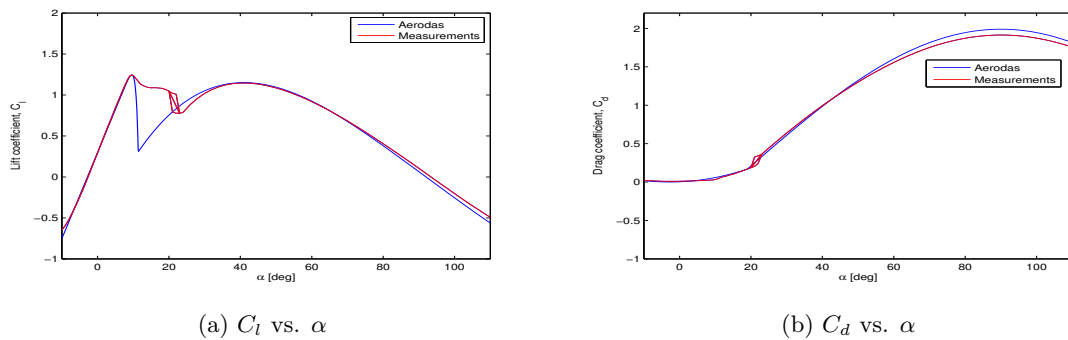


**Figure 2.10:** Lift and drag coefficient vs  $\alpha$ , measurement and Aerodas model (DU96-W-180)

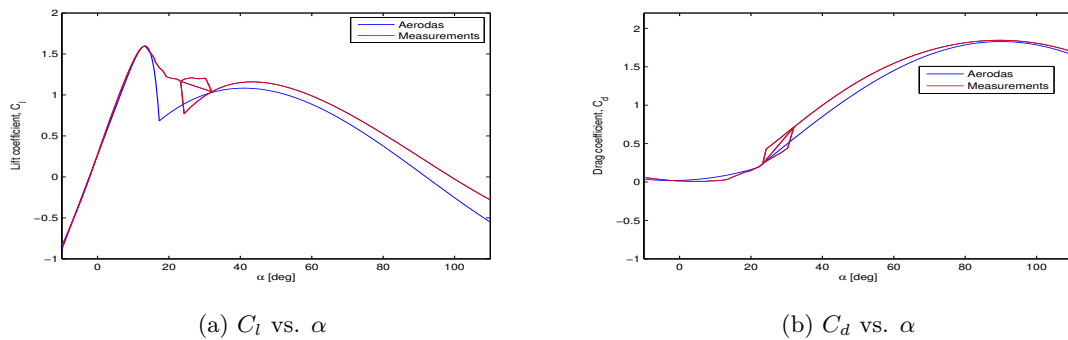


**Figure 2.11:** Lift and drag coefficient vs  $\alpha$ , measurement and Aerodas model (DU97-W-300)

CL2max and CD2max and therefore it are these two parameters that cause the error in the modeling. It is clear that the empirical relations used for determining these two parameters or constructed from insufficient or inaccurate data sets which results in an overestimation of the maximum drag coefficient. This makes it clear that in order to be able to use this prediction model for deep stall coefficients an accurate model is needed to estimate the CL2max and

CD<sub>2max</sub>. In this research the focus will be on finding the maximum drag coefficient in relation to the leading edge thickness, where the leading edge thickness is defined as the  $y/c$  ordinate at  $x/c = 0.0125$ .

## 2.3 Bluff body blockage correction

Windtunnels are intended to replicate an environment in order to get insight in the aerodynamic characteristics a model experiences when passing through free air. In case of a closed test section it is inevitable that the flow around the model is interfering with the windtunnel walls which is the main source of errors. Various correction models are available to correct for this wall interference depending on whether the flow is attached or separated. Airfoils under high angle of attack are characterised by leading edge separation and cause a significant amount of blockage. In this section the bluff body blockage correction method according to Hackett and Cooper is shortly explained together with the important governing equations based on the work of Landstra (2010).

### 2.3.1 Blockage effect

Prior to explaining the correction method the importance and effect of the blockage on the aerodynamic coefficient is explained. The model blockage ratio or model area ratio is defined as the ratio of the model ( $S$ ) and the cross sectional area of the test section ( $C$ ).

$$\text{Model Aspect Ratio} = \frac{S}{C} \quad (2.11)$$

The larger this ratio the more the model obstructs the flow to cross the test section. Conservation of mass inevitably leads to an increase in velocity at the location of the model which results in an increase in dynamic pressure. Due to this increase in dynamic pressure the measured forces with the balance (or determined from pressure orifices) will be higher than expected with the given initial velocity.

In figure 2.12 the increase in drag coefficient is observed with increasing model blockage ratio while in general the drag coefficient of an object (identically shaped) is constant despite an increase or decrease in blockage. This could mean a change in model size or change in the cross section of the test section. in size. Bigger corrections are of course more questionable than small ones and therefore it is beneficial to keep the model area ratio as small as possible.

### 2.3.2 Hackett and Cooper correction

The correction method from Hackett and Cooper Hackett and Cooper (2001) is based on the initial Maskell correction and therefore also referred to as the extended Maskell correction. In the initial Maskell theory a single drag correction is given which can be represented as a single change in dynamic pressure. Hackett and Cooper improved this theory by identifying

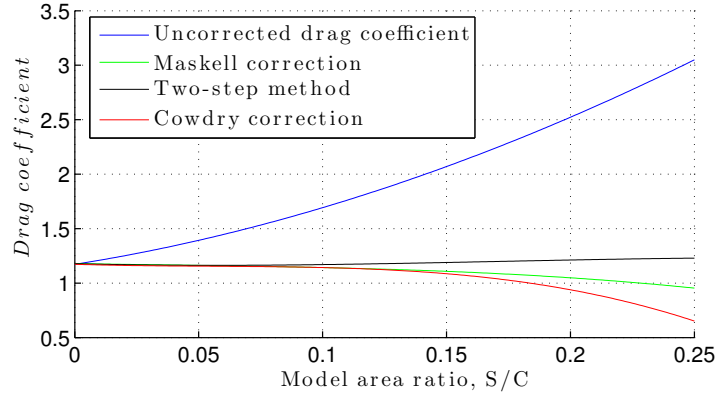


**Figure 2.12:** Comparison of separated flow corrections for 3D normal flat plates, AGARD-336. (1998)

that the increment in dynamic pressure consists of two distinct contributions, this is the drag increment due to the wake distortion ( $\Delta C_{DM}$ ) and the change in dynamic pressure. They state that while the initial Maskell correction tends to over correct the drag coefficient that with the extended correction this tendency is removed.

The method provides two different dynamic pressure corrections, one to correct the drag coefficient and one to correct all other coefficients (lift, moment, pressure). As explained above Hackett and Cooper identified two contribution to the increase in dynamic pressure. For determining the corrected drag coefficient ( $C_{D_c}$ ) it is required to take both contributions into account. This results in the following expression for the dynamic pressure correction.

$$\left(\frac{q_c}{q_u}\right)_{dis} = \frac{C_{D_u}}{C_{D_c}} = 1 + \theta \frac{S}{C} C_{D_u} \quad (2.12)$$

For the other coefficients the drag increment due to wake distortion needs to be subtracted. The dynamic pressure correction than becomes.

$$\left(\frac{q_c}{q_u}\right)_{nodis} = 1 + \theta \frac{S}{C} (C_{D_c M1} - \Delta C_{DM}) \quad (2.13)$$

The term  $C_{D_c M1}$  is the correction including the wake distortion from which the wake distortion ( $\Delta C_{DM}$ ) has to be subtracted. The part of the drag correction without the wake distortion is given in equation 2.14.

$$(C_{D_c M1} - \Delta C_{DM}) = \frac{-1 + \sqrt{1 + 4C_{D_u}\theta(S/C)}}{2\theta S/C} \quad (2.14)$$

The parameter  $\theta$  is called the Maskell blockage correction factor for bluff body flow. Based on experimental data Maskell established a relation between this blockage factor and the aspect ratio of non-lifting rectangular plates. For a infinite aspect ratio or for a flat plate spanning the entire test section (2D) a value of 0.96 for  $\theta$  is suggested by Maskell. This value will therefore also be used for all corrections performed in this research. It is however possible to determine the value of  $\theta$  based on the base pressure and the drag coefficient. The Maskell blockage correction factor is given by the following equation.

$$\theta = \frac{1}{k_c^2 - 1} \quad (2.15)$$

The value of  $k_c$  in equation 2.15 is unknown. An iterative solution can be found using

$$(k_c^2)_n = k^2 \left\{ 1 + \frac{1}{(k_c^2)_{n-1} - 1} \frac{C_{DS}}{C} \right\}^{-1} \quad (2.16)$$

The subscript n indicates the n<sup>th</sup> approximation of  $k_c^2$ . For the first approximation the value of  $(k_c^2)_0$  is equal to  $k^2$  which is related to the base pressure according to the following equation.

$$k^2 = 1 - C_{pb} \quad (2.17)$$

Where  $C_{pb}$  is the average base pressure coefficient.

Now it is possible to determine the Maskell correction factor in function of the angle of attack for a given profile. For the DU91-W2-250, tested at a Reynolds number of 500 000 and spanning the entire height of the wind tunnel, the result is given in figure 2.13.

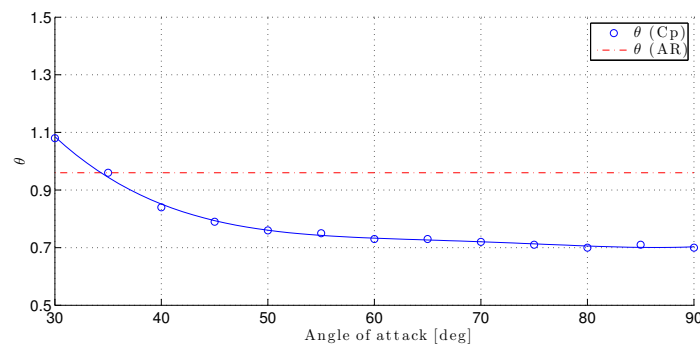


**Figure 2.13:** Comparison between the Maskell correction factor based on the aspect ratio (AR) and on the base pressure (Cp), DU91-W2-250 at  $Re = 5 \times 10^5$

It can be seen that the Maskell correction factor changes with angle of attack when its determined based on the the base pressure while according to the aspect ratio is should be constant. A value of 1.08 is found at an angle of 30° and it drops to 0.7 at 90°. In the beginning a rapid decrease is observed while near the end a more constant value is found. A reason for this variation with angle of attack could be due to the fact that by changing

the angle the frontal area changes. A larger angle of attack increases the frontal area and therefore also the blockage, while the aspect ratio is constant with angle of attack. This is the result of pressure taps which have a fixed spanwise position. It is however possible that at different locations different values for  $\theta$  will be found. This analysis of  $\theta$  is just given to show that the Maskell correction factor in relation to the aspect ratio is questionable to use in all circumstances. However no pressure data will be available for all the models used in this research and therefore it is chosen to use the 0.96 value in all cases to be consequent and to be able to compare different results. The effect of this lower value of  $\theta$  for the higher angles of attack on the pressure distribution can be seen in Appendix B where it is applied to the DU91-W2-250 at 90 degrees angle of attack. It can be seen that a lower value of  $\theta$  results in less correction and therefore the drag coefficient after the correction will reduce less compared to the higher value for  $\theta$ . So in case too low values are found for the drag coefficient after correction, it is possible that this is due to the too high value for  $\theta$ .

---

## Chapter 3

---

# Wind tunnel experiment

Wind tunnel experiments are valuable means of testing in order to acquire information concerning the aerodynamic behaviour of an object. In this chapter the objectives of the conducted experiment are explained followed by the wind tunnels characteristics and the test setup. Furthermore it is shortly explained how the models are designed and which measurement techniques are used.

### 3.1 Objectives

In this thesis it is investigated what effect the leading thickness has on the maximum drag coefficient of an airfoil. Based on tests of various profiles with varying leading edge thickness, starting with a flat plate, this relation will be investigated. The parameter used to define this leading edge thickness is the ordinate  $y/c$  at the  $x/c = 0.0125$  location. From literature it has become clear that increasing the leading edge thickness reduces the maximum drag coefficient but until today the research on this subject is limited and more systematic research is required. Earlier researchers made use of profiles which had different trailing edge angles. The influence of the trailing edge is eliminated by keeping it constant with increasing leading edge thickness.

Due to this high angle of attack configuration the airfoil behaves like a bluff body which results in fully separated flow causing a large amount of pressure drag. The blockage of the flow and the wake are therefore significant factors which need to be taken into account. It is required to correct all the gathered data using a single correction code, only than a relation between LE thickness and maximum drag coefficient can be determined. It is not correct to establish such a LE thickness vs  $C_{d,max}$  relation based on various test performed by various researchers.

By designing various models which have an identical trailing edge and a different LE thickness it is tried to establish this relation. Where from the uncorrected data it is possible to determine a qualitative relation, the corrections are required to make a quantitative statement.

### 3.2 LTT Windtunnel

The first wind tunnel used to perform the experiments in, is the Low Turbulence tunnel (LTT) of the Aerospace faculty of the TU Delft. The LTT is a closed circuit, low speed and low turbulence wind tunnel achieving a maximum velocity of 120  $m/s$ . The large contraction ratio (17.8) ensures that the free-stream turbulence level in the test section varies from only 0.015% at 20  $m/s$  to 0.07% at 75  $m/s$ . There are ten interchangeable test sections which makes it possible to set up the next test while the tunnel is operative. In figure 3.1(a) the control room and the test-section are shown.

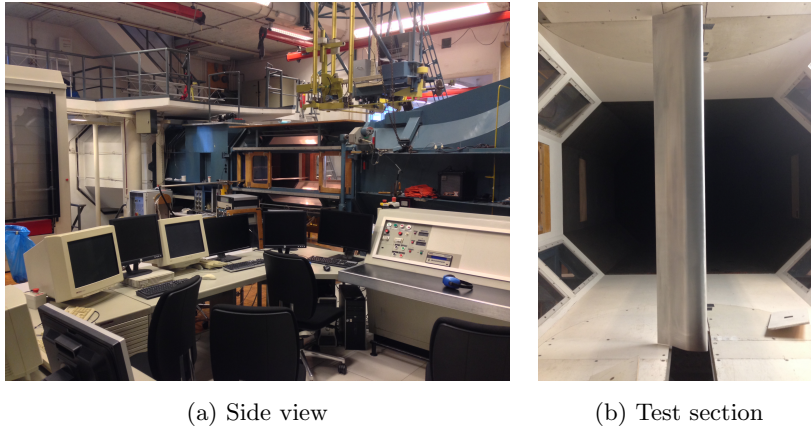


**Figure 3.1:** Low Turbulence, Low speed windtunnel

The test section has a height of 1.25 m, a width of 1.8 m and four corner fillets of 0.42 m making it octagonal. In figure 3.1(b) a view from inside the wind tunnel (downstream) is showing the test section and one of the designed models.

In all cases the model is placed vertically to minimise the amount of blockage. In case of the DU91-W2-250 profile (pressure measurement) the model is attached on both sides to a turning table making it possible to alter the angle off attack without leaving a gap. The other models (balance measurement) are attached only on the upper side to the balance via a shaft, leaving a minimal gap on both sides which could have an influence on the measurements.

Instead of working with an octagonal test-section an equivalent tunnel height ( $h_{eq}$ ) is defined.

$$h_{eq} = h - 2 \frac{b_f - h_f}{b} \quad (3.1)$$

For a vertically installed airfoil the height ( $h$ ) is 1.8 meter and the width( $b$ ) is 1.25 meter. The height and width of the corner fillets,  $h_f$  and  $b_f$  respectively, are both 0.3 meter. The equivalent height then becomes 1.656 meter.

### 3.3 WindGuard

The opportunity arose to conduct the same experiments in a different wind tunnel. WindGuard (also later referred to as WG ) is a German facility for wind tunnel experiments. In their facilities in Bremerhaven a lowspeed wind tunnel is available with the interesting characteristic of having the same height as the LTT but a larger width. The rectangular test section has the following dimensions: 1.25 m x 2.75 m x 5m. This means that the same models can be used resulting in a similar aspect ratio but a smaller blockage ratio. This reduces the amount of correction required which could lead to better results. Furthermore, it can be used as a means of validation of the correction method. In figure 3.2 a side view of the wind tunnel can be seen.



**Figure 3.2:** Side view of the WindGuard wind tunnel

The set-up however is different than in the LTT since they make use of two electronic balances instead of one mechanical. On the lower side they use a six component balance and on the upper side a two component balance. Both balances are connected to a turntable which makes it possible to install the models without any gaps at the model (see figure 3.3(a)). However, a gap is present at both the turning tables in order to be able to connect it to the balances. In figure 3.3(b) a downstream view from inside the inlet is given with the flat plate installed at 90 degrees. Comparing this figure to figure 3.1(b) it can be seen that the blockage is much smaller.

The electronic balance has the advantage over the mechanical one that the measurement frequency is significantly larger. The relative high measuring frequency (100Hz) makes it possible to constantly measure the forces while the profiles are rotating very slowly with a constant angular velocity. Depending on the region that is measured the angular velocity is 0.35 deg/s or 0.12 deg/s. The accuracy on the other hand is less compared to the mechanical balance of the LTT. The electric balances are capable of measuring forces up to 10 000 N which makes them not ideal to measure the small forces or little changes. For each profile a 360° polar is made in two direction in order to observe any influence of the rotation.

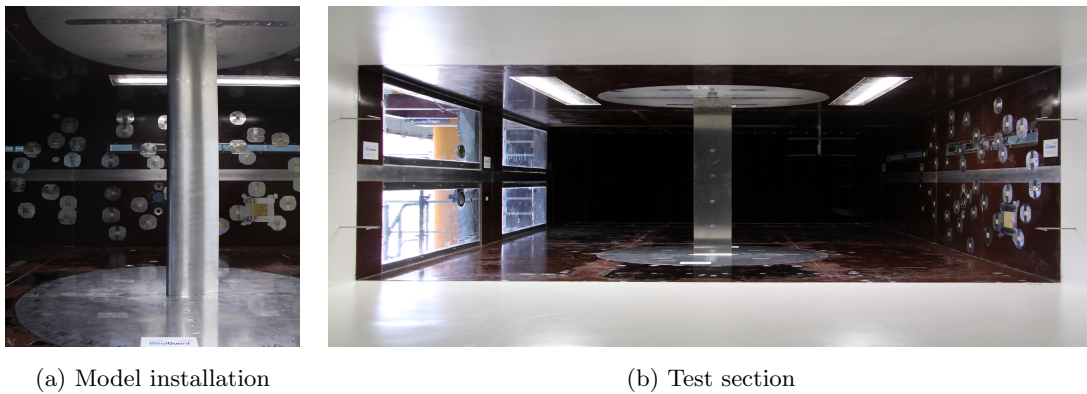


**Figure 3.3:** View from inside the test section of the wind tunnel at WindGuard

## 3.4 Models

During the project different models are used for both the wind tunnel tests as for the CFD simulation: one existing profile, the DU91-w2-250, and several models specifically designed for this project.

### 3.4.1 DU91-W2-250

The DU91-W2-250 airfoil is designed in 1991 for wind turbine applications and is characterised by a 25% thickness. The parameter used in this experiment to identify the leading edge thickness is the  $y/c$  ordinate at  $x/c = 0.0125$ . For the DU91-W2-250 this is found to be 0.031 (lower side). In figure 3.4 the contour of the DU91-W2-250 is depicted. The model will span the entire height of the test section (1.25 m) and will have a chord of 0.15 m.

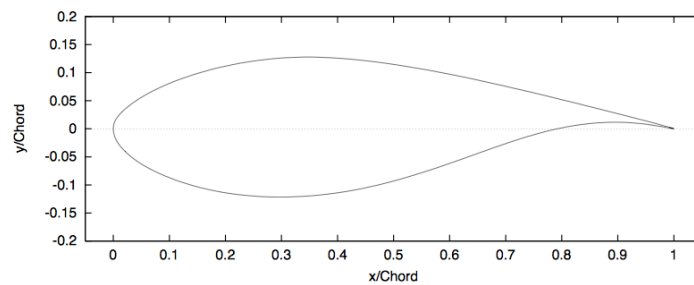


**Figure 3.4:** DU91-W2-250 profile

### 3.4.2 Design of models

In addition to the existing DU91-W2-250 different models are designed specifically for these experiments. In order to verify the effect of the leading edge thickness ( $y/c$  at  $x/c = 0.0125$ ) on the maximum drag coefficient it is chosen to use this as a design parameter according to Timmer (2010). Different profiles are created with varying leading edge thickness and identical trailing edge. The leading edge thickness will vary from zero (flat plate) to  $0.035 y/c$  while for the trailing edge a constant thickness is used similar to the flat plate. By designing the profiles like this the leading edge thickness and the trailing edge are decoupled. In figure 3.5 an example of how these profiles will look is given.

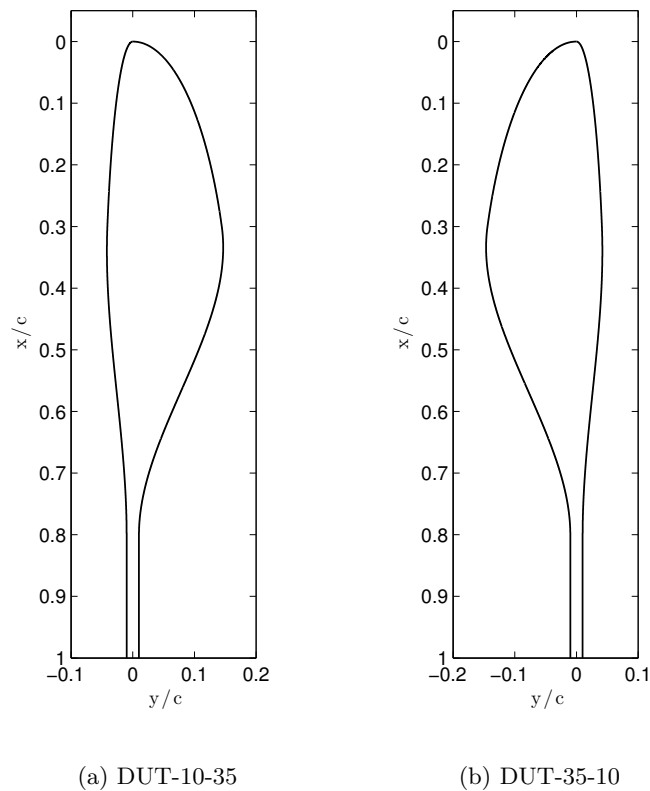


**Figure 3.5:** DUT models

Since it is assumed that the part which is emerged in the wake does not influence the flow it is possible to combine two profiles in one model. The model is here referred to as the physical object while the profile is determined by the leading edge thickness of the frontal surface (surface facing the wind). In figure 3.5 two DUT models are shown, DUT-10-35 and DUT-35-10. Later on in this report the different surfaces will be referred to as upwind surfaces and downwind surface. It should be noted that the DUT-10-35 and the DUT-35-10 are the same model used from the other side.

The design of the profiles is done according to the following steps. For the first 30% of the chord, the shape is determined by an ellipse while the last 20 % is a straight line to create the flat plate. The two parts are connected using a third degree polynomial which is based on the known values of  $y/c$  at  $x/c = 0.3$  and  $x/c = 0.8$  and its derivatives. Below an example of one model (with LE thickness of 0.025) is given. The ellipse used for the first 30% of the model is expressed by equation 3.3.

$$\left(\frac{x - x_0}{A}\right)^2 + \left(\frac{y - y_0}{B}\right)^2 = 1 \quad (3.2)$$

Where  $x_0$  and  $y_0$  are the centre of the ellipse positioned at half chord. A and B are the half length of the long and short axis respectively. The value of A is equal to half the chord since the centre is position at half chord. If now a specific thickness is required like for example a thickness of 0.025  $y/c$  at  $x/c = 0.0125$  the value of B can be determined.

$$B = \frac{y - y_0}{\sqrt{1 - \frac{(x - x_0)^2}{A^2}}} = \frac{0.025}{\sqrt{1 - \frac{0.0125 - 0.5^2}{0.5^2}}} = 0.11250879 \quad (3.3)$$

The equation to determines the profile up to 30% of the chord is now as follows.

$$y = \sqrt{1 - \frac{(x - x_0)^2}{A^2}} * B = \sqrt{1 - \frac{(x - 0.5)^2}{0.5^2}} * 0.11250879 \quad (3.4)$$

The last 20% of the profile is a flat plate with a chosen thickness of 0.01  $y/c$ . The third degree polynomial that is constructed to fluently connect the ellipse shaped front with the flat end is given by equation 3.5

$$y = 1.87916036 * x^3 - 3.197940644 * x^2 + 1.508717139 * x - 0.1124218035 \quad (3.5)$$

In total 4 different models resulting in 7 different profiles are created. The model of the flat plate can only be used from one side since a rather large stiffener is required at the back to prevent excessive bending (see figure ??). This stiffener is assumed to not have an influence on the flow when it is not extending in the deep wake. The chord for all models is chosen to be 0.20 meters, which is a trade-off between blockage and stiffness. A smaller chord would be more beneficial regarding the blockage but consequently this would reduce the thickness and therefore also the stiffness.

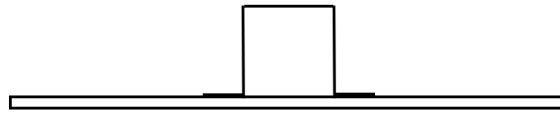


**Figure 3.6:** flat plate

By designing the 'airfoils' as explained above the flat plate works as a good reference object. Earlier research (Hoerner, 1965) shows that for an inclined flat plate ( $\text{AOA} = 90^\circ$ ) the maximum drag coefficient is equal to 1.98. However, other sources give other values in general it is assumed that the maximum drag coefficient will be between 1.96 and 2.01.

Later on in this report the models which are designed and manufactured will be referred to as the DUT models.

## 3.5 Measurement devices and data acquisition

During the wind tunnel tests several different measurement devices are used combined with different software to collect all the data. This section gives an overview of this measurement apparatus and the working principle of the software as it is used in the LTT.

### 3.5.1 Dynamic pressure calibration curve

Since it is not possible to directly measure the free-stream velocity during an experiment it is determined by making use of a so-called dynamic pressure calibration curve. The curve is established in the past for all test-section in case they are empty. This curve gives the relation between the wind tunnel control pressure ( $\Delta P_b$ ) and the dynamic pressure at the centre of the empty testsection. The control pressure is determined from the total pressure in the settling chamber and the static pressure half-way the contraction. The ( $\Delta P_b$ ) results in a free-stream dynamic pressure at the location of the model.

### 3.5.2 Pressure tap measurement

The DU91-W2-250 model is equipped with surface pressure tabs on the upper and lower surface. Both sides have 21 pressure orifices around the centre of the span with an increase in density near the leading edge. The span wise positions of each orifice is slightly different so they do not influence each other. The pressure orifices are connected via the inner side of the airfoil to the DTC Initium measurement device.

### 3.5.3 Balance system

The designed models are not equipped with surface pressure taps and are therefore connected to the external six-component balance system. The balance is a mechanical system that measures six forces to determine the lift force, the drag force, the side force, the pitching moment, the yawing moment and the rolling moment. In figure 3.1(a) the external balance system can be seen above the test section. This mechanical balance is assumed to be accurate but only has a measuring frequency of about 4Hz. Given the high fluctuating measuring conditions a significant amount of measurements are required.

### 3.5.4 Data acquisition and handling

In most cases, when attached flow is investigated, the data that is stored from wind tunnel experiments already contains certain correction with respect to wall interference. For completely separated flow these corrections do not hold and therefore only the raw and uncorrected data is used, afterwards the appropriate correction will be applied.

#### Pressure measurement

For the DU91-W2-250 two different kind of pressure measurement are performed for which different softwares are required. By using an in-house designed code in Labview a time-averaged solution is stored for each orifice and this over a chosen time of 20 seconds. These time-averaged pressure values are useful to determine the drag force and lift force as explained afterwards. A different software called the DTC initium software, makes it possible to store all pressures at a frequency equal to the measuring frequency ( $\approx 650$  Hz). This time depended output reveals unsteady behaviour which can be used to determine the Strouhal number.

In both cases the raw data output are pressure values but for the time averaged data the software converts it in to pressure coefficients using the following expression:

$$C_p = \frac{p - p_0}{q_0}, \quad (3.6)$$

where  $p$  are the readings from the surface pressure tabs,  $p_0$  is the static free-stream pressure (determined from the total free stream pressure measured with a pitot static tube) and  $q_0$  is the dynamic pressure which is determined from the dynamic pressure calibration curve.

For high angles of attack the flow will be fully separated, therefore surface pressure data is sufficient to determine the force coefficient. This is justified because friction drag is negligible compared to the large pressure drag. In case of attached flow or partially attached flow, wake rake data is needed to determine the frictional drag since its contribution can no longer be neglected. Although frictional forces can not be neglected completely in the entire deep stall

region, it is not possible to instal the wake-rake in such a turbulent flow since it will vibrate too excessively.

In order to determine the lift and drag coefficients in case of separated flow the normal force coefficient ( $C_n$ ) and tangential force coefficients ( $C_t$ ) are required. These can be obtained by integrating the pressure coefficient over the contour of the airfoil. Below the expression for the normal and tangential pressure coefficient are given:

$$C_n = \frac{1}{c} \int_0^c (C_{p,l} - C_{p,u}) dx, \quad (3.7)$$

$$C_t = \frac{1}{c} \int_0^c \left( C_{p,u} \frac{dy_u}{dx} - C_{p,l} \frac{dy_l}{dx} \right) dx. \quad (3.8)$$

From the normal and tangential coefficient it is possible to compute the lift coefficient ( $C_l$ ) and the drag coefficient ( $C_d$ ) according to:

$$C_l = C_n \cos \alpha - C_t \sin \alpha, \quad (3.9)$$

$$C_d = C_n \sin \alpha + C_t \cos \alpha. \quad (3.10)$$

In order to determine the lift and drag coefficient for attached flow the wake rake data is used. The wake rake measures the total pressure ( $p_t$ ) and the static pressure ( $p_s$ ) at different locations in the wake. Jones (1936) prescribes the following equation to determine the drag coefficient:

$$C_d = 2 \int \sqrt{C_{p_t} - C_{p_s}} \left( 1 - \sqrt{C_{p_t}} \right) d\frac{y}{c}. \quad (3.11)$$

Note that the measured pressures are transformed into pressure coefficients using equation 3.6. The lift coefficient can be calculated using,

$$C_l = \frac{C_n}{\cos \alpha} - C_d \tan \alpha, \quad (3.12)$$

where the normal force component is determined according to equation 3.7, the drag coefficient according to equation 3.11 and  $\alpha$  is the angle of attack of the airfoil.

### Balance measurement

For the designed models no pressure orifices are present since this would be too expensive and therefore force measurements are performed using the mechanical balance system of the LTT. In figure 3.1(a) the balance system can be observed above the test section. From its initial zero position the balance has the possibility to make large positive angles but only a limited negative angle. So installing the model at  $90^\circ$  angle of attack and to be able to perform the

measurements over the selected angle of attack range ( $40^\circ - 140^\circ$ ) it was necessary to create a positive angle offset for the balance system. The forces are measured in alignments with the axis of the balance system and due to the offset this is not in alignment with the models. A schematic top view of the wind tunnel can be seen in figure 3.7, where the balance system is represented by the grey rectangular box.

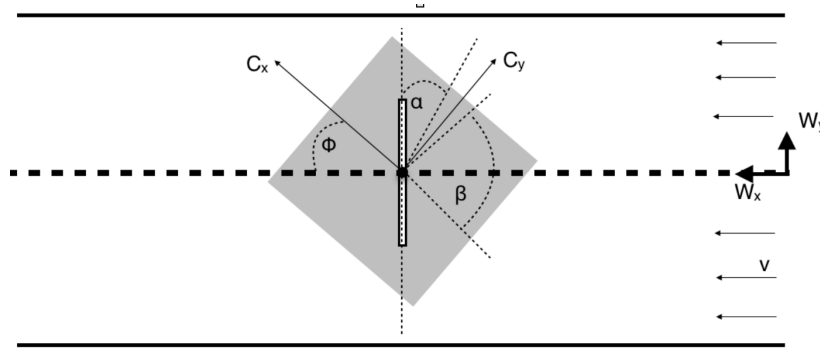


**Figure 3.7:** Schematic overview of the wind tunnel setup

There are three different angles which can be identified from the figure. First of all there is the angle  $\beta$  which is the angle that controls the movement of the balance system. From its start positions (set at zero) this goes from  $-50$  to  $50$  degrees. Secondly there is the angle  $\alpha$  which is the actual angle of attack that the profile experiences, this goes from  $40^\circ$  to  $140^\circ$ . Finally there is the angle  $\phi$  which is the actual angle of the balance system. This angle is equal to the offset angle plus the angle  $\beta$  which is set.

Now to determine the force coefficients the two following equations are used:

$$C_d = C_x * \cos(\phi) - C_y * \sin(\phi), \quad (3.13a)$$

$$C_l = C_x * \sin(\phi) + C_y * \cos(\phi), \quad (3.13b)$$

where  $C_x$  and  $C_y$  are the force coefficients measured along the  $C_x$  and  $C_y$  axis of the balance system respectively. So for each angle that is set ( $\beta$ ) there is a corresponding angle of attack ( $\alpha = 90^\circ + \beta$ ) and a corresponding angle of the balance system ( $\phi = \text{offset} + \beta$ ). The offset angle is slightly different for each profile since a manual adjustment is required after installation of the profile to set it perfectly at  $90$  degrees angle of attack.

---

# Chapter 4

---

## Experimental results

In this chapter the experimental results obtained from measurements in both wind tunnels will be discussed. First all the measurements on the DU91-W2-250 are treated, afterwards the balance measurements from the DUT models are discussed. A comparison between the results obtained from both facilities will conclude this chapter.

### 4.1 DU91-W2-250 model

Different kind of pressure measurements are performed on the DU91-W2-250. First the measurements performed in the LTT are discussed starting with the time averaged pressure measurements. These are used for determining the force coefficients and the pressure distribution around the airfoil under different angles of attack, also the effect of the Reynolds number will be talked over. This is followed by high speed pressure analysis in order to investigate the wake. Finally the measurements performed by WindGuard are discussed.

#### 4.1.1 Time averaged pressure measurement

For the DU91-W2-250 the measurements are performed for angles of attack ranging from -30 degrees to 120 degrees and this at three Reynolds numbers which are:  $2 \times 10^5$ ,  $5 \times 10^5$  and  $7 \times 10^5$ . In a large part of the measurement domain separation will occur which means that the flow will become highly unsteady. Therefore it is required to perform a significant amount of measurements in order to get a meaningful averaged pressure distribution. The angle of attack is each time altered with 5 degrees except near  $C_{l,max}$  where smaller steps are taken, this to capture the start of separation and at each position the pressure is measured for 20 seconds with a frequency of about 650 Hz.

First the force coefficients and the influence of the Reynolds number is discussed, afterwards

more insight is given at certain locations ( $C_{l,max}$ ,  $C_{d,max}$ ) by looking at the pressure distributions.

### Force coefficients

The force coefficients are determined from the pressure data using the equations as described in section 3.5. In figures 4.1 the uncorrected lift, drag and moment coefficient are depicted for the three different Reynolds numbers. It is clear to see that for all three coefficients there are some angle of attack ranges where the Reynolds number has a significant influence on the coefficients and ranges where this can be neglected. To discuss the effect of the Reynolds number it is sufficient to look at the uncorrected coefficients. In order to discuss the values it is required to perform the corrections as discussed in section 2.3, this will be treated later on.

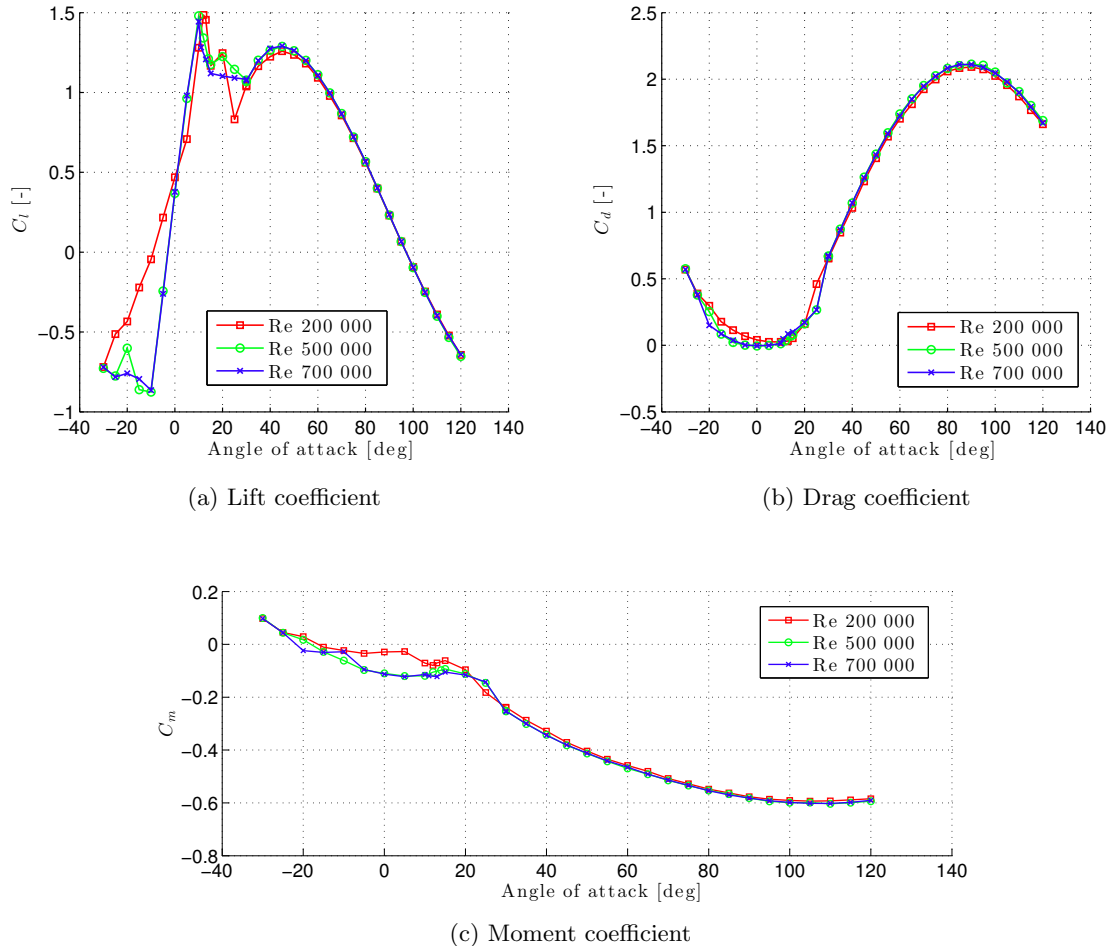


**Figure 4.1:** Uncorrected Lift, drag and moment coefficient of the DU91-W2-250 for Reynolds numbers  $2 \times 10^5$ ,  $5 \times 10^5$  and  $7 \times 10^5$

For the lift coefficient (Figure 4.1(a)) it is observed that, for a Reynolds number of  $5 \times 10^5$

and  $7 \times 10^5$ , the effect is only noticeable around primary stall where the flow is partially stalled. For a Reynolds number of 200 000 a strong influence is observed in the region where fully attached flow is expected. Looking at the pressure distribution later on will show the presence of a laminar separation bubble which could explain this behaviour. In general it is observed that for larger Reynolds numbers the  $C_{lmax}$  decreases and that the lift coefficient is not dependent on the Reynolds number in deep stall ( $\alpha > 50^\circ$ ). The drag coefficient (figure 4.1(b)) is found to be more independent of the the Reynolds number than the lift coefficient. For the Reynolds number  $5 \times 10^5$  and  $7 \times 10^5$  hardly any difference is found over the entire angle of attack range. At a Reynolds number of  $2 \times 10^5$  the drag coefficient is deviating from the others in the range where the flow is assumed to be attached. A similar observation is found for the moment coefficient (figure 4.1(c)). Why the low Reynolds number is behaving differently than the other is explained by looking at the pressure distribution in this region.

### Pressure distribution

Based on the pressure distribution it is possible to identify the start of separation or the presence of a laminar separation bubble for example. This makes it possible to explain why the force coefficients have a certain behaviour and how the Reynolds number has an influence on these. In order to explain why at a Reynolds number of  $2 \times 10^5$  the lift coefficient deviates from the the higher Reynolds number in the region where attached flow is assumed one can look at the pressure distribution in this region. In Figure 4.2 the pressure distribution at an angle of attack of  $-10^\circ$  is given where according to the lift coefficient a significant influence of the Reynolds number plays a roll.

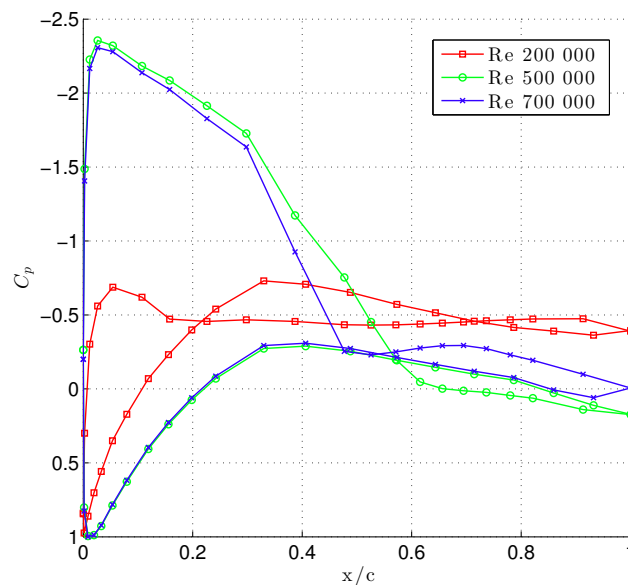


**Figure 4.2:** Uncorrected pressure distribution at  $\alpha = -10^\circ$ , Du91-W2-250

As in figure 4.1(a) it is found that at  $-10^\circ$  the effect of the Reynolds number is clearly visible. For a Reynolds number of 200 000 it can be seen that on the lower side of the airfoil the flow

is almost completely stalled from the leading edge onward while for a Reynolds number of 500 000 the flow is completely attached on the lower side. At the highest Reynolds number a very strong pressure recovery at 30 percent of the chord results in a strong adverse pressure gradient resulting in a separation around mid chord. For the upper surface the two higher Reynolds numbers behave identical up to 90 percent of the chord. For the Reynolds number of 700 00 the flow speed at the trailing edge matches the free-stream velocity while for the Reynolds number of 500 000 a slightly positive pressure coefficient is found at the trailing edge. This means that the flow speed at this point is lower than the free-stream velocity. For the lowest Reynolds number a relative strong suction is present on the upper surface compared to the other Reynolds numbers.

Furthermore, it is shown that around  $C_{lmax}$  ( $\alpha \approx 11^\circ$ ) the influence of the Reynolds number is important, therefore in figure 4.3 the pressure distribution around  $C_{lmax}$  is given. In figure 4.3(a) it can be seen that on the upper side for  $Re \times 10^5$  a laminar separation bubble is present just before mid chord of the airfoil, afterwards the flow reattaches and remains attached until the end. For the higher Reynolds numbers this separation is not present, however it appears that transition from laminar to turbulent flow occurs around 35 percent of the chord. On the lower side it is observed that the two higher Reynolds numbers cause earlier reattachment compared to the Reynolds number of 200 000. Looking at figure 4.3(b), which is the pressure distribution at  $11^\circ$  angle of attack, it can be seen that for the two highest Reynolds numbers flow separation occurs. The adverse pressure gradient becomes too big and separation occurs around 55 percent of the chord. For the lower Reynolds number it can be seen that the flow is still attached, therefore the maximum lift coefficient for the lowest Reynolds number is found later ( $\alpha \approx 12^\circ$ ) than for the other two Reynolds numbers ( $\alpha \approx 11^\circ$ ). It is noted that the separation bubble tends to reduce or disappear at this higher angle of attack so that normal laminar turbulent transition occurs.

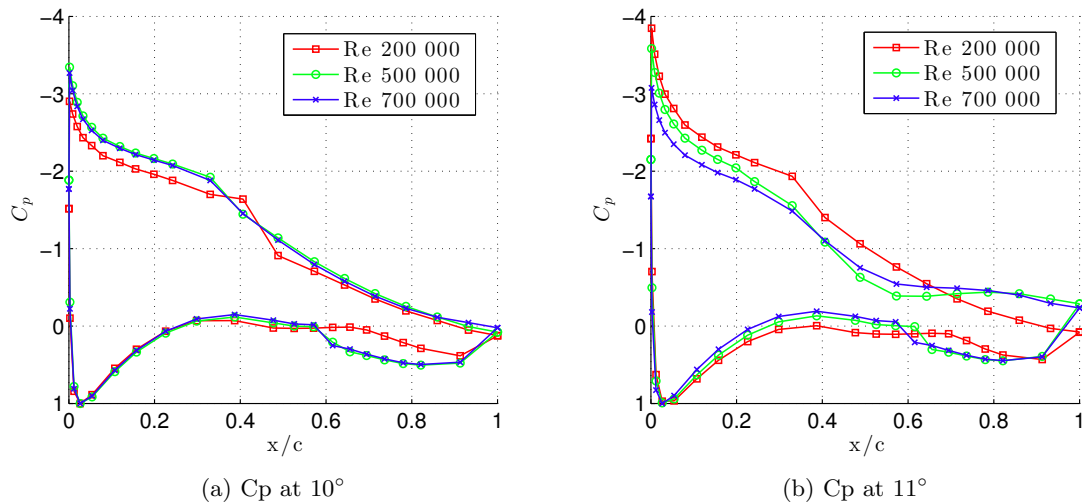


**Figure 4.3:** Uncorrected pressure distribution for Reynolds numbers  $2 \times 10^5$ ,  $5 \times 10^5$  and  $7 \times 10^5$

From figures 4.1 it is concluded that a Reynolds number between  $2 \times 10^5$  and  $7 \times 10^5$  has no significant influence on the force coefficients for completely separated flow ( $\alpha > 50^\circ$ ). In

figure 4.4 the pressure coefficient at  $90^\circ$  angle of attack is given.

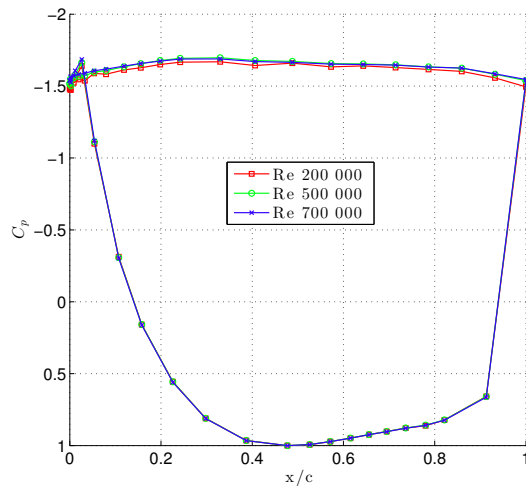


**Figure 4.4:** Uncorrected pressure coefficient DU91-W2-250 at  $90^\circ$

It can be seen that the pressure coefficient at the lower side is identical for all three Reynolds numbers. The upper side, which is completely separated, only shows very small differences around the leading edge which means that for the force coefficients hardly any effect of the Reynolds number is noticeable.

Finally the corrected lift and drag coefficients are presented below. In the region where the flow is fully separated the blockage method of Hackett and Cooper is used as explained in Chapter 2. In the other region a classical wind tunnel corrections is used.

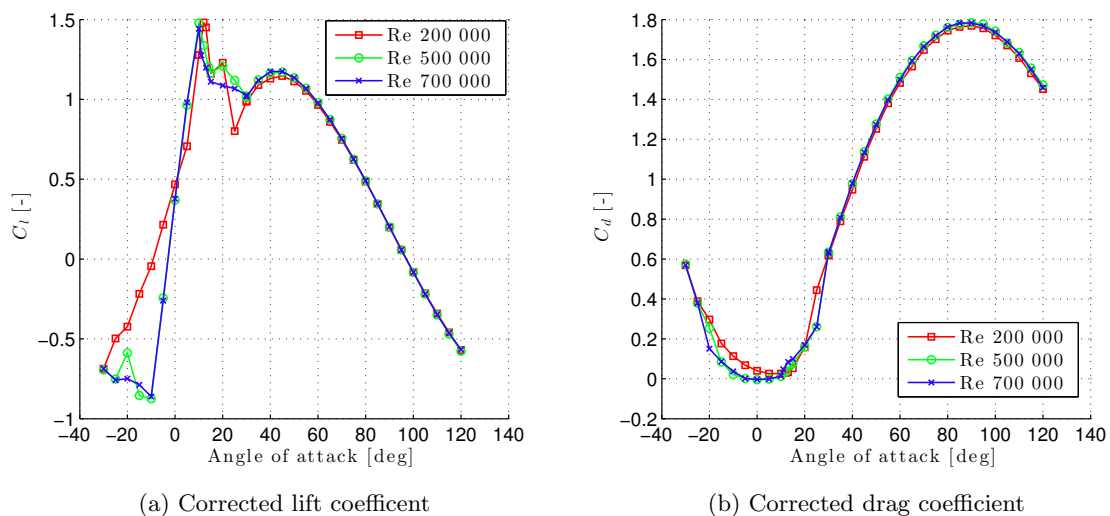


**Figure 4.5:** Corrected lift and drag coefficient DU91-W2-250, at  $Re = 2 \times 10^5$ ,  $5 \times 10^5$  and  $7 \times 10^5$

### 4.1.2 High speed data

While time averaged pressure data are useful to determine the force coefficients and identify flow separation from pressure coefficient distributions it is not possible to determine the fluctuations in the wake which also provide interesting information. Using high speed measurement software the data is stored with a frequency of about 650 Hz which makes it possible to analyse the fluctuations. This analysis is performed at two Reynolds number ( $Re = 2 \times 10^5$  and  $5 \times 10^5$ ). The pressure fluctuations on the trailing and leading edge of the airfoil give information about the vortex shedding frequency. In figure 4.6(a) an example of such a high speed signal output is given. In order to determine the frequency of the fluctuations from the output signal a fourier transform is performed. The corresponding fourier transform of the given signal can be seen in figure 4.6(b).

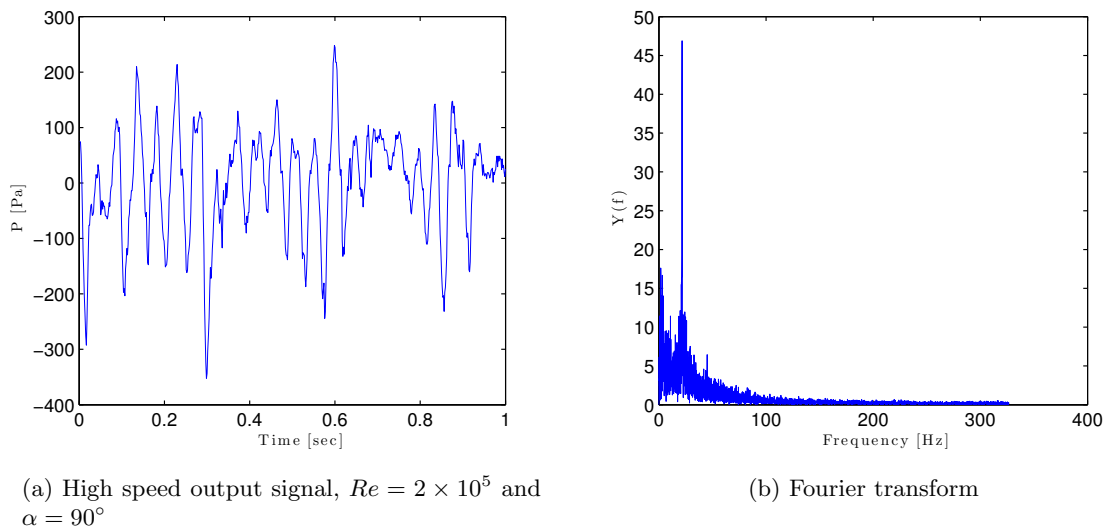


**Figure 4.6:** High speed data and fourier transform

From the fourier transform it is possible to determine the shedding frequency of the flow which is found by locating the highest peak in the fourier transform. From figure 4.6(b) the frequency is found to be 21.7 Hz. According to equation 2.1 the Strouhal number then becomes 0.16. Performing this analysis for all angles of attack in deep stall (30 - 90) at both Reynolds numbers yields the results as presented in figure 4.7

It can be seen that in this deep stall region the Strouhal number is independent of the Reynolds number and that for increasing angle of attack the Strouhal number reduces. Near  $90^\circ$  angle of attack the influence of the angle of attack also diminishes. Comparing this with the Strouhal number for an inclined flat plate (see section 2.1 figure 2.2) the similar results are obtained. This means that the flow in the wake of a flat plate and the DU91-W2-250 behave similar.

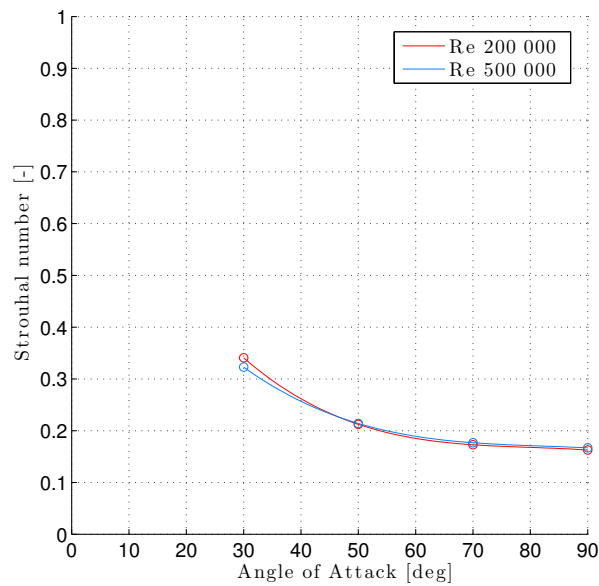


**Figure 4.7:** Strouhal number for DU91-W2-250 at  $Re = 2 \times 10^5$  and  $5 \times 10^5$

### 4.1.3 WindGuard

Due to the different setup at WindGuard it was possible to perform pressure and balance measurement at the same time which enables us to do a comparison between both measurement techniques. In figure 4.8 the lift and drag coefficient obtained from both measuring techniques are depicted.

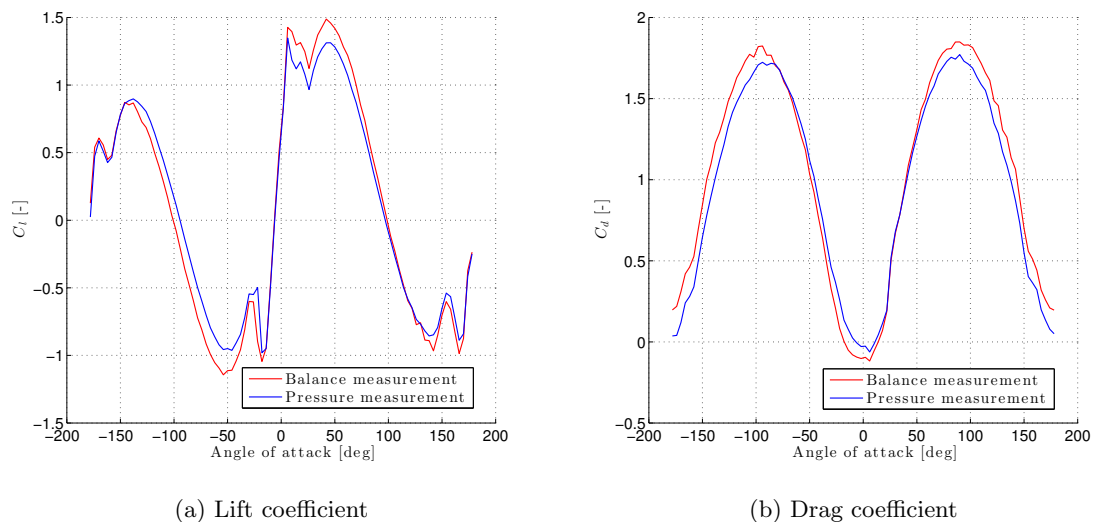


**Figure 4.8:** Force coefficient DU91-W2-250 based on balance and pressure measurements,  $Re = 5 \times 10^5$

The lift coefficient (figure 4.8(a)) shows good comparison between both measurement techniques in the region where the flow is attached while in the region where the flow is partially or completely stalled a significant difference is noticeable. In the (post-) stall region the balance measurement results in higher values for the lift coefficient.

The drag coefficient on the other hand(see figure 4.8(b))shows better agreement between both methods in the beginning of the stalled region than in the attached region. In the attached region on the other hand the balance measurement even yield a negative drag coefficient which is not possible.

In order to see how the pressure measurement performed by WindGuard compares to the pressure measurement in the LTT the pressure distributions of the DU91-W2-250 at  $90^\circ$  angle of attack are plotted in figure 4.9

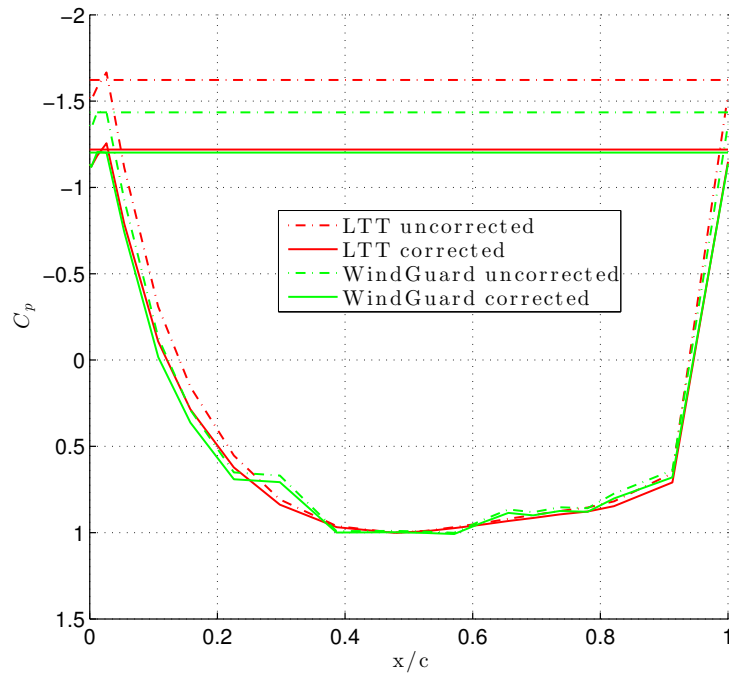


**Figure 4.9:** Pressure distribution at  $90^\circ$  angle of attack according to the LTT ( $Re = 5 \times 10^5$ ) and WG ( $Re = 6 \times 10^5$ ), DU91-W2-250

Both the corrected and uncorrected pressure distribution is given in the figure. It can be seen that at the LTT the base pressure is significant lower than compared to the measurement by WG. This is explained by the larger blockage ratio which is present in the LTT. For a tunnel width of 1.8 m (LTT) the blockage ratio of the DU 91-W2-250 models becomes about 0.08 while at WindGuard the blockage ratio reduced to about 0.05 given the tunnel width of 2.75 m. After applying the correction as explained in chapter 2 it can be seen that the base pressures compare rather well (LTT slightly lower). On the lower side of the airfoil the pressure coefficient does not change much after the correction and are almost identical. Here it also shown clearly that a smaller blockage results in smaller correction which is obvious.

From this analysis it can be concluded that the pressure measurement in the LTT and WindGuard gives similar results while for the balance measurement by WindGuard a certain offset is detected with respect to the pressure measurement. Also again it can be seen that there is no difference between the pressure distribution although the Reynolds numbers at the LTT is much lower. Furthermore it is shown that the correction method of Hackett and Cooper leads to comparable results after correction although the blockage factor is different in both cases. Although it is found that according to the base pressure a different value of the maskell blockage factor should be used (LTT  $\theta = 0.7$  and WG  $\theta = 0.81$ ). More investigation in this subjected is required but this is outside the scope of this project also because the DUT models or not equipped with pressure orifices.

## 4.2 DUT models

In this section the results of the balance measurements performed in the LTT wind tunnel are presented and discussed. As explained in section 3.4 in total seven different profiles are tested. The measurement range is set from an angle of attack of 40 degrees up to 140 degrees. All the DUT models are tested at a Reynolds number of 150 000 which is lower than intended. Because the models are only supported on one side it is not possible to test at higher Reynolds numbers since this would cause the model to vibrate excessively which could introduce errors or damage the wind tunnel. In this section only the averaged corrected data are treated, first the lift and drag coefficient of the flat plate are discussed since this is used to validate the measurements, afterwards the results of the other models will be treated. This section will conclude with a relation between the lift and drag coefficient at 90° angle of attack and the leading edge thickness.

### 4.2.1 Aerodynamic characteristics

Prior to looking at the results of all the DUT models it is recommended to verify the results of the measurement. In order to do so it is possible to compare the flat plate data with the ideal flat plate theory as described by equation 2.2. This gives an initial idea of how well the measurements behave in certain regions. In figure 4.10 the lift and drag coefficient from both, the measurement and the theory, are plotted.

As can be seen in the figure the theoretical and experimental data do not always compare in a good way. For the lift coefficient it is noted that around 90° the experimental and theoretical results match perfectly and that towards the end of the measurement domain the deviation grows. The theory for the drag coefficient results in a higher maximum value and reduces somewhat faster than according to the experimental data. The measurements however are not completely 2D since at the lower and upper side of the flat plate a small gap is present, this could be one of the reasons why the measurements do not agree with the theory. Later on in this report the effect of the gap will be discussed based on measurements performed by WindGuard. Furthermore, the model vibrates and deflects a little even at this small Reynolds number and it cannot not be excluded that the blockage corrections have an influence on the

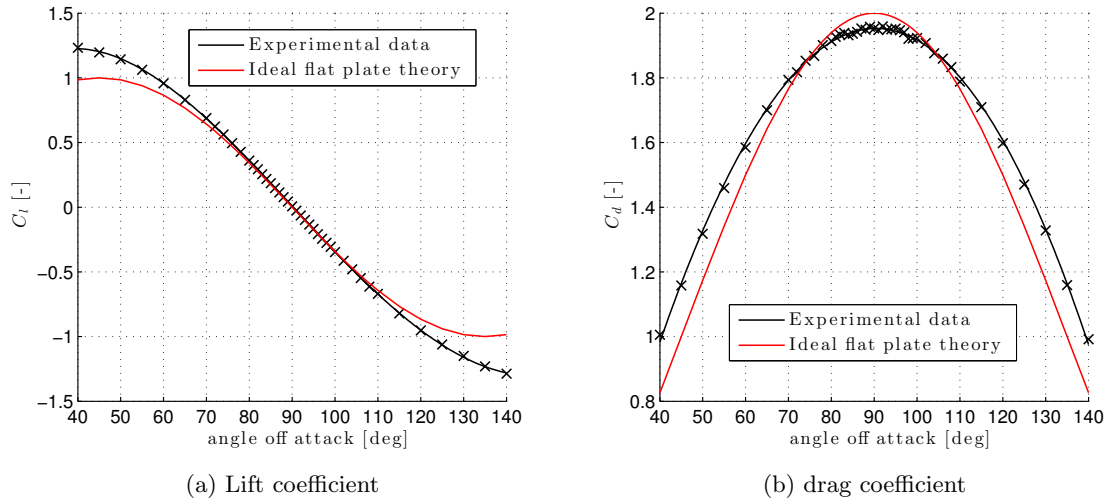


**Figure 4.10:** Experimental and theoretical flat plate drag and lift coefficient,  $Re = 1.5 \times 10^5$

actual coefficients. The increase in difference between both near the end of the domain could be explained to the fact that for the ideal flat plate theory no viscous drag is considered. The effect of this in the ideal theory becomes more pronounced in these regions.

In figures 4.11(a) and 4.11(b) the lift coefficient versus the angle of attack is given for all the models. Although the graph does not clearly indicate the lift coefficient in the entire regions a distinct pattern is present. It is observed that for an increasing leading edge thickness the zero lift coefficient moves to a larger angle of attack. From 90 degrees for a flat plate up to 96 degrees for the thickest profile. Furthermore, it can be seen that in case the rounded leading edge is tilted forward ( $40^\circ \leq \alpha \leq 90^\circ$ ) the influence of the leading edge thickness is smaller than in case the leading edge is tilted to the back ( $90^\circ \leq \alpha \leq 140^\circ$ ).

In figures 4.11(c) and 4.11(d) the corrected drag coefficient for all models is plotted. It can be seen that for the smallest leading edge thickness the maximum drag coefficient is located at 90 degrees while the thicker profiles tend to have the maximum drag coefficient at a slightly lower angle of attack ( $89^\circ$ ). This same shift in maximum drag coefficient is observed by [Viterna et al. \(1981\)](#). Furthermore it looks that the drag coefficient is symmetric around the point of maximum drag coefficient ( $89^\circ$ -  $90^\circ$ ). No difference is observed whether the leading edge is tilted forward or backward as was the case for the lift coefficient.

Finally the moment coefficient is measured at 33.5 percent of the chord since this is the location of the shaft which connects the model to the balance system( for the flat plate the location of the shaft is at mid chord). It is possible to recalculate this moment coefficient to any desired point (25 percent chord is normally used in aerodynamics). However, it is chosen to keep the results as they are originally obtained. The results are given in figure 4.12.

The moment coefficient around 50 percent chord of a flat plate has some inherent characteristics which can easily be seen at a graph. These are the zero moment coefficient at  $90^\circ$  and the

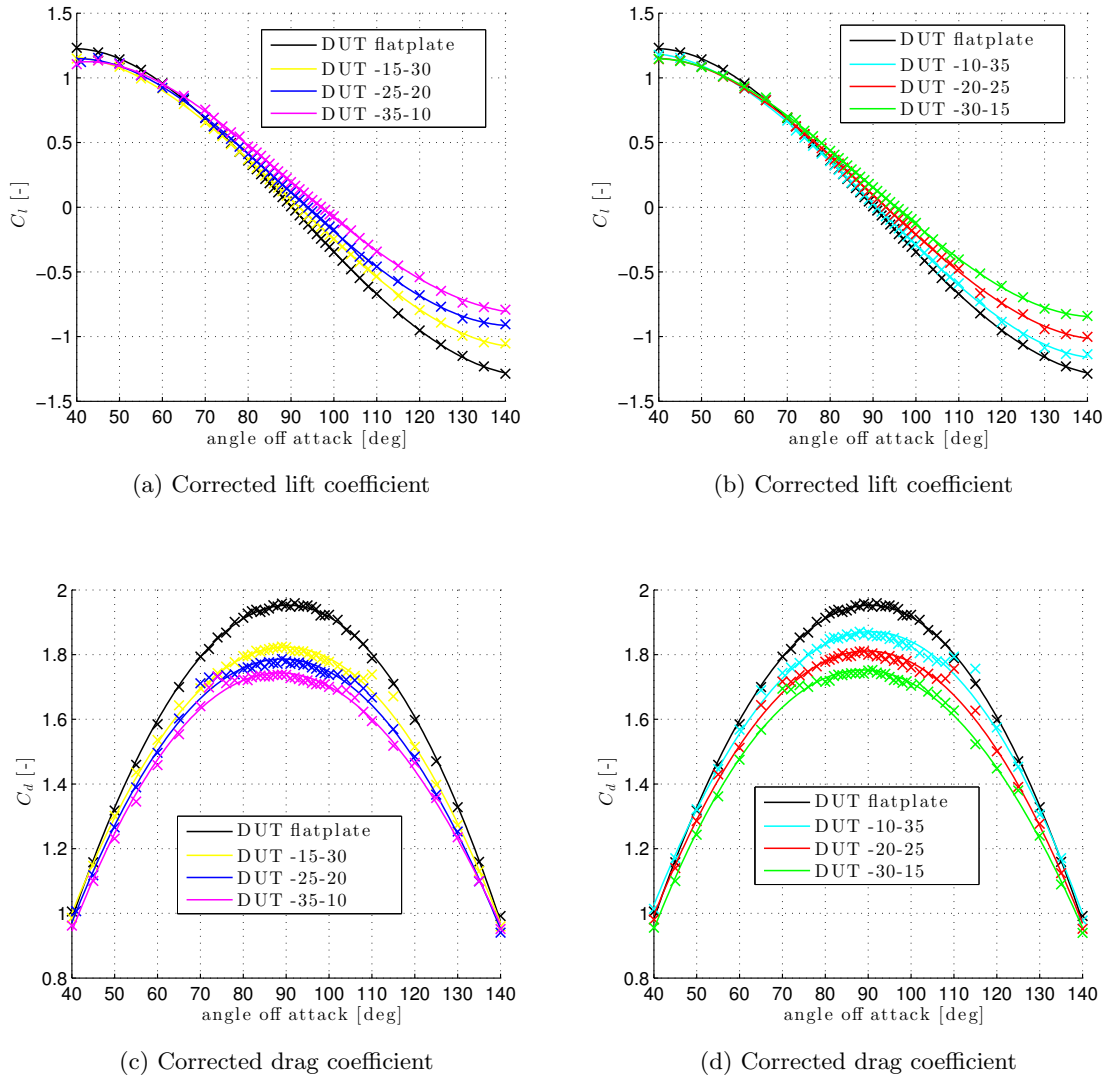


**Figure 4.11:** Corrected lift and drag coefficient in deep stall region for the DUT models,  $Re = 1.5 \times 10^5$

antisymmetric behaviour around  $90^\circ$ . Therefore it is chosen to keep the moment coefficient of the flat plate around 50 percent chord. However, it is noted that an offset is present for this zero moment coefficient ( $\approx +8^\circ$ ) which is most likely a measurement error rather than a physical fact also the antisymmetry is not full filled. The moment coefficient of the other models, around 33.5 percent of the chord, or here present to give an indication of their value and how they behave with changing angle of attack. While for the drag and lift coefficient a clear relation was observed with respect to the leading edge thickness this is not the case for the moment coefficient.

As mentioned before the attachment point for all the models, except the flat plate, are not at the centre of the model. This has as a consequence that the model is not positioned in

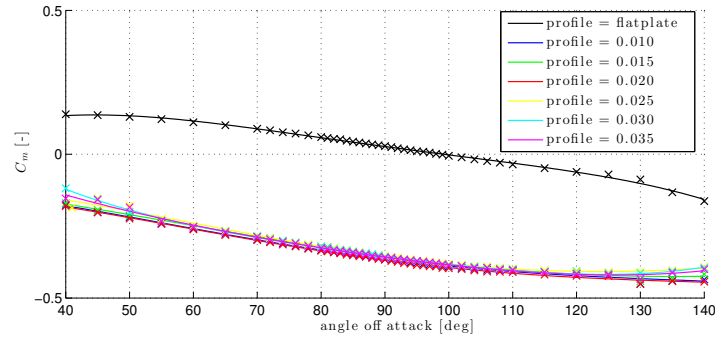


**Figure 4.12:** Corrected moment coefficients of all the models,  $Re = 1.5 \times 10^5$

the middle of the test section and causes the flow to prefer one side above the other since less blockage is present. Whether this has an effect on the measurements or on the correction technique is not certain and not taken into account. Further investigation is required to make a statement on this.

#### 4.2.2 Leading edge thickness vs $C_{d,max}$

Now that the coefficients are known it is possible to find a relation between the design parameter  $y/c$  at  $x/c = 0.0125$  and the lift and drag coefficient at  $90^\circ$  angle of attack. As indicated above for the moment coefficient no relation was found with respect to the leading edge thickness and therefore no extra attention will be given to it. In table 4.1 an overview is given for various airfoils (having different trailing edges) which are discussed by [Timmer \(2010\)](#) in earlier research. Table 4.2 then gives the results from the current research on the DUT models.

**Table 4.1:** Overview of  $C_{d,max}$  and  $C_l@90^\circ$  for different airfoils [Timmer \(2010\)](#)

	$y/c$	$C_{d,max}$	$C_l@90^\circ$
Flat plate	0	1.98	0
Naca 63-215	0.01793	1.960	0.09
LS(1) - 0417, 90gr	0.02129	1.877	0.06
LS(1) - 0417, 270gr	0.03011	1.800	0.115
DU96-W-180, 90gr	0.01887	1.914	0.106
DU96-W-180, 270gr	0.02072	1.832	0.113
Naca 0012	0.01894	1.914	0.08
Naca 0018	0.02841	1.800	0.115
DU91-W2-250	0.031	1.859	0.171
DU97-W-300, 90gr	0.03327	1.806	0.247
DU97-W-300, 270gr	0.03069	1.845	0.163

In figure 4.10(a) the lift coefficient at  $90^\circ$  angle of attack is given in relation to the leading edge thickness. Its clear to see that a quadratic least square fit gives a better result for

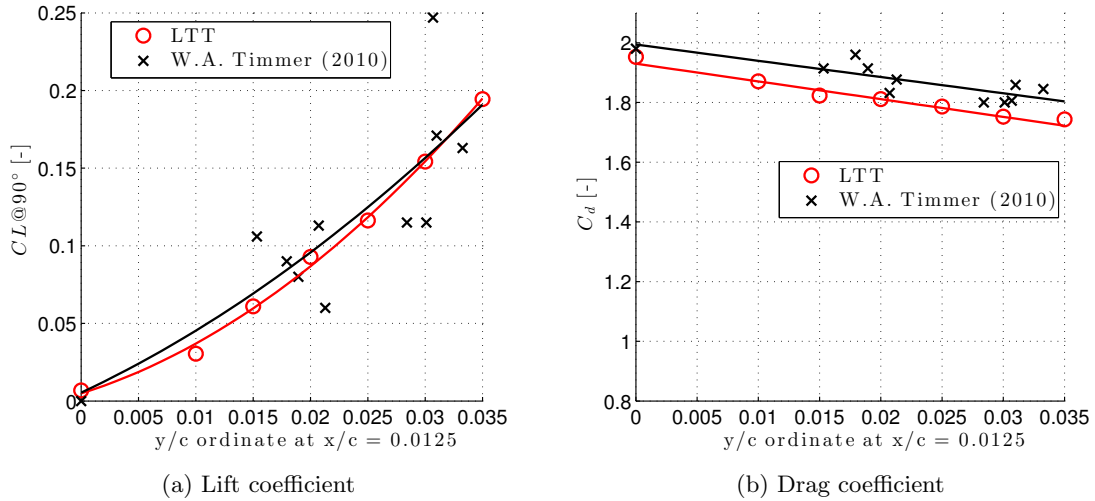
**Table 4.2:** Overview of  $C_{d,max}$  and  $C_l@90^\circ$  for the DUT models

	$y/c$	$C_{d,max}$	$C_l@90^\circ$
Flat plate	0	1.98	0
DUT-10-35	0.010	1.960	0.09
DUT-15-30	0.015	1.877	0.06
DUT-20-25	0.020	1.800	0.115
DUT-25-20	0.025	1.914	0.106
DUT-30-15	0.030	1.832	0.113
DUT-35-10	0.035	1.914	0.08

the DUT airfoils then for the various airfoils given by Timmer. This is possibly due to the systematic approach of increasing the leading edge thickness while keeping the trailing edge constant. This is not the case for the results shown by Timmer. The corresponding equations are:

$$Cl@90^\circ = 88.764(y/c)^2 + 2.3217(y/c) + 0.0049, \quad (4.1)$$

$$Cl@90^\circ = 52.33(y/c)^3 + 0.74(y/c) + 0.0054 \quad (W.A.Timmer). \quad (4.2)$$

**Figure 4.13:** Lift and drag coefficient at  $90^\circ$  angle of attack in relation to the leading edge thickness,  $Re = 1.5 \times 10^5$ 

The drag coefficient in figure 4.10(b) shows a linear decreasing with increasing leading edge thickness for both the DUT airfoils and the airfoils discussed by Timmer. Also here it is observed that the the linear fit better approaches the actual results in case of the DUT airfoils. The relations for the drag coefficient at  $90^\circ$  angle of attack as they can be seen in the figure are given by the following expressions:

$$C_{d,max} = 1.93 - 5.94(y/c), \quad (4.3a)$$

$$C_{d_{max}} = 1.994 - 5.4375(y/c) \quad (W.A.Timmer). \quad (4.3b)$$

From the equations it can be seen that this current research results in a slightly stronger decrease with increasing leading edge thickness compared to the results of Timmer. Furthermore, it can also be seen that in this research the drag coefficient of the flat plate (and the other models compared to the results of Timmer) is rather low.

The reason for a reduction in drag and an increase in lift can not be found based on the balance measurements only. A possible reason why the drag reduces, also indicated by Lindenburg and Montgomerie, is due to the increasing rounding at the nose which better prepares the flow to go around the object and therefore reduces the wake. This would explain the reduction in the drag coefficient, but from these balance measurements this explanation can not be judged. Furthermore, from the high speed pressure data of the DU91-W2-250 it is found that the frequency and thus the Strouhal number is not changing with respect to the flat plate although the drag is reduced. This would mean that the wake is not changed and consequently the explanation of the smaller wake might not be true. Flow visualisations or pressure measurement are required to evaluate what is happening around the leading edge and possibly explain the drag reduction and increase in lift. Experimentally these test are not conducted since, no pressure orifices are present in the current models and no time was available to conduct flow visualisations in the LTT. Later on in this report an explanation will be given to this drag reduction based on pressure data and flow visualisation obtained from CFD computations.

### 4.3 Comparison WindGuard data

In this section the experimental data obtained by WindGuard are discussed and compared to the data found in the LTT. As explained in section 3.3 WindGuard supports the model on both sides which makes it more rigid and therefore makes it possible to run at higher Reynolds numbers compared to the experiment in the LTT. In the region of interest ( $40^\circ \leq \alpha \leq 140^\circ$ ) these higher Reynolds numbers will not have much effect on the force coefficients since it was shown that the lift and drag coefficient are independent of the Reynolds number in the deep stall region. However it is observed that for a low Reynolds number (150 000) the measurements from WindGuard are inconsistent and inaccurate while this is not the case for the measurements in the LTT. The reason for these results at low speed is probably caused by the accuracy of the WindGuard balance system. The balance is capable of measuring forces up to 10 000 N where at the lowest Reynolds number only forces of 20 N appear, which makes the measurements very prone to errors. A similar problem is observed earlier on for the DU91-W2-250 measurements of WindGuard. There it was found that in the region where the forces are low, for the lift coefficient in the stalled region and for the drag coefficient in the attached region, that the balance measurement deviates the most from the pressure measurements. Therefore the data presented here of WindGuard are all obtained from measurements with

a Reynolds number of  $6 \times 10^5$  such that the forces are large enough and thus the balance performs well.

In figure 4.14 the corrected lift and drag coefficients for the flat plate are depicted as it is obtained from the LTT and from WindGuard. Furthermore, the theoretical ideal flat plate values are shown. For the lift coefficient (figure 4.14(a)) it can be seen that the WindGuard data is shifted upwards or to the right with respect to the LTT data over the entire measurement domain. and this is based on the lift coefficient at  $90^\circ$  angle of attack. In any case the lift coefficient should be zero which is according to the theory and the measurements in the LTT. When this lift production at  $90^\circ$  would be deducted from the entire range almost a perfect match with the LTT is found. This means almost perfect according to the ideal flat plate theory around  $90^\circ$  and increasing deviation towards the end of the measurement domain. Because of this it can be excluded that the deviation towards the end of the domain between the theory and the measurements is due to blockage correction. For both wind tunnel measurements a similar deviation is found at the end of the domain while the amount of blockage correction is significantly different.

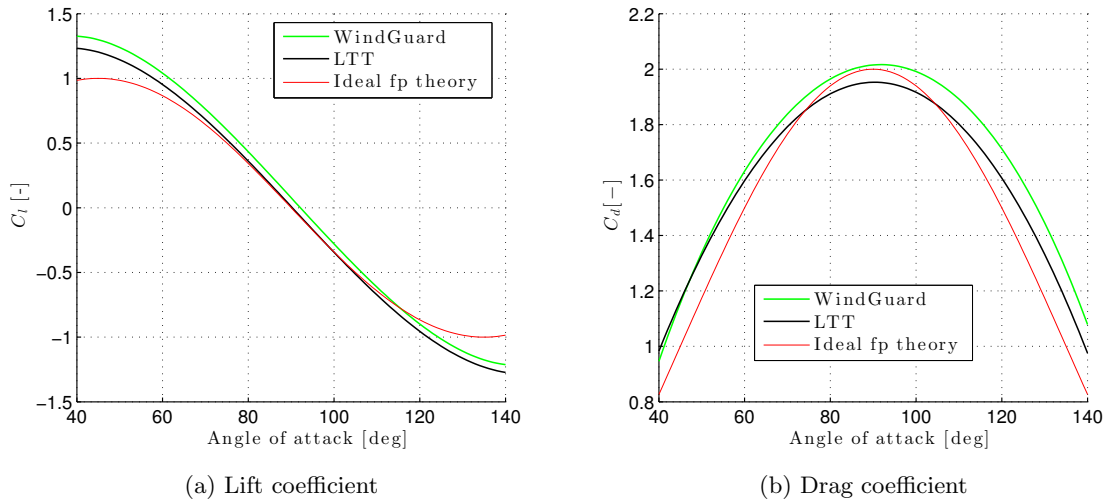


**Figure 4.14:** Flat plate data from WindGuard ( $Re = 6 \times 10^5$ ), LTT ( $Re = 1.5 \times 10^5$ ) and Ideal flat plate theory

The drag coefficient (see figure 4.14(b)) according to WindGuard start in agreement with those of the LTT but diverges quickly. Similar to the lift coefficient also here is an increase observed, this increase in drag grows up to about  $90^\circ$  angle of attack and from here on the elevation is almost constant. Looking at the maximum drag coefficient it seems that this is reached just after  $90^\circ$  angle of attack which is not in agreement with the theory, the measurement in the LTT and earlier research by for example [Viterna et al. \(1981\)](#). The maximum drag coefficient of 2.01 on the other hand is closer to the ideal flat plate theory than the 1.95 according to the LTT. Furthermore it is observed that the drag coefficient curve is not symmetrical around  $90^\circ$ . For a flat plate it is logic that at 40 degrees and 140 degrees the drag coefficient is identical, while this is the case for the theory and the LTT a significant discrepancy is found between both by WindGuard. This antisymmetry can

possibly be addressed to the shift which is observed in the lift coefficient.

There can be a variety of reasons for these misalignments between the WindGuard measurements and the LTT measurements. The difference in maximum drag coefficient could be due to the difference in blockage ratio, for the LTT measurement significant more amount of correction is required which increases the uncertainty of the values and it even could lead to overcorrection of the drag coefficient resulting in a lower drag. In the second chapter it is already indicated that the maskell correction factor of 0.96 is questionable and this could also explain the lower drag coefficient. Besides the different blockage ratio also the way the model is supported during the measurements could cause deviation in the results. In the LTT the model is only supported at one side which allows a certain amount of movement of the model plus a gap is present at both ends. These gaps (about 2 mm at each side) and movement of the model could introduce side effects which lead to different flow behaviour. The effect of the gap however is investigated by WindGuard. The difference between a measurement with a gap at one end and a measurement without any gaps can be seen in figure 4.15. Each configuration is tested three times which enables us to present the data with error bars, the solid line represents the average value. This experiment is conducted over a smaller angle of attack range and to improve the accuracy the angular velocity is decreased.

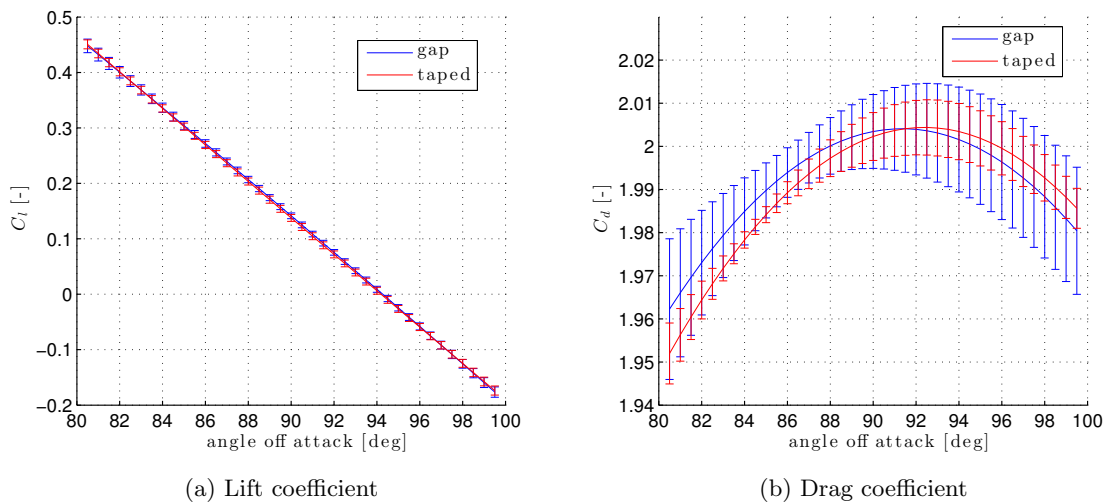


**Figure 4.15:** The effect of one gap on the lift and drag coefficient of the flat plate,  $Re = 6 \times 10^5$

For the lift coefficient no significant difference is observed whether or not one end of the model has a gap. For the drag coefficient on the other hand this difference of leaving one end of the flat plate untaped is noticeable. However, it can not be seen in the measurement however tends to be higher in case no gap is present. Due to the gap some 3D vortices might cause the model to vibrate more, causing this bigger error in the measurements. Based on these results it is however valid to state that the measurements in the LTT do not suffer from the fact that there is a gap on both ends. It should be noted that the vertical axis scale is different resulting in a more clear difference for the drag coefficient. However, zooming in on the lift coefficient reveals only a negligible difference which is within the measurement error.

The effect of the vibration due to the single support in the LTT is not tested and would need some further research to verify it has any influence on the results. The alternative configuration is also the direct cause of possibly another reason why the results of the LTT and WindGuard differ. By supporting the model on both sides a perfect alignment between the two balances is required and this tends to be hard sometimes. Furthermore, it is known that only the lower turntable is driven and that the upper turntable is turning under influence of the model. This could introduce some forces at the balance which are not originating from the flow. A zero run before and after the measurements are performed to minimise this effect and to improve the results.

The data from all other DUT airfoils gathered by WindGuard compare in a similar way as explained above to the data obtained from the measurements performed in the LTT. The resulting plots of all the different profiles can be seen in Appendix C. A typical example of the force coefficients is given in figure 4.16

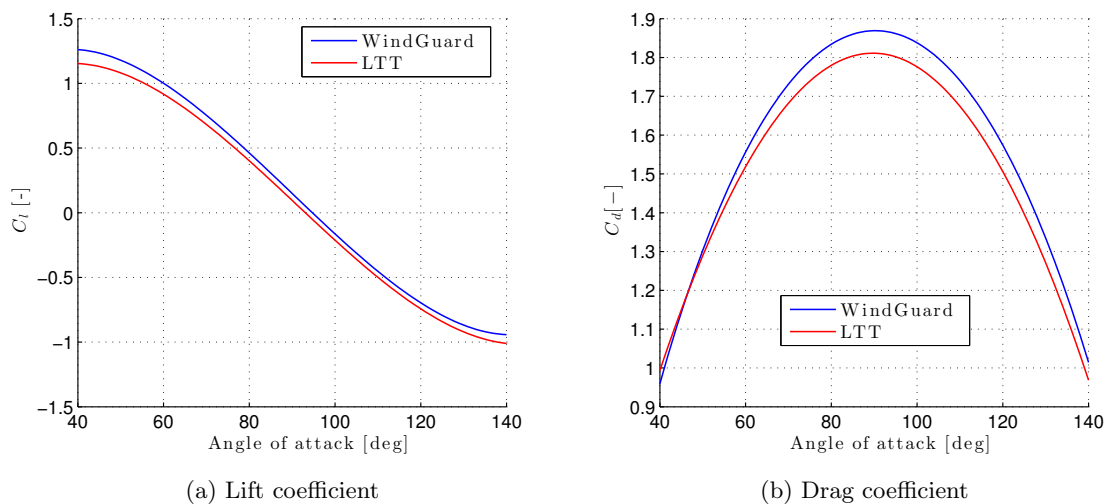


**Figure 4.16:** Lift and drag coefficient of the DUT-20-25, WindGuard ( $Re = 6 \times 10^5$ ) and LTT ( $Re = 1.5 \times 10^5$ )

For the lift coefficient this means an upwards shift over the entire range, however this tends to reduce for increasing leading edge thickness. For the drag coefficient it is observed that the angle of attack where the maximum is reached moves forward with increasing leading edge thickness which is similar as was found at the LTT. The maximum drag coefficient itself is significantly larger according to WindGuard, although the difference slightly reduces with increasing leading edge thickness. For the moment coefficient (not shown here) a constant downwards shift is observed over the entire range. From all these data it is possible to again create a relation between the leading edge thickness and the lift and drag coefficient at  $90^\circ$  angle of attack. The results can be seen in figure 4.17

In figure 4.17(a) it can be seen that for the lift coefficient obtained by WindGuard no clear relation is found with respect to the leading edge thickness as was the case for the results from the LTT. Here again it is clear that something is not entirely correct since for the flat plate a

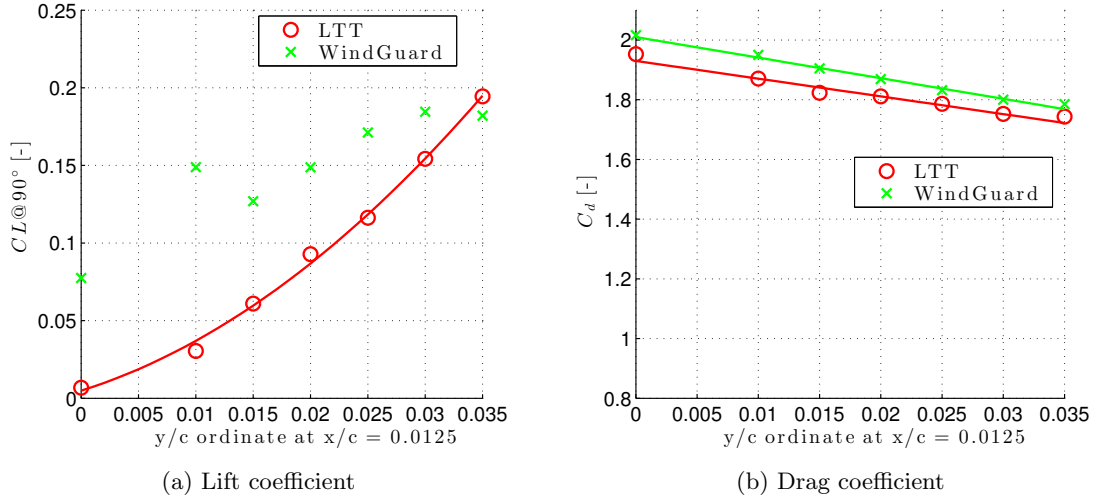


**Figure 4.17:** The lift and drag coefficient at  $90^\circ$  angle of attack in relation to the leading edge thickness according to: WindGuard ( $Re = 6 \times 10^5$ ), LTT ( $Re = 1.5 \times 10^5$ )

lift coefficient of zero should be found. As explained before it can be seen that with increasing thickness the results of WindGuard get closer to those of the LTT. A possible reason again is that for the smaller leading edges the lift force is too small and thus the accuracy and precision of the balances are not sufficient. With increasing leading edge thickness and as a consequence an increasing force the results become better. For the drag coefficient (see figure 4.17(b)) a linear decrease is found with increasing leading edge thickness which is given by the following expression.

$$C_{d_{max}} = 2.01 - 6.9(y/c) \quad (4.4)$$

An overview of the drag reduction and the flat plate drag is given in table 4.3. It can be seen that the maximum drag coefficient of the flat plate found by Timmer (2010) and WindGuard compares the best, while for the slope it is the LTT that compares the best with the results found by Timmer.

**Table 4.3:** Drag coefficient for the flat plate and drag reduction according to W.A. Timmer, LTT and WindGuard

	$C_d(y/c = 0)$	$\frac{dC_d}{d(y/c)}$
W.A. Timmer	1.994	-5.44
LTT	1.93	-5.94
WindGuard	2.01	-6.9

---

## Chapter 5

---

# CFD Analysis

In this chapter the implementation of Computational Fluid Dynamics (CFD) is discussed. The NUMECA software *FINE<sup>TM</sup>/Open* is used to simulate a 2D flow around the models at 90 degrees angle of attack. CFD has the opportunity to simulate the flow without being bounded by a solid wall. This eliminates the necessity for any corrections which could introduce unwanted errors. The CFD part of this research is intended to merely support the wind tunnel tests. It is chosen to work with the RANS simulation (Reynolds average Navier-Stokes) rather than a Large eddy simulation which means that the quantitative meaning of the results is subordinate to the qualitative meaning of the results given the large amount of separation. From the theory section 5.1 this will become more clear.

The need for CFD computation in addition to experimental testing comes forth of the limitations of wind tunnel testing. While the DU91-W2-250 model has a limited amount of pressure orifices on fixed span wise positions, the designed models created for this experiment are not equipped with pressure orifices at all. This confines the insight into the flow pattern around the complete model. During the experiments, measurement techniques are used which do not give the possibility to visualise the flow field. Using CFD these limitations can be overcome which results in a better understanding of the aerodynamic behaviour and is used in order to explain certain phenomena.

Section 5.1 discusses the theoretical background of CFD by providing the general Navier-Stokes equations and the derived Reynolds averaged Navier-Stokes equations. In section 5.2 the realisation of the geometry and computational domain is explained together with the grid generation. Finally in section 5.3 the flow setting and the turbulence modelling scheme will be shortly discussed.

## 5.1 Theoretical Background

In this section the theory behind the numerical flow solver is explained. First the general Navier-Stokes equations which describe the flow are given. Afterwards the Reynolds averaged Navier-Stokes equations will be discussed together with the effect on the modelling.

### 5.1.1 Navier-stokes equations

The derivation of the Navier-Stokes equations begins with an application of Newton's second law which is conservation of momentum. Neglecting gravitational forces and external body forces the conservation of momentum is given by:

$$\frac{\partial(\rho u_i)}{\partial t} + \frac{\partial(\rho u_i u_j)}{\partial x_j} = -\frac{\partial p}{\partial x_i} + \frac{\partial \tau_{ji}}{\partial x_j} \quad (5.1)$$

In this equation  $\rho$  is the density,  $u_i$  is the velocity component in  $i$  direction,  $p$  is the static pressure and the stress tensor is given by  $\tau_{ji}$ . In order to solve this equation additional information is required. In general this will be governed by the conservation of mass and energy .

The conservation of mass for a compressible fluid is given by the following equation:

$$\frac{\partial \rho}{\partial t} + \frac{\partial \rho u_i}{\partial x_i} \quad (5.2)$$

The Navier-Stokes equations are nonlinear partial differential equations which are assumed to properly describe the turbulent flow. It is however found that solving this set of equations is hardly possible and the difficulty is associated with the presence of the non-linear convective term.

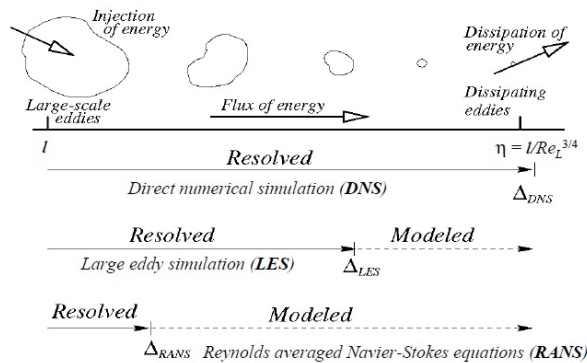


**Figure 5.1:** Extend of modelling for certain type of models Hossain (2012)

Depending on the Reynolds number this creates a wide range of time and length scales. A large Reynolds number results in a large range of scales which is not solvable with the current available computer capacity. A way to deal with this problem is to find an approximate solution for the equations by making simplifications and assumptions. Especially for highly turbulent flow these assumptions must be made. Two well known methods which result in a simplified expression are large eddy simulation (LES) and Reynolds averaged Navier-Stokes (RANS) simulation. Large eddy simulation still requires lots of computational power compared to RANS simulations. In figure 5.1 the different methods are represented and it is indicated up till which level of turbulent scale the flow is actually resolved and which part is modeled.

### Reynolds Averaged Navier-Stokes equations.

The *FINE*<sup>TM</sup>/open solver makes use of these so called RANS equations. They are derived by making a distinction in the flow variables between a time-averaged part ( $\bar{u}_i(x, t)$ ) and a fluctuating part ( $u'_i(x, t)$ ). The decomposition is of the following form:

$$u_i(x, t) = \bar{u}_i(x, t) + u'_i(x, t) \quad (5.3)$$

Inserting this in equation 5.1 results in the following equation for the averaged flow field.

$$\frac{\partial(\bar{\rho}\bar{u}_i)}{\partial t} + \frac{\partial(\bar{\rho}\bar{u}_i\bar{u}_j)}{\partial x_j} = -\frac{\partial\bar{p}}{\partial x_i} + \frac{\partial\tau_{ji}}{\partial x_j} - \frac{\partial\overline{\rho u'_i u'_j}}{\partial x_j} \quad (5.4)$$

Due to the decomposition and the averaging an extra term shows up in equation 5.4. The quantity  $-\overline{\rho u'_i u'_j}$  is called the Reynolds stress. This extra quantity leads to a closure problem which requires a model to solve the equation. One type of closure model is the eddy viscosity modeling. This makes use of the Boussinesq hypothesis to relate the Reynolds stress to the mean flow by a turbulent eddy viscosity ( $\mu_t$ ). There are various turbulence models available which find a solution for the eddy viscosity, see section 5.3

## 5.2 Computational Domain

Before any computation can be performed an appropriate domain needs to be defined. In this section it will be shortly explained how the geometries are created and transformed into a computational domain. Also the mesh generation will be discussed.

### 5.2.1 Domain

To simulate an external flow over an object a flow domain is created from which a solid object is subtracted. The geometry of the objects, in this case the designed profiles, are

created using SolidWorks and exported as parasolids to the HEXPRESS<sup>TM</sup> environment of the FINE<sup>TM</sup>/open software. HEXPRESS<sup>TM</sup> is an automatic unstructured grid generator producing only hexahedral cells. A build in CAD manipulator is used to design a surrounding box which represent the Wind tunnel boundaries. The imported geometry is subtracted from the created box to create a flow domain around a solid profile. In Figure 5.2(a) the resulting domain can be seen.

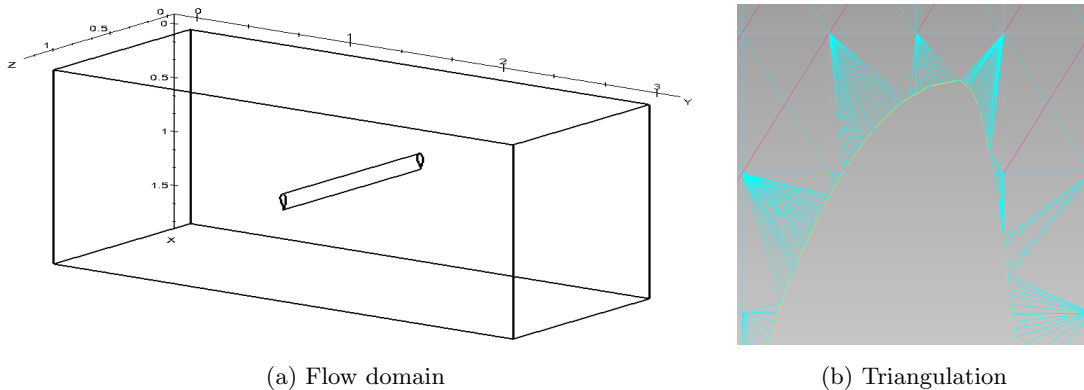


**Figure 5.2:** Computational domain and triangulation

The flow domain with dimensions 1.2 m x 1.8 m x 3 m is a simplified representation of the LTT wind tunnel. The justification of this simplification lies in the type of boundary conditions used which will be discussed hereafter. So far a solid representation of the computational domain is determined. The domain obtained from the CAD manipulation is now transformed into a discretised one by making use of triangulation of the surface boundary. In Figure 5.3(b) the triangulation near the leading edge of the profile 0.035 can be seen. The quality of the discretised domain is important since a poor triangulation leads to an incorrect mesh while good triangulation allows to capture the geometry correctly.

## 5.2.2 Mesh

### Boundary conditions

The generation of the mesh starts with identifying the type of boundary condition of each face of the domain. Since the computation will be 2D it is required that two mirror planes are present. The two faces between which the profile is spanned are identified as mirror planes. The four other faces which represent the boundary of the wind tunnel are identified as external boundary conditions. The other faces representing the profile are identified as solid boundaries. By using external boundary conditions the windtunnel wall is not simulated, this is the reason why a simplified representation of the windtunnel is allowed. The normal velocity component at the boundary of the the flow domain is able to transfer trough the boundary where it will be subjected to the applied boundary conditions. For all four faces the boundary conditions are similar and set equal to the environment of the wind tunnel during the experiments. This is a certain velocity in y-direction, a static temperature and

the values for  $k$  and  $\epsilon$  which originate from the chosen turbulence model (see section 5.3).

### Mesh generation

Using the mesh wizard the generation of the mesh is performed in different steps. First an initial mesh is created which surrounds the computational domain. This very coarse initial mesh is then adapted and refined so that it satisfies the geometry dependent criteria, any cells intersecting the geometry or located outside the domain are removed. The mesh is then projected onto the geometry in order to snap it onto it. An optimisation ensures that a high quality mesh obtained. Finally it is possible to insert high aspect ratio cell tangentially to a solid wall in order to capture the boundary layer. In Figure 5.3 an example of a mesh can be seen with a large amount of refinement near the model.

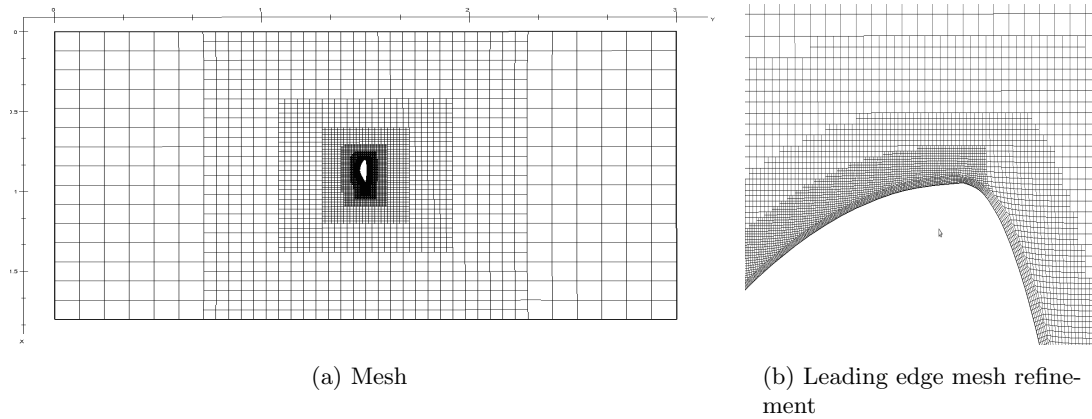


**Figure 5.3:** Mesh

The amount of layers required and the size of the first cell can be computed and is determined by:  $y^+$ , a reference length, the kinematic viscosity of the fluid and a reference velocity.  $y^+$  is a non-dimensional distance from the wall and is together with the wall function responsible for how well the boundary layer is resolved. The non-dimensional wall distance is determined as follows

$$y^+ = \frac{yu_\tau}{\nu}, \quad (5.5)$$

where  $y$  is the distance from the wall,  $u_\tau$  is the friction or shear velocity and  $\nu$  is the kinematic viscosity. There are two different approaches to resolve the near-wall region where very small turbulent fluctuations are present. The first approach is called the near wall-model. The mesh is refined in such a way that it is possible to resolve to flow in the boundary layer. This requires a  $y^+ < 5$  in order for the first cell to lie in the viscous sublayer. This approach requires considerable amount of refinement near the wall and therefore it will also require more computational power. A second approach is called the extended wall function. Instead of refining the mesh near the wall a semi-empirical function is used to approximate the flow in this near wall region. Depending on the choice of  $y^+$  the part which is approximated is bigger or smaller. If  $y^+$  is smaller than five then the first node is positioned in the viscous sublayer and only a very small part is approximated. When  $y^+$  is larger 20 the first node is

in the log layer which results in a bigger part that needs to be approximated. The manual of **Numeca FINE<sup>TM</sup>/Open** is used in order to chose the appropriate settings.

## 5.3 Flow Solver

When the mesh is generated the flow settings can be done in the flow solver. Various parameters can be controlled like the actual flow properties, the values of the boundary and initial conditions, the desired output and many more. In this section the turbulence model will be discussed in more detail, other numerical parameters will shortly be discussed.

### 5.3.1 Turbulence model

As indicated in section 5.1.1 a turbulence model is used to relate the additional Reynolds stress to the mean flow by a turbulent eddy viscosity  $\mu_t$ . The turbulence models available are either one-equation models (Spalart-Allmaras, SARC) or two-equation models (k- $\epsilon$ , k- $\omega$ ,...). The one-equation models are low cost and designed for wall-bounded flow in aerospace applications. For completely separated flow it is however found that the solution is less accurate. From the two-equation models the k- $\epsilon$  is chosen to be used in this CFD analysis. The general k- $\epsilon$  model is known to be robust and well applicable for a variety of turbulent flows. It is chosen to use the model with extended wall function which means that the flow near the wall will be approximated rather than resolved. The model is based on the transport equations for the turbulent kinetic energy (k) and its dissipation rate ( $\epsilon$ ). Both quantities need to be estimated in order to define the correct boundary and initial conditions.

The turbulent kinetic energy (k) is dependand on the fluctuating part of the stream wise velocity component  $u''$  as given in equation 5.6

$$k = \frac{3}{2}(\sqrt{u''^2})^2 \quad (5.6)$$

The fluctuations can be determined from the turbulence intensity ( $T_u$ ) and and the free stream velocity  $U_{ref}$ . For the turbulence intensity the value of the LTT (0.015 %)is used .

$$T_u = \frac{\sqrt{u''^2}}{U_{ref}} \quad (5.7)$$

Now the dissipation rate can be determined using the following relation.

$$\epsilon = C_\mu \frac{\mu}{\mu_T} \frac{\rho_{ref} k^2}{\mu} \quad (5.8)$$

Where  $C_\mu$  is an empirical dimensionless constant with a value of 0.09,  $\frac{\mu}{\mu_T}$  is the turbulent viscosity ratio, which for external flow is assumed to be 1 and  $\rho_{ref}$  is the density and  $\mu$  the dynamic viscosity.

### 5.3.2 Numerical parameters

Besides the turbulence model there is a variety of different parameters which influence the flow solver and that can be adjusted and adapted to each case separately. Since the CFD computation in this research is not the main goal no detailed investigation is performed to optimise all parameters for the given problem. A short overview of some of these parameters is given below where in most cases the default value is used, except in case of the preconditioning.

#### Multigrid parameters

The application of a multigrid causes the solution to converge faster. A default setting of four is used including the correction damping and the coarse grid initialisation. Correction damping removes high discontinuities between grid interpolations and smoothens the results to ensure robustness. The coarse grid initialisation performs a preliminary flow calculation on a coarser mesh, created by the solver, such that a rapid estimation of the flow is provided. The computations then includes a finer grid each time one of two criteria are met, either maximum number of cycles per grid level or convergence criteria on each grid level.

#### Numerical scheme

The numerical schemes applied are kept as default which means for the spatial discretisation a 2nd-order central scheme. The time marching of the governing equations towards a steady steady solution is performed according to a Runge-Kutta scheme, this in combination with a CFL number of 3.

#### Preconditioning

The preconditioning is the only numerical parameter which is not activated by default. Preconditioning can be used in any case but is strongly recommended to use in case when the Mach number is smaller than 0.3. The parameter  $\beta$  is the value that determines the preconditioning and has a default value of 3. In the next chapter it will be shown based on some results that this value of 3 was not satisfying, a value of 30 is found to be better. The preconditioning is in general not necessary but improves the converges of the solution, furthermore it is shown in the next chapter that not only the convergence changes but also the actual solution.



---

# Chapter 6

---

## CFD Results

In chapter 4, where the experimental results are discussed, it is pointed out that some phenomena can not be explained without further analysis. In this chapter the force outputs are used to establish a relation between the maximum drag coefficient and the leading edge thickness and further analysis is performed based on the CFD results. Pressure distributions and flow visualisations are used to explain how it comes that the maximum drag coefficient reduces with increasing leading edge thickness. Before discussing the results of the various models an evaluation is performed of different computational parameters. In section 1 it is evaluated how the mesh, the preconditioning and the boundary conditions influence the solution of the computation. At the end of this first section an overview is presented of the used computational parameters for all models. In section 2 the force coefficients of the designed models are discussed and their relation to the leading edge thickness. In the final section the pressure distribution is discussed together with the flow visualisation around the nose in order to explain the reduction of the drag due to an increasing leading edge thickness.

### 6.1 Evaluation of computational variables

An evaluation of three characteristics of the computation (mesh, preconditioning and boundary conditions) is given in this section. It will be explained why the three parameters are chosen as they are based on the simulation of the flat plate. The flat plate is chosen as reference due to the known pressure distribution (Fage et al. (1927)). At the end of this section an overview is given of the computational setting used for the designed models (20 cm chord) and the DU91-W2-250 (15 cm chord).

### 6.1.1 Mesh

First the effect of the mesh on the computation will be shown and it is discussed why certain meshes perform better. External boundary conditions are used to run these simulations in order to investigate the effect of the mesh. This eliminates the need for blockage correction and therefore reduces the chance on errors (see section 6.1.3 ). However, this means that the results only can be used to compare with corrected wind tunnel data. A different mesh is needed if you want to compare with uncorrected data since then the tunnel walls need to be simulated to. The computations are performed using a preconditioning with a  $\beta$  value of 30. The effect of this  $\beta$  value on the simulations and the reason for choosing 30 will be explained shortly after.

In the previous chapter it is explained that the refinement of the mesh can be performed in various ways and up to a chosen level. This level of refinement and the position of the refinement will have an influence on the results. In general a finer grid better simulates the actual flow around the object at the cost of more computational time. It is then the goal to find a good balance between accuracy of the solution and the computational time required to solve the problem. It is however found that with the current used solver and the given amount of separation more refinement (especially in the wake) does not necessarily results in better simulations. To show the effect four different meshes will be discussed which are depicted in appendix D and briefly describes as follows:

- Mesh 1 : The first mesh is a coarse mesh counting about 3500 cells where the upper and lower surface are refined only a little and the refinement does not extend in the far wake.
- Mesh 2 : This mesh contains about 43000 cells resulting from a stronger upper and lower surface refinement. This increased refinement will make it possible to better simulate the rounded leading edge. The wake is however not captured with this refinement.
- Mesh 3 : The third mesh ( $\approx 128\ 000$  cells) has a refinement on the upper and lower surface plus a refinement in the wake region.
- Mesh 4: The last mesh contains the most amount of cells ( $\approx 150\ 000$  cells) since the frontal and rear surface are refined considerably. No extra refinement is placed around the leading edge or in the wake.

In figure 6.1(a) the pressure distribution of the flat plate for the four different meshes is given. Although the meshes are significantly different in amount of cells and location of refinement no major differences are visible in the figure. The only main difference that is found is the base pressure for the third mesh is smaller compared to other meshes and smaller than according to the measurement from [Fage et al. \(1927\)](#).

Since from this analysis no distinct conclusion can be made on the mesh it is chosen to perform a similar pressure coefficient analysis for the DU91-W2-250. The simulated pressure

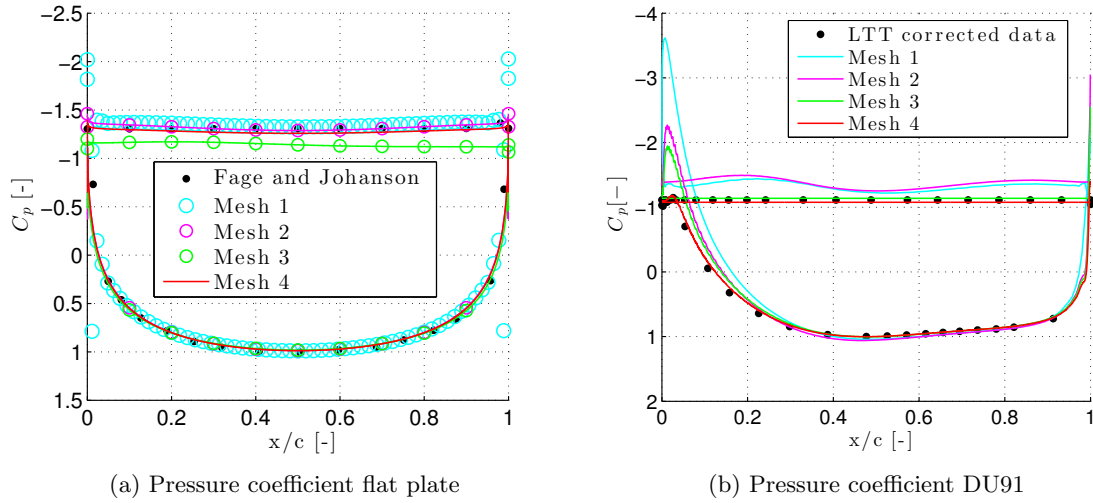


**Figure 6.1:** Pressure distribution at  $90^\circ$  angle of attack for different setting of preconditioning (Including reference of measurement Fage et al. (1927))

distribution are compared to the results from the wind tunnel experiment in the LTT (see sec 4.1). The effect of the mesh refinement on the pressure distribution for the DU91-W2-250 can be seen in figure 6.1(b)

Its clear that for the DU91-W2-250 more distinct differences are present due to a change in mesh. This could be due to the rounded leading edge which has a less fixed separation point compared to the sharp edge of the flat plate. Therefore a better mesh provides better estimation of the separation point and consequently a better pressure distribution can be calculated. Mesh 1 and 2 which are the most coarse show an undulating base pressure which is originating from the circulation in the wake. Mesh three and four have more refinement on the upper surface and yield a more constant base pressure which compares better to the time averaged measurement. For the lower surface it can be seen that from the stagnation point to the trailing edge no significant difference is found. This confirms that in case of a sharp edge/fixed separation point the mesh has no big influence on the pressure distribution as indicated for the flat plate. From the stagnation point to the leading edge no sharp edge is present and this is also noticeable in the pressure distribution which is different for the four meshes. The coarse mesh shows a very large suction peak on the leading and as the meshes gets more refined in this region this peak reduces to the expected value which is almost reached with mesh 4. From this investigation it can be conclude that mesh 4 is the most appropriate mesh to use of the four suggested options. Especially because the leading edge is captured the best and this is important considering the relation which is investigated. However, it can not be excluded that the use of another mesh could lead to equally good or even better results. A different mesh could for example have more cells or different areas refined capturing more effects. However it is important to make sure that the solution converges.

Finally it is observed that in order to determine the effectiveness of the mesh it is not sufficient to only have a look at the drag coefficient. Like for example for the coarse mesh a

good estimation of the drag coefficient is obtained although the pressure distribution is not comparable to the actual pressure distribution. This is possibly because both sides are poorly simulated and therefore cancel each other in a positive way regarding the drag coefficient. When looking at the lift coefficient in this case it is significantly larger than what is expected. A overview of the lift and drag coefficient for the different meshes is given in table 6.1.

**Table 6.1:** Effect of mesh on the lift and drag coefficient at  $90^\circ$ , DU91-W2-250

	$C_d$	$C_l$
Mesh 1	1.79	0.37
Mesh 2	1.92	0.26
Mesh 3	1.67	0.23
Mesh 4	1.72	0.19
LTT corrected data	1.78	0.2

It can be seen that for mesh 1 the best approximation of the drag coefficient is found although the pressure distribution is bad. This is explained by looking at the lift coefficient which is much higher than what is found during the wind tunnel experiment. The pressure distribution of mesh 2 shows an improvement of the nose simulation resulting in a lower lift coefficient but no change in base pressure, therefore a increase in drag coefficient is observed. For mesh 3 a decrease in base pressure is found while the pressure around the nose has not changed much which results in a drag coefficient which is too low. Finally for the fourth mesh a good estimation of the pressure around the nose is given resulting in a good estimation of the lift coefficient. A slightly over estimation of the base pressure now results in a drag coefficient which is lower than what was found during the wind tunnel experiment. The connection between the lift coefficient and the drag coefficient will be further explained later on in this report.

### 6.1.2 Preconditioning

Prior to the mesh evaluation it is stated that for the preconditioning parameter  $\beta$  a value of 30 is used. Now it will be explained why this value is used and how it is determined. Ideally the preconditioning only makes the solution converge faster without influencing the accuracy however it is noticed that the preconditioning also has an influence on the solution rather than only on the convergence. The effect on the other hand from the value on the solution is not clearly described in any literature. By using again the flat plate as a reference different values are tried to see which results in the best solution and how it effects the simulation.

It is allowed or recommended to use preconditioning in case of a mach number smaller than 0.3 which is a used criterion that indicates that the flow can be assumed as incompressible. In order to simulate the models with a comparable Reynolds number as during the wind tunnel experiment ( $Re = 150\,000$ ) a velocity of 11m/s is used which yields a Mach number of only 0.03. In the manual of **Numeca** an indication of the  $\beta$  value is given based on the Reynolds number furthermore a default value of 3 is given. In the figure 6.2(a) the effect can be seen on the pressure distribution of a flat plate between different simulations with and without preconditioning and three different values for  $\beta$ .

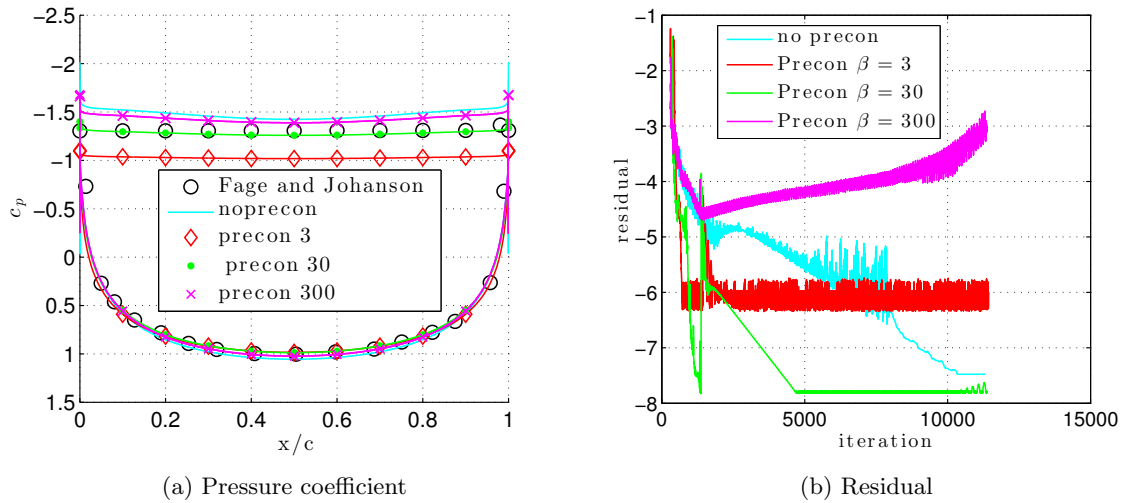


**Figure 6.2:** Pressure distribution and residual of a flat plate at  $90^\circ$  angle of attack for different setting of preconditioning (Including reference of measurement [Fage et al. \(1927\)](#))

It is observed that for the lower surface the preconditioning has no significant effect on the pressure coefficient while for the upper side a big difference is detected. [Fage et al. \(1927\)](#) give the pressure distribution for a flat plate at  $90^\circ$  angle of attack based on a wind tunnel test. In comparison to that the simulation without preconditioning gives a base pressure which is lower and less constant resulting in a drag coefficient of 2.12. For the default value of the preconditioning parameter ( $\beta = 3$ ) the base pressure reduces strongly which results in a drag coefficient of 1.78. Increasing the parameter to 30 shows a rise in the base pressure while keeping it more or less constant resulting in a drag coefficient of 2.01. Increasing the preconditioning factor further to 300 (3, 30 and 300 are suggested in the manual of Numeca) makes the simulation go towards the solution without preconditioning, which means less constant and a drag coefficient which is too high. It is given that too small or too big values of  $\beta$  may lead to divergence and to a too dissipative solution, therefore this evaluation is important.

In figure 6.2(b) it can be seen what effect the preconditioning has on the convergence of the solution. The residual is depicted which indicated how fast the solution solution converges. A smaller residual means that the simulation is performed with greater accuracy and the faster the residual reduces the faster the solution converges.

It is concluded that the preconditioning not only has an effect on the convergence of the solution but also on the actual output. In this case a too small preconditioning factor underestimated the base pressure while a too high value for  $\beta$  results in overestimating the base pressure. The best results are found for a preconditioning value of 30 which is therefore used during all other simulations. It should be mentioned that this is in combination with mesh 4, a different mesh could required a different preconditioning value.

### 6.1.3 Boundary conditions

The boundary conditions do play a important roll when simulations are performed and in order to accurately model the experiments performed in the wind tunnel it would be required to simulate the wind tunnel walls as well. This would mean that instead of using external boundary conditions, solid boundary conditions are needed.

When solid boundary conditions are applied the six faces of the flow domain (see figure 5.2(a)) are described as follows. The face through which the flows enters the flow domain is the inlet and where the flow leaves the domain is called the outlet. The upper and lower face of the domain are identified as solid walls while the left and right face are identified as mirror planes (2D simulation). The upper and lower solid boundary is simulated as an Euler wall which means that at the boundary there is a slip condition resulting in a non zero velocity and therefore no boundary layer growth over the tunnel wall. During the actual wind tunnel test this is of course not valid but this Euler wall simulations can be justified since in the LTT the test section is slightly diverging in such a way that it compensated for the boundary layer growth over the tunnel wall in case of an empty test section for moderate velocities. However, it will turn out that the boundary layer growth has an impact due to the large amount of suction in the wake. The effect of applying the solid boundary condition in comparison to the external boundary conditions is depicted in figure 6.3(a). In general it is like this that the CFD with external boundary conditions replicates free flow which compares to wind tunnel test results after corrections. CFD with Solid boundary conditions on the other hand required blockage corrections similar to those applied for the wind tunnel. Ideally the uncorrected wind tunnel results are compared to uncorrected CFD results in order to validate each other.

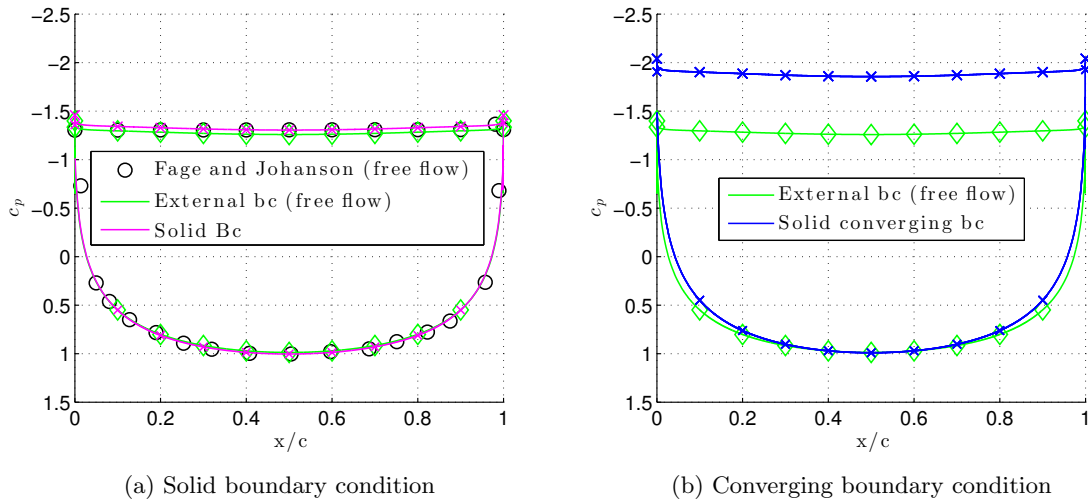


**Figure 6.3:** Pressure distribution of a flat plate at  $90^\circ$  angle of attack for different boundary conditions

It can be seen that the effect of creating a solid wall and therefore constricting the flow in a fixed area has no significant effect in this simulation. The pressure on the lower surface remains unaltered while for the upper surface only a slight increase is observed. Looking at the drag coefficient this rises from 2 to 2.01 (for using solid boundary conditions) while the first one does not need to be corrected, the second does for blockage (see chapter 2). This

results in a drop to 1.66 which is too low for a flat plate.

In theory it should be that the drag coefficient after corrections of the solid boundary wall simulation is identical to the drag coefficient of the external boundary simulation. In this case it is clear that for the solid boundary condition a too low drag coefficient is obtained. The reason for this poor simulations is rather uncertain and can have multiple causes. A reason that is looked at is the boundary layer growth on the tunnel wall. Initially these wind tunnel walls are simulated as an Euler wall as explained before. It is however possible that due to the large amount of suction in the wake the boundary layer increases more than expected.

In order to see if this assumption of excessive boundary layer growth is valid two approaches are possible. Either the solid walls are no longer simulated as Euler walls and the actual boundary layer is determined. Secondly it is possible to assume a fixed boundary layer growth on the tunnel which is created by converging tunnel walls. By making the flow domain converging it is possible to keep the slip condition at the wall (Euler) which simplifies the simulation and the required computational time significantly. Where the first option is physically more correct and better in agreement with the actual experiment the second option is good enough to at least give an indication that the excessive boundary layer growth could be the reason why solid boundary condition (with straight Euler walls) do not yield the correct results. For simplicity and due to the limited amount of time it is chosen to simulate a boundary layer growth with a converging wall.

In order to verify the effect of the boundary layer growth a strong converging wall (15 cm at each side) is created. In figure 6.3(b) the pressure distribution is given for both the external boundary conditions and the solid boundary conditions with converging tunnel walls for simulating the boundary layer growth. It is clear that in this case there is a significant increase in base pressure while on the lower surface only minor changes are visible. For the drag coefficient this means that it rises from 2 to 2.55. Correcting this for blockage using the equations as described in chapter 2 results in a drag coefficient of 2.01 which is slightly higher than for the external boundary conditions. This indicates that a plausible reason why solid boundary conditions with a straight Euler wall perform badly might be due to a large boundary layer growth. To use the solid boundary conditions in this case, where a large amount of suction is present in the wake, it needs further investigation regarding the boundary layer growth. Either it can be done by simulating the boundary layer or by measuring it during wind tunnel experiments. This, the influence of strong suction in the wake in the boundary layer growth, is however outside the scope of this current investigation and could be an interesting subject for future projects. Due to the current issue with the solid boundary condition all presented results hereafter are obtained from simulations with external boundary conditions.

#### 6.1.4 Overview computational settings

Previously in this chapter different computational settings are evaluated. An overview is presented where most used setting of the simulations, from which the results follow, are given.

**Table 6.2:** Input parameters for the numerical simulations

Parameter	models	DU91-w2-250
Mesh	4	4
Preconditioning ( $\beta$ value)	30	30
Boundary conditions	External	External
Initial velocity	11 m/s	50 m/s
k	$0.0408 \text{ m}^2/\text{s}^2$	$0.8483 \text{ m}^2/\text{s}^2$
$\epsilon$	$11.46 \text{ m}^2/\text{s}^2$	$4904 \text{ m}^2/\text{s}^2$

In table 6.2 it can be seen that the main difference between the designed models and the DU91-W2-250 is the initial velocity and the parameters k and  $\epsilon$  which are influenced by the velocity (see section 5.3). For the mesh in all cases a type four mesh is used. This does not mean that in all cases the mesh is identical since it will alter with the shape and chord of the profiles. However the construction of the mesh is identical with considerable refinement on all surfaces but no extra refinement in the wake. In the following section the results will be shown.

## 6.2 Force coefficients

In this section the results of the CFD are presented and discussed. The force coefficients of all models are given and a relation between the leading edge thickness is presented. A distinction is made between the flat plate which is simulated at various angles of attack and the other designed profiles which are only simulated at  $90^\circ$  angle of attack. The results for the DU91-W2-250 will be given in the next chapter where the computational results are compared with the experimental results.

### 6.2.1 Flat plate

The flat plate is simulated over a range of angles similar to those during the wind tunnel test. This makes it possible to not only discuss the maximum drag coefficient but also the shape of the polars and see in which regions the simulation perform as expected or not. The ideal flat plate theory (eq 2.2) is used to validate these results while in the following chapter it will be compared to the results of the wind tunnel experiments. In figure 6.4 the lift and drag coefficients are depicted. It is chosen to only perform the simulation over half the domain and then duplicate the results since it is assumed that the lift coefficient and drag coefficient of the flat plate are anti-symmetric and symmetric around  $90^\circ$  respectively.

For both the lift and drag coefficient it is found that near  $90^\circ$  angle of attack the simulation and the ideal flat plate theory are almost identical. Only for the drag coefficient a minor over estimation is found. The deviation from the theory grows towards the end of the angle of attack range. This again could be explain due to the fact that for the ideal flat plate

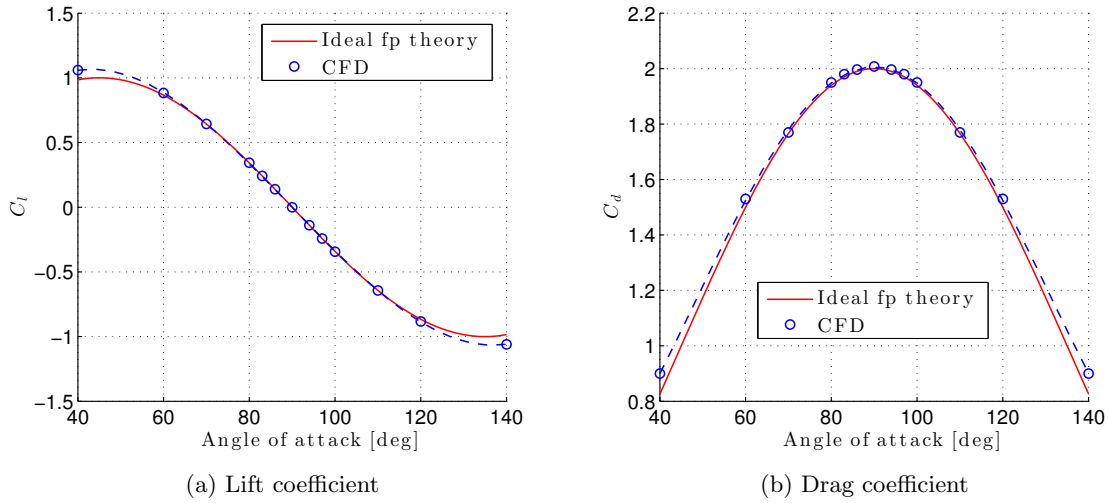


**Figure 6.4:** Theoretical and numerical lift and drag coefficient for the flat plate,  $Re = 1.5 \times 10^5$

theory no viscous drag is taken into account. Furthermore it is possible that some of the computational parameters, which are discussed above, are optimised for an angle of attack of  $90^\circ$  and further away from this  $90^\circ$  angle of attack a different mesh or different value for preconditioning could lead to an improvement of the result in this region. Investigating this in detail would go beyond the scope of this project since the main goal is to investigate the relation between the maximum thickness and the maximum drag coefficient which is found at about 90 degrees angle of attack.

### 6.2.2 DUT airfoils

All DUT airfoils, except the flat plate, are tested only at an angle of attack of  $90^\circ$ . In order to simulate all models over a larger angle of attack range to compare the polars with those of the wind tunnel experiment would be too time demanding and since CFD is not the main area of investigation this is not done. With the results at 90 degrees angle of attack it is possible to create a similar relation between the maximum drag coefficient and the leading edge thickness as is determined from the wind tunnel experiment. The results for the lift and drag coefficient are depicted in figure 6.5

The lift coefficient (see figure 6.5(a)) is related to the leading edge thickness with a third degree polynomial that starts at zero for the flat plate to a maximum of 0.201 for the 0.035 profile. For the drag coefficient (see figure 6.5(b)) a linear decrease with the leading edge thickness is observed. It is chosen to exclude the flat plate drag coefficient from the linear relation since it reduces the accuracy of the relation significantly for the other models. Based on this linear relation the drag coefficient of the flat plate is found to be 1.96 rather than the 2.01 value from the CFD simulation. Both are acceptable values for the maximum drag coefficient of a flat plate although that the 2.01 is above the theoretical maximum. The lift

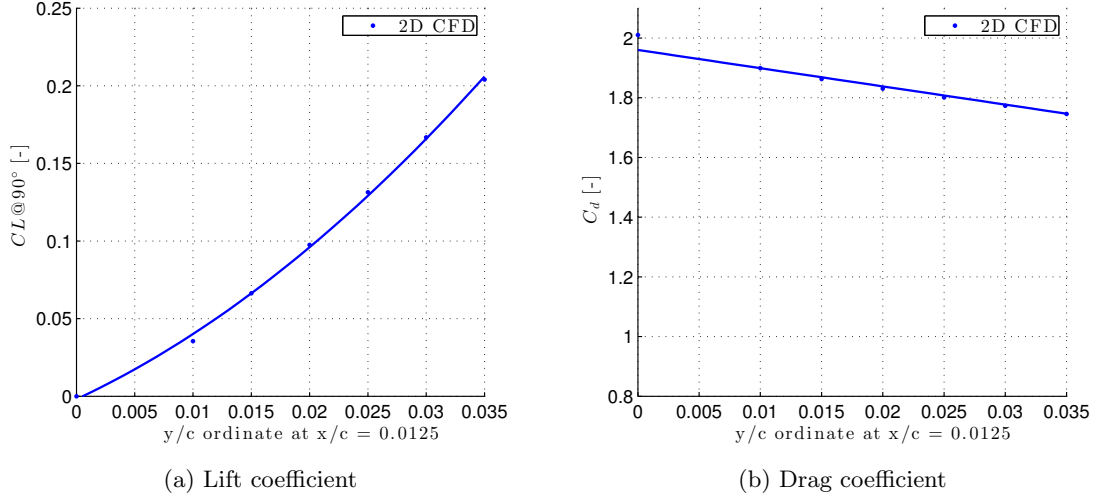


**Figure 6.5:** Lift and drag coefficient vs the leading edge thickness,  $Re = 1.5 \times 10^5$

coefficient and drag coefficient at  $90^\circ$  angle of attack in relation to the leading edge thickness is given by the following two expressions:

$$C_l = 69.63(y/c)^2 + 3.5(y/c), \quad (6.1)$$

$$C_d = -6.1(y/c) + 1.96. \quad (6.2)$$

From only these force coefficients it is not possible to identify the reason for this behaviour. Therefore in the next section further analysis is done using pressure distributions and flow visualisations.

### 6.3 Flow analysis

From both the experimental and numerical results (comparison follows in next chapter) similar relations are found between the lift and drag coefficient at  $90^\circ$  angle of attack and the leading edge thickness. From the performed experiments it was not possible to shed a light on the explanation of these relations. The only statement possible so far is based on the wake analysis of the DU91-W2-250 (see section 4.1.2), where it was found that the shedding frequency is similar to that of the flat plate at  $90^\circ$  angle of attack. This would suggest that it is not the wake strength that is changing with leading edge thickness. In this section pressure distributions and flow visualisations will be discussed in order to investigate what phenomena are causing the decrease in maximum drag coefficient with increasing leading edge thickness.

### 6.3.1 Pressure distribution

The CFD makes it possible to obtain pressure data from the models while this was not possible during the experimental testing since the models are not equipped with pressure tap holes. The pressure distribution for all the models is given in figure 6.6

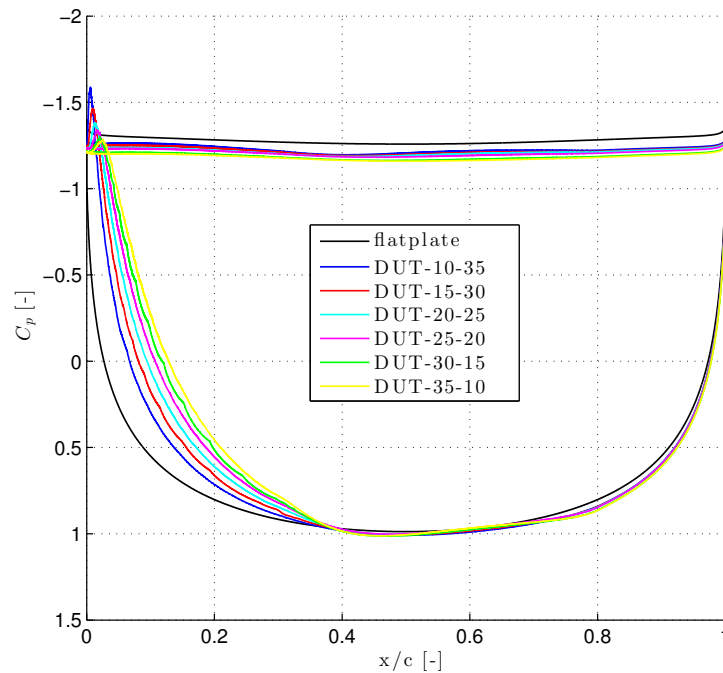


**Figure 6.6:** Pressure distribution for all the DUT airfoils,  $\text{AOA} = 90^\circ$

It is clearly visible that the only region where there is significant difference in the pressure distribution is on the lower surface from the stagnation point towards the leading edge of the profile. A steady reduction in suction peak pressure at the leading edge is observed with increasing thickness, furthermore it can be seen that the pressure decrease (from stagnation point to leading edge) for thicker profiles is more gradual than for thinner profiles. From the stagnation point to the trailing edge no difference is observed with the flat plate which is as expected since the trailing edge is similar to a flat plate. For the base pressure it is noticeable that only the flat plate has a lower pressure compared to the other models. This also explains why in figure 6.5(b) the drag coefficient of the flat plate is larger than according to the trend which is based on the other models and therefore it could be justified to not include the flat plate data in the relation of the drag coefficient and the leading edge thickness.

The availability of the pressure distributions also enables us to determine the lift and drag coefficient in a rather different way. Instead of integrating from leading to trailing edge it is also possible to integrate the upper and lower side separately from the thickest point to the leading edge and trailing edge respectively which results in a lift and drag coefficient of both the lower and upper (or front and rear surface respectively) separately. The results of the integrations for the different profiles is given in table 6.3.

**Table 6.3:** Lift and drag coefficient from front and rear surface separate

Airfoil	Front surface		Rear surface		Total	
	Cl	Cd	Cl	Cd	Cl	Cd
DUT-10-35	0.03	0.67	0.01	1.23	0.04	1.9
DUT-15-30	0.06	0.64	0	1.22	0.06	1.86
DUT-20-25	0.09	0.62	0	1.21	0.09	1.83
DUT-25-20	0.13	0.6	0	1.2	0.13	1.8
DUT-30-15	0.16	0.58	0	1.19	0.16	1.77
DUT-35-10	0.20	0.56	0	1.18	0.20	1.74

What catches the eye first is the zero lift coefficient for the rear surface which is also as expected, while for the front surface an increase in lift coefficient is given with increasing leading edge thickness. This increase in lift coefficient on the front surface goes together with a decrease in drag coefficient. Furthermore also the rear surface, although it is minor, shows a decrease in drag coefficient. By looking at the pressure distribution along the contour of the profiles it is possible to better understand the behaviour which is detected in the table above. In figure 6.7 the pressure along the contour is given for the DUT-10-35 and the DUT-35-10, which are the models that are the most different from each other and therefore should show the best what is changing. It can be seen that for the thickest profile that the part on the upwind side, where suction is present, is larger compared to the thinnest profile. Where for the DUT-35-10 the suction is present on about 12 % of the upwind surface for the DUT-10-35 this is only on about 6%. When from this area the resulting force is determined it can be seen that this will point in the upward and forward direction. A larger area result in a larger force, therefore in case of the DUT-35-10 the force will be significantly larger. When finally decomposing this resulting force it becomes clear that the larger this force the bigger the contribution to the lift coefficient and the more the drag coefficient will be reduced. For all the other models which are in between these two the same observation is done. So for an increase in leading edge thickness the suction area on the upwind side of the profile increased which results in an increasing forward pointing force. The pressure distribution along the contour for the other airfoils can be seen in appendix E. The presence of the forward pointing force on the leading edge is thus the explanation for the reduction found during the experiments and simulations. This is not in agreement with Montgomerie who explained that a decrease in drag coefficient for increasing (leading edge) thickness is due to later separation of the flow. Further discussion of this founding will be done later by making use of the streamlines around the leading edge.

Another effect that can play a roll in the drag reduction/lift increase, situated near mid-chord, is the increasing maximum thickness. The models are designed in such a way that for an increase in leading edge thickness the maximum thickness also increases. This is done to maintain the same elliptical shape of the leading edge up to 33% of the chord. In figure 6.7(b) it can be seen that this results in a steeper gradient to go from the maximum thickness to the flat plate trailing edge. This steeper gradient causes the resulting force which act on that part to be pointing at a certain angle which is more upwards compared to the thinner model. Keeping the same force but changing the direction more upwards (and thus a larger maximum thickness) results in a smaller contribution to the drag coefficient and a bigger

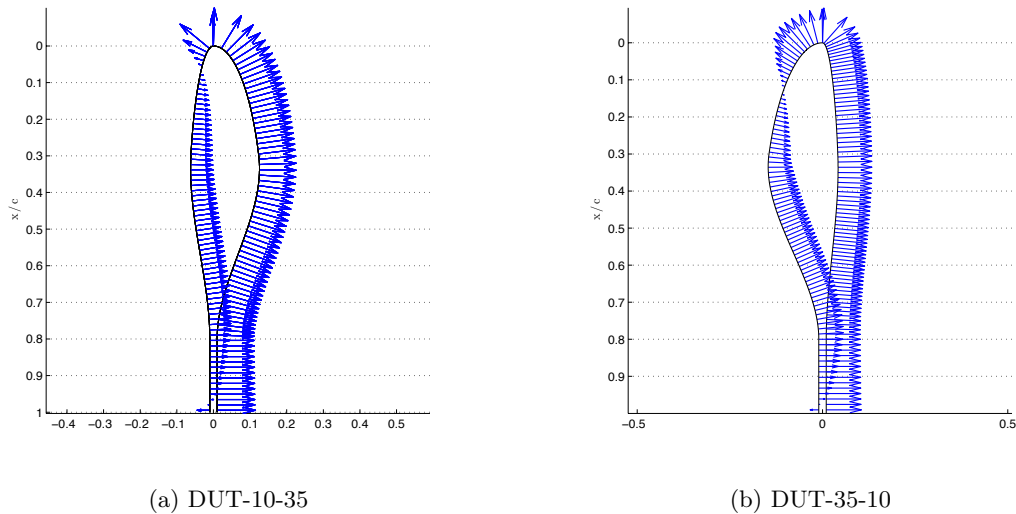


**Figure 6.7:** Pressure distribution along the surface contour,  $Re = 1.5 \times 10^5$

contribution to the lift coefficient. For example in figure 6.7(a) it can be seen that for the thinner upwind surface almost 100 % of the pressure force is converted in a drag force around mid chord. Therefore it is plausible that this maximum thickness also contributes to the drag reduction/lift increase together with the leading edge thickness. In order to make a conclusion on the effect of the maximum thickness further analysis is needed in this area for example by simulating profiles with similar leading edge thickness but varying maximum thicknesses. Also the location of the maximum thickness could be altered to verify any possible effect of this parameter. This however is not discussed in this report could be an interesting project in the future.

### 6.3.2 Flow visualisation

So far it is known that the reduction in drag with increasing leading edge thickness is caused due to an increasing forward pointing force on the leading edge. By looking at the streamlines around the leading edge it is possible to get a better insight in what is going on and why a larger suction part is present for the thicker leading edge. In figure 6.8 the streamlines around the DUT-10-35 are depicted.

A velocity increase over the profile can be observed together with a well defined bubble boundary which encloses the circulating flow. This is a similar flow behaviour as a flat plate which is described in chapter 2. For all other models these far field streamlines will look almost identical and no additional information can be extracted from it regarding the drag reduction. Better insight can be gained in the region around the leading edge which is marked by the red rectangular box in the figure. A close-up of this region for all six models (from  $(\frac{y}{c})_{x/c=0.0125} = 0.010$  to  $(\frac{y}{c})_{x/c=0.0125} = 0.035$ ) is given in figure 6.9. Significant zooming is

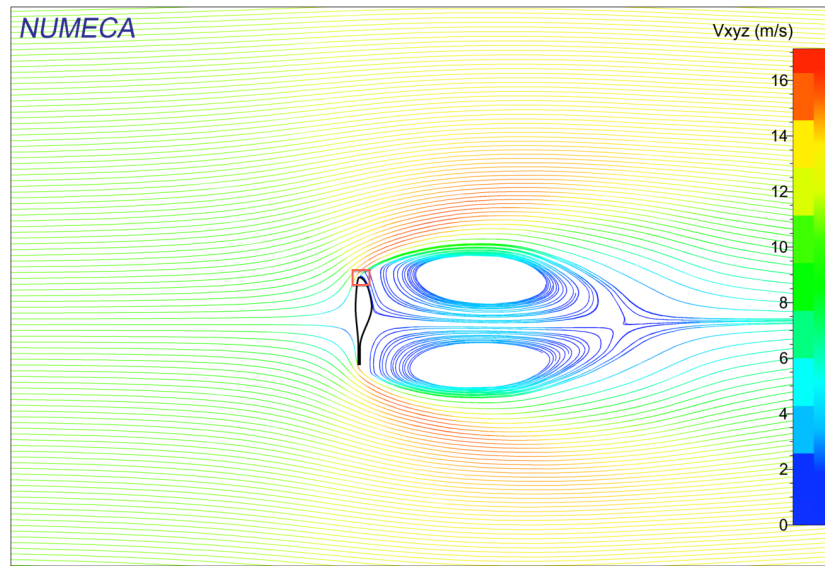


**Figure 6.8:** streamlines around the DUT-10-35

required to capture the effect on the leading edge, this causes that only a small part of the profile is seen on the figures. For the part which can not be seen the flow is attached up to the trailing edge where well defined separation occurs due to the sharp edge.

For the thinnest model (figure 6.9(a)) it can be seen that for almost the complete upwind surface the flow is attached and separation occurs just ahead of the leading edge. On the downwind surface the circulation causes the flow to move from the centre upwards to the leading edge, just before it reaches the leading edge from the back a small 'separation bubble' is present. Between this separation bubble and the separation on the frontal surface the back flow reattaches just ahead of the leading edge.

The DUT-15-30 (figure 6.9(b)) is characterised by the same separation bubble on the back due to the circulation although it is moved slightly to the front. The separation on the upwind surface start earlier compared to the DUT-10-35, this creates more suction which makes it possible for the rear separation to move forward and is now located just on the leading edge.

For the DUT-20-25 it can be seen that on the downwind surface the streamlines are attached and that the separation bubble, still caused due to the circular flow, is moved to just in front of the leading edge. The separation on the upwind surface start again earlier which also leads to an increase in distance between the flow separation on the front and the separation bubble originating from the back flow.

Similar observation is done for the DUT-25-20. In this case the separation bubble originating from the circular flow is formed completely on the upwind side of the profile. However instead of reattaching afterwards it is found that between the separation on the front and the separation bubble vortices are present.

Finally for the two thickest profiles these same vortices are present, they only are stretched over a longer distance since the separation moves forward with the thickness.

So in general it can be concluded the drag reduces with increasing leading edge thickness due to a suction force which grows with increasing thickness, this is illustrated by looking at figure 6.7 (and in appendix E). The suction force yields a resulting force which can be decomposed a forward pointing force (canceling a part of the drag) and a upwards pointing force (lift force). From the streamlines around the leading edge it is clear that the growing of the suction peak goes together with forward moving of the separation point. The presence of a recirculation due to the circular flow in the wake which also moves forward with increasing leading edge thickness is rather unknown so far. It should be mentioned that these are 2D results and that the highly separated flow has strong 3D flow characters, therefore further investigation is required. Also is it doubtful that a RANS simulation can accurately determine the topology of the flow. The location where this recirculation cell originates is probably dependent on the the rear surface curvature. This would mean that in case this recirculation cell influences the drag coefficient it is invalid to state the part of the body which is fully emerged in the wake has no effect on the drag coefficient [Hoerner \(1965\)](#). Further investigation is required to make a clear statement on this.

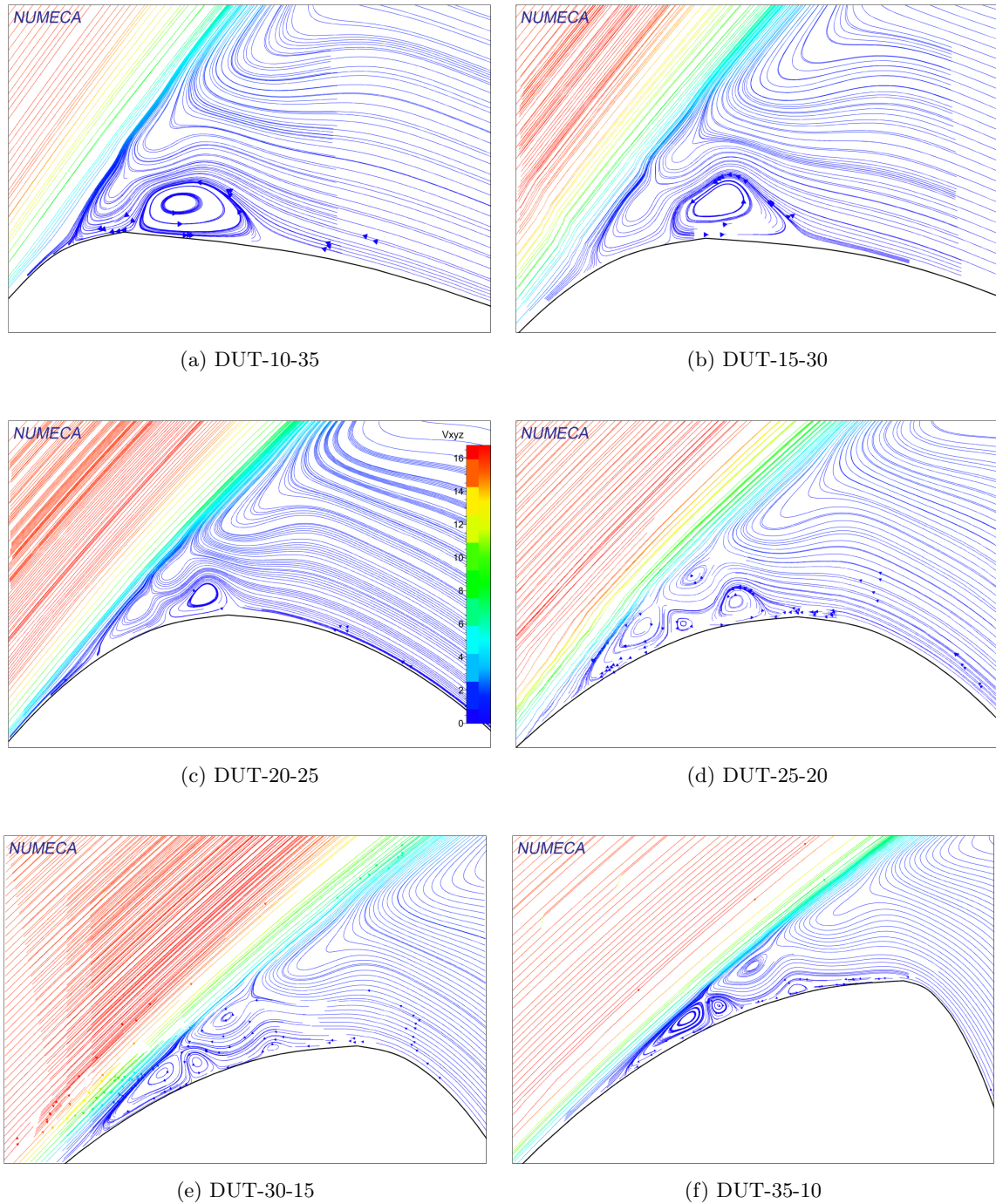


**Figure 6.9:** Streamlines near the leading edge for different profiles

---

## Chapter 7

---

# Comparison Experiments - CFD

In this chapter the results obtained from the wind tunnel experiments are compared to those obtained from the CFD simulations. No new results will be presented in this chapter and it is merely a comparison from earlier discussed results. First the DU91-W2-250 will be discussed base on the pressure distribution. Secondly the balance measurements from the other models are compared to the CFD. In the last section first the flat plate will be discussed to evaluate the difference over the entire angel of attack range. Later on the established relations between the lift and drag coefficient with respect to the leading edge thickness are discussed. The results presented in this chapter are all corrected for blockage since for the CFD no uncorrected results are available. This because no trustworthy results with solid boundary conditions are obtained as explained in the previous chapter.

### 7.1 DU91-W2-250

The DU91-W2-250 has the advantage over the designed models that it is equipped with pressure holes. This makes it possible to compare the pressure distribution determined from the CFD simulation with those from the wind tunnel measurement. Comparing the pressure distribution always gives better insight in what is happening instead of just the force coefficients. In figure 7.1 the pressure distribution at  $90^\circ$  angle of attack is given for both the wind tunnel facilities and the CFD computation. For the LTT and the CFD simulation a Reynolds number of 500 000 is used while the data of WindGuard is obtained at a Reynolds number of 600 000. For the base pressure it is chosen to represent the mean base pressure rather than the actual pressure at the upper side. There is not much difference between both since the pressure at the upper side is rather constant anyway but it makes it easier to compare them and to make a conclusion. For the lower surface no significant difference between the three pressure distributions is observed. The data from WindGuard only shows a less smooth result compared to the other two and this is probably due to the continuous turning rate making it difficult to capture a significant amount of vortex cycles at a certain angle. The upper

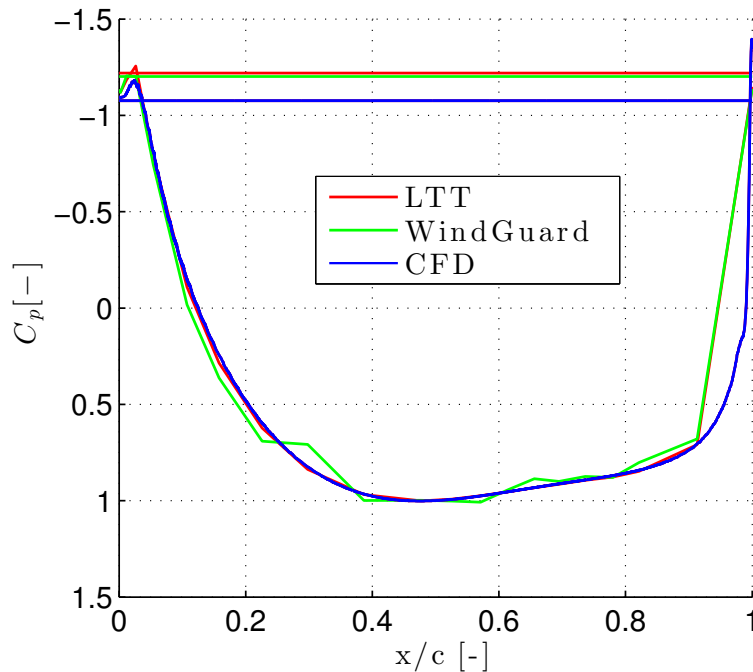


**Figure 7.1:** Corrected pressure distribution at  $90^\circ$  angle of attack according to LTT ( $Re = 5 \times 10^5$ ), WG ( $Re = 5 \times 10^5$ ) and CFD ( $Re = 6 \times 10^5$ ) for the DU91-W2-250 profile

surface shows a noticeable difference between the three pressure distributions. The pressure distribution of the LTT is the lowest followed by that of WindGuard which is only a little bit smaller. The base pressure obtained from the CFD simulation is the smallest. The reason for this smaller base pressure could be due to the chosen mesh in combination with the RANS flow solver. As shown earlier in section 6.1 this current mesh tends to produce a base pressure which is slightly too small but is chosen anyway because it simulates the leading edge the best.

## 7.2 DUT airfoils

In this section the force coefficients from the balance measurements are compared to the force coefficients obtained from the CFD computation. First the flat plate data will be compared with the experimental results over the entire measurement range. Later on the derived relation between the force coefficients and the leading edge thickness are compared.

### 7.2.1 Flat plate

In the previous chapter it is explained that for the flat plate the CFD computations are performed at various angles of attack to see how the lift and drag curves would behave. In

figure 7.2 the lift and drag coefficient is given according to the LTT and the CFD computation ( $Re = 1.5 \times 10^5$ ), WindGuard ( $Re = 6 \times 10^5$ ) and the ideal flat plate theory over the entire angle of attack range.

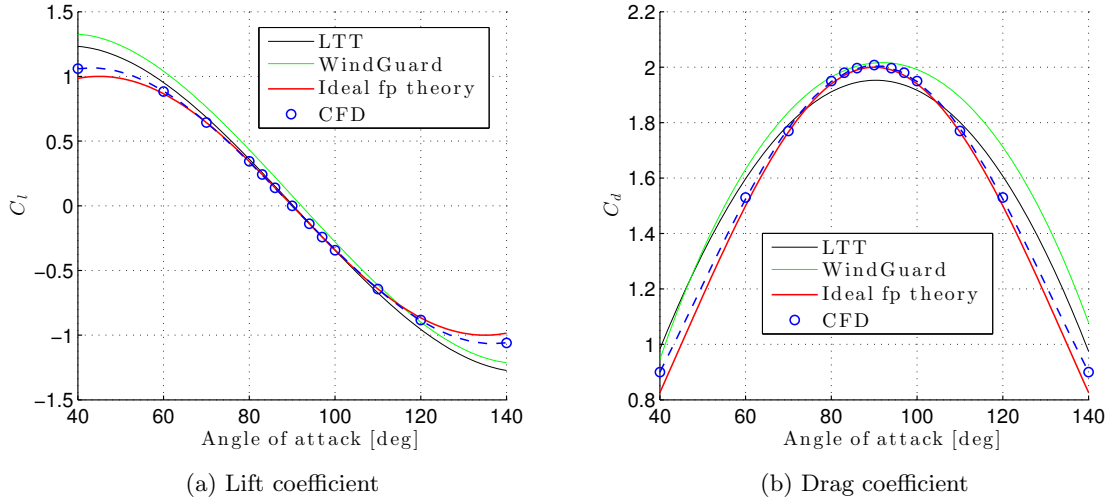


**Figure 7.2:** Lift and drag coefficient based on the wind tunnel measurements, Ideal flat plate theory and CFD

For the lift coefficient it can be seen that all cases are almost identical around  $90^\circ$  angle of attack, only a small offset ( $\approx 2^\circ$ ) in the WindGuard data is observed. However going to the end of the domain all the different results start to deviate from the ideal flat plate theory and also from each other. The CFD results stays the closest to the ideal flat plate theory while the two wind tunnel measurements deviate more strongly. A possible reason for the stronger deviation at the relative smaller angles of attack is presence of the stiffener at the back of the flat plate. It was assumed that when its fully emerged in the wake it would not have any influence but it might be that there is an influence on the force coefficients. This stiffener is necessary for the experiments to minimise the deflection and vibration of the flat plate while for the CFD this is not needed. For the drag coefficient the comparison is somewhat different. At  $90^\circ$  angle of attack it can be seen that it is the measurement from the LTT that is deviating the most from all the others which compare rather well. Near the end of the domain a similar behaviour can be seen as for the lift coefficient which again could be explained due to the stiffener. Why for the measurement of WindGuard the drag curve is not symmetrical around  $90^\circ$  (visible when looking at the coefficient at  $40^\circ$  and  $140^\circ$  angle of attack) could be explained due to the angle shift which is found from the lift coefficient.

### 7.2.2 Leading edge thickness vs $C_{d_{max}}$

Finally all the relations found so far that link the lift and drag coefficient to the leading edge thickness are compared. In figure 7.3 all the found relations are depicted (including the relation found by Timmer (Timmer, 2010)).

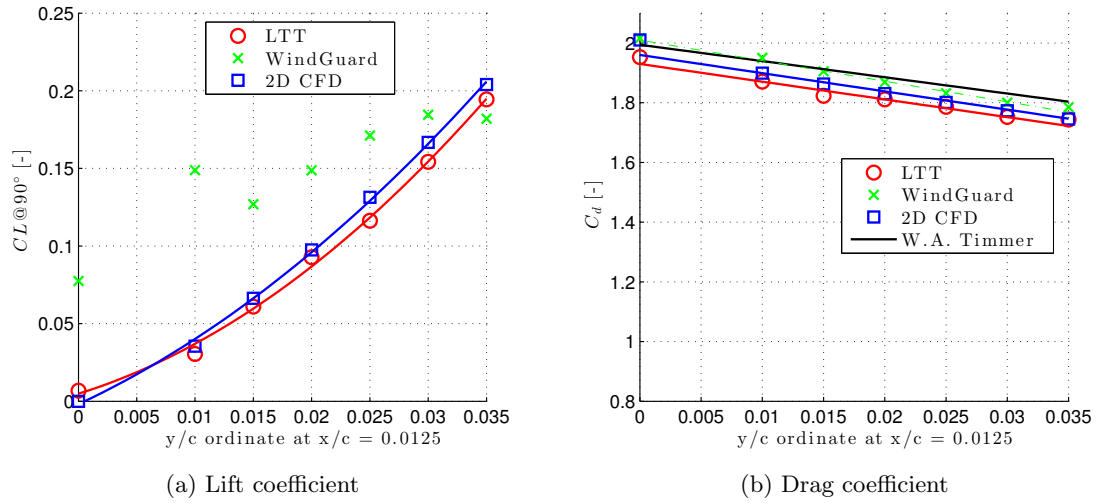


**Figure 7.3:** Lift and drag coefficient with respect to the leading edge thickness based on wind tunnel measurements and CFD

For the lift coefficient it can be seen that the measurements of WindGuard do not yield a relation between the lift coefficient at  $90^\circ$  angle of attack and the leading edge thickness. The measurements in the LTT and the CFD computation yield quadratic relations which are slightly different. According to the LTT measurement still a questionable lift coefficient is present for the plate while for the CFD computation this is not the case. With increasing thickness the lift coefficient increases faster according to the CFD and except for the flat plate all lift coefficient for the models are larger according to the CFD than compared to the LTT measurement. The deviations which are given for the WindGuard measurements are earlier attributed to the small forces which are hard to measure with their electronic balance system.

The maximum drag coefficient in relation to the leading edge thickness is given in figure 7.3(b) which demonstrates that for all cases a relation is found. Again it is found that the measurements from the LTT and the CFD computations match the best although in this case there is a constant offset. The slope with which the drag reduces with increasing leading edge thickness is almost identical but the values are shifted upwards. Furthermore, it can be seen that for both (LTT and CFD) the flat plate drag coefficient is higher than what the empirical relation would suggest. Similar observation was described by Lindenburg who gives stronger reduction in drag coefficient for very small leading edge radii (see figure 2.6). For the WindGuard measurement a much stronger decrease with increasing leading edge is found compared to the other cases.

An overview is given in table 7.1 where the maximum drag coefficient of the flat plate and the reduction with increasing leading edge thickness is summarized of all the tests and the simulation.

**Table 7.1:** Drag coefficient for the flat plate and drag reduction according to W.A. Timmer, LTT, WindGuard and CFD

	$C_d(y/c = 0)$	$\frac{dC_d}{d(y/c)}$
W.A. Timmer	1.994	-5.44
LTT	1.93	-5.94
WindGuard	2.01	-6.9
CFD	1.96	-6.1

So in general it can be concluded that the CFD computation and the wind tunnel measurement agree in a certain way. Best comparison is found between the LTT and the CFD computation. However, concerning the maximum drag coefficient of a flat plate it is WindGuard that compares the best with the CFD and the theory. A reason why overall the drag coefficient obtained by the LTT is so low could be due to an incorrect value for the Maskell correction factor, this is earlier indicated in chapter 2.



---

## Chapter 8

---

# Conclusion and Recommendations

In this research it has been investigated how the change of leading edge thickness influences the drag coefficient and the aerodynamic characteristics in general for airfoils under extreme high angles of attack. Especially near 90 degrees angle of attack where the maximum drag coefficient is reached. This chapter concludes the results of this research and presents some recommendations for further analysis.

### 8.1 Conclusion

A condition which is unique for turbine blade compared to airfoils designed for airplanes is that during start-up, stopping and standstill of the wind turbine, the blades experience very high angles of attack even beyond 90°. Being able to estimate the forces that act on the blades in these circumstances is valuable regarding the design and therefore investigated in this research. By means of experimental and computational analysis a conclusion is drawn regarding the effect of the leading edge thickness on the maximum drag coefficient which is experienced at 90° angle of attack.

Two wind tunnel experiments are conducted in two different wind tunnels which have the interesting characteristic of having the same height but a significantly different width (1.8 m and 2.75 m). This is of interest since testing at extreme high angle of attack goes together with a significant amount of blockage and having two wind tunnels with a different width it is also possible to make a statement on the blockage correction method.

For this investigation specially designed models are created to analyse the effect of the leading edge thickness. The parameter identifying the leading edge thickness is chosen to be the  $y/c$  ordinate at  $x/c = 0.0125$ . The models created will range from zero (flat plate) to a LE thickness of 0.035 and have a chord length of 0.20 meter. All trailing edges are similar to the flat plate such that only the effect of the leading edge is taken into account. Furthermore,

the existing DU91-W2-250 model is used which is equipped with pressure orifices making pressure measurement possible. These pressure measurements have the benefit over balance measurement to give more insight in the flow around the model and also concerning the blockage correction it is possible to determine the Maskell blockage factor ( $\theta$ ) based on the base pressure rather than on the aspect ratio (for an infinite span  $\theta$  is assumed to be 0.96).

The first wind tunnel test is conducted in the Low Turbulence Tunnel at the Delft Technical University. The main conclusions from the DU91-W2-250 and the designed models are summarized below:

- The Reynolds number has no effect on the force coefficients in the deep stall region,  $\alpha > 50^\circ$ .
- Maskell blockage correction factor ( $\theta$ ) based on base pressure is 0.71 for DU91-W2-250 at  $90^\circ$  angle of attack (0.96 is used in all cases which is based on infinite aspect ratio).
- The maximum drag coefficient of a flat plate is found to be 1.95.
- The drag reduction with leading edge thickness is determined to be:  $\frac{dC_d}{d(y/c)} = -5.94$
- The lift coefficient increases quadratic with the leading edge thickness going from 0.005 to 0.194

From the second wind tunnel test performed at WindGuard the following conclusions are drawn:

- Significant difference between pressure and balance measurement of the DU91-W2-250 in the deep stall region.
- The maximum drag coefficient of a flat plate is found to be 2.01.
- The drag reduction with leading edge thickness is determined to be:  $\frac{dC_d}{d(y/c)} = -6.9$
- The effect of a gap at one side of the model is negligible.

In addition to the wind tunnel test also a CFD simulation is performed get more insight in the reason why the drag reduces with increasing thickness. The main findings from the CFD simulation are given below:

- The maximum drag coefficient of the flat plate is found to be 2.01
- The drag reduction with leading edge thickness is determined to be:  $\frac{dC_d}{d(y/c)} = -6.1$
- An increase in leading edge thickness causing an increase in suction force which results in an increase in lift coefficient and a decrease in drag.

- From flow visualization it is concluded that separation occurs earlier for a thicker leading edge thickness

So in general this research has shown that the maximum drag coefficient decreases linearly with increasing leading edge thickness. This is caused by an increasing suction force at the leading edge which also justifies the increase in lift coefficient. The increase in suction force is due to earlier separation for increasing leading edge thickness and not because a thicker leading edge prepares the flow better to go around the object (Montgomerie, 1996)

## 8.2 Recommendations

Previously it has been explained to which extend the research question is answered with success. However there is a number of suggestions to be made in order to improve the current research and as a possible start for further analysis.

With respect to the wind tunnel tests a few improvements are possible which will lead to better results or in order to get better comparable results between both wind tunnel facilities. Equipping the models with pressure orifices such that not only balance measurements can be performed would be beneficial. Being able to do the pressure measurement on the models has some direct and indirect benefits. The first direct advantage of the pressure measurement is that measuring frequency is significantly larger when compared to the mechanical balance used in the LTT. This high measuring frequency is useful to determine the strouhal number. The ability of performing pressure measurements also results in secondary benefit which is that the model can be clamped at both sides. This in itself is also a recommendation since at WindGuard the model is clamped at both side while in the LTT this was not possible, therefore only at very low Reynolds numbers was tested. Although it is assumed that the Reynolds number has no influence on the force coefficients at high angle of attack it would be more correct to compare the two wind tunnel test if both the set-up and the testing conditions are similar. The availability of the pressure distribution would also make it possible to determine the Maskell correction factor based on the base pressure and uncorrected drag rather than on the aspect ratio. It has been shown in an example of the DU91-W2-250 that this might vary significantly. During the entire research  $\theta = 0.96$  is used for all correction. This because no pressure data was available for the models. However, an example of the DU91-W2-250 has shown that in the LTT a value of 0.7 should be used for  $\theta$  based on the base pressure at  $90^\circ$  angle of attack. An even better estimation of the  $\theta$  value is possible when pressure measurements are possible over the entire span of the profile.

CFD is used to obtain pressure distribution and perform flow visualisation which yielded important information concerning the effect of the leading edge thickness on the flow. Two important improvements on the current simulation would be: the use of solid boundary conditions and 3D simulation. It has been shown that that possibly a large boundary layer growth is present due to the large suction in the wake. In order to simulate the tunnel walls it will be important to accurately simulate this boundary layer growth. Furthermore, it is known that highly separated flow is characterised by 3D structures while in this research the

flow is simulated as 2D. Therefore if these both could be implemented in the simulation a comparison between the uncorrected wind tunnel test and the CFD can be performed, this then excludes any possible errors due to the correction. However, it is possible that with a simplified RANS simulation it is not possible to accurately simulate the 3D structures in the wake. A more time and computational demanding large eddy simulation simulation will become closer to the real situation.

Finally in addition to the already performed experiments it would be interesting to conduct some experimental flow visualisations around the leading edge to confirm the findings of the CFD flow visualisation. Given the small area where the effect of the leading edge is having a influence on the flow I would suggest that particle image velocimetry would be the best suited for this research. With oil visualisation it will be hard to detect the difference between the models.

Besides improvement on the current research some additional research can be recommended in order to extent the current relations. For example the effect of the maximum thickness and the location of the maximum thickness can be investigated. It is also possible that this maximum thickness and the thickness of the leading edge are related. Furthermore it can be evaluated how camber influences the maximum drag coefficient.

---

# Bibliography

- AGARD-336. *Wind tunnel wall corrections, In AGARDography 336*. North Atlantic Organisation, first edition, 1998.
- A.W. Bloy and D.G. Roberts. Aerodynamic characteristics of the naca 632-215 aerofoil for use in wind turbines. *Wind Engineering*, 17(2):67–75, 1993.
- Jerry M. Chen and Yuan-Chen Fang. Strouhal number of inclined flat plates. Technical report, National Chung-Hsing University, Taiwan, February 1996.
- A. Fage, A.RC.Sc, and F. C. Johanson. On the flow of air behind an inclined flat plate of infinite span. Technical report, The National Physical Laboratory, May 1927.
- R. Fail, J. A. Lawford, and R. C. W. Eyre. Low-speed experiments on the wake characteristics of flat plates normal to an air stream. Technical report, Ministry of Supply - Aeronautical research council, June 1957.
- J.E. Hackett and K.R. Cooper. Extension to maskell’s theory for blockage effects on bluff bodies in closed wind tunnel. *The Aeronautical Journal*, 105:409–418, 2001.
- S.F. Hoerner. *Fluid-Dynamic Drag*. Hoerner Fluid Dynamics, first edition, 1965.
- Md Naim Hossain. Computational Mechanics turbulence modeling, 2012. URL <http://naimhossain.blogspot.nl/2012/08/turbulence-modeling.html>.
- B. M. Jones. The measurement of profile drag by the pitot-traverse method. Technical report, ARC RM, January 1936.
- F. W. Landstra. Improved blockage correction for two-dimensional profiles in deep stall. Master’s thesis, Technical University Delft, August 2010.
- T. V. Lawson et al. Mean fluid forces and moment on cylindrical structures: Polygonal section with rounded corners including elliptical shapes. *ESDU 79026*, 1979.
- C. Lindenburg. Investigation into rotor blade aerodynamics: Analysis of the stationary measurements on the uae phase-vi rotor in the nasa-ames wind tunnel. Technical report, NASA, July 2003.
- B. Montgomerie. Drag coefficient distribution on a wing at 90 degrees to the wind. Technical report, ECN, Renewable Energy, February 1996.

- Numeca. *Fine<sup>TM</sup>/Open v2.12 (Including Openlabs) Flow integrated Environment*. Numeca International.
- Abdeen Mustafa Omer. Energy, environment and sustainable development. *Renewable and sustainable energy reviews*, 12:2265–2300, 2008.
- C Ostowari and D Naik. Post stall studies of untwisted varying aspect ratio blades with a naca 4415 airfoil section - part 1. *Wind Engineering*, 8(3):176–194, 1984.
- C Ostowari and D Naik. Post stall studies of untwisted varying aspect ratio blades with naca 44xx airfoil sections - part 2. *Wind Engineering*, 9(3), 1985.
- D. Satran and M.H. Snyder. Two- dimensional tests of ga(w)-1 and ga(w)-2 airfoils at angles-of-attack from 0 to 360 degrees. Technical report, Wind Energy Laboratory, Wichita State University, Kansas, USA, January 1977.
- F. Scarano. Experimental aerodynamics. Technical report, Delft University of Technology, February 2012.
- David A. Spera. Models of lift and drag coefficients of stalled and unstalled airfoils in wind turbines and wind tunnels. Technical report, Jacob Technology, Inc., Cleveland, Ohio, Oktober 2008.
- W. A. Timmer. Aerodynamic characteristics of wind turbine blade airfoils at high angles-of-attack. Technical report, Delft University of Technology, 2010.
- Viterna, Larry A., and David C. Janetzke. Theoretical and experimental power from a large horizontal-axis wind turbines. *Fifth Biennial wind energy conference and workshop, Washington DC*, 2:265–280, 1981.

---

# Appendix A

---

## AERODAS

The post stall drag equation according to Spera is given by the following equation.

$$CD2 = CD1max + (CD2max - CD1max) * \sin\left(\frac{90 - \alpha}{90 - ACD1} \cdot 90\right) \quad (A.1)$$

Spera models the post-stall regime by a sine curve that achieves its maximum at 90° and intersects the pre-stall drag curve at coordinates (ACD1, CD1max), this can be seen in figure 2.7(b). Using this formula for determining the post-drag results in false values for the drag coefficient. This can be observed by determining the drag coefficient at an angle of attack equal to ACD1. Filling in this in equation A.1 results in a CD2 equal to CD2max while it should be CD1max as can be seen in figure 2.7(b).

A new expression for CD2 in this region is determined using the following approach. As Spera it is assumed that the post-stall drag can be simulated by a sine function. Furthermore it is also assumed that this function finds its origin at the point (ACD1, CD1max). The general sine function then has the following form.

$$y = a \cdot \sin(b(x - ACD1)) + CD1max \quad (A.2)$$

The parameters (a and b) can now be determined using the following information:

- The drag reaches its maximum at 90 degrees  $\Rightarrow f(90) = CD2max, f'(90) = 0$ .
- At ACD1 the drag equals CD1max  $\Rightarrow f(ACD1) = CD1max$ .

This results in the following expression for the post-stall drag coefficient.

$$CD2 = CD1max + (CD2max - CD1max) \cdot \sin\left(\frac{90}{90 - ACD1} \cdot \frac{\pi}{180} \cdot (\alpha - ACD1)\right)$$

$$(A.3)$$

CD1max and ACD1 are known from the pre-stall domain and the maximum drag coefficient can be determined according to the following equation.

$$CD2max = G1[t/c] * G2[AR] \quad (A.4)$$

Where G1 and G2 are two empirical relations, which are functions of airfoil thickness (t/c) and the airfoil's aspect ratio (AR) respectively.

$$G1 = 2.30 \exp\{-[0.65(t/c)]^{0.90}\} \quad (A.5a)$$

$$G2 = 0.52 + 0.48 \exp[-(6.5/AR)^{1.1}] \quad (A.5b)$$

The effect of the aspect ratio and the thickness is illustrated in figure A.1 where the obtained data from the AERODAS model is compared to data sets of various airfoils. It can be seen that the data sets used for the infinite aspect ratio airfoils are very inconsistent. Values well above 2 are found which is assumed to be the theoretical maximum. Besides this it is also observed that for similar thickness ratios also relative low values are present. The uncertainty in the data sets could affect the credibility of the AERODAS model since it is base on these data sets.

For determining the lift coefficient not equal to the maximum lift coefficient Spera established formulas for different regions depending upon the angle of attack. To obtain the lift coefficient at 90° the following formulas are used which are applicable between ACL1 and 92 degrees.

$$CL2 = -0.032(\alpha - 92) - RCL2 * \left(\frac{92 - \alpha}{51}\right)^{N2} \quad (A.6a)$$

$$RCL2 = -0032(41 - 92) - CL2max = 1.632 - CL2max \quad (A.6b)$$

$$N2 = 1 + CL2max/RCL2 \quad (A.6c)$$

Where

RCL2 reduction from extension of linear segment of lift curve to CL2max

N2 exponent defining the shape of lift curve at CL2max

To determine the lift coefficient using the given equation the maximum lift coefficient is required. This is defined in a similar way as the maximum drag coefficient. So at 41° the lift coefficient is given as an empirical function of the airfoil thickness and aspect ratio:

$$CL2max = F1[t/c] * F2[AR] \quad (A.7)$$

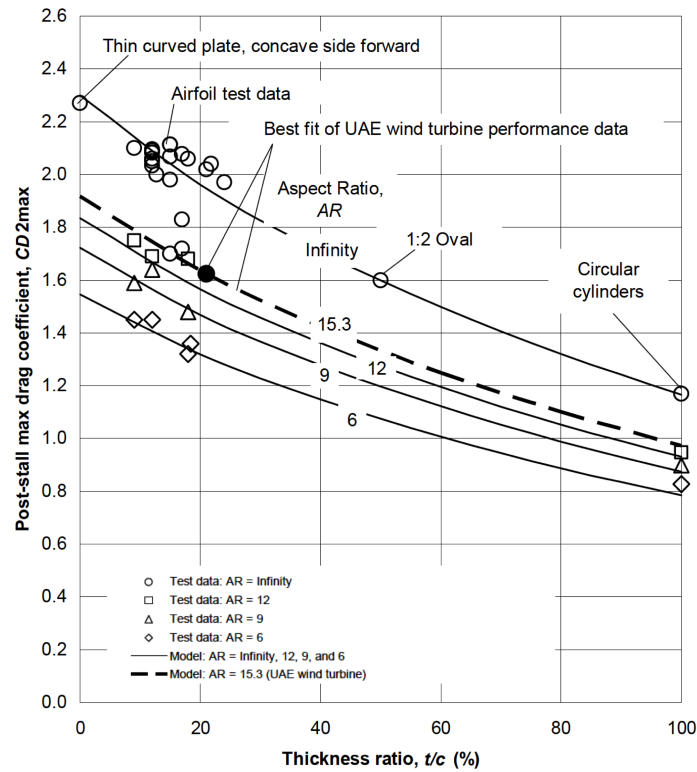


**Figure A.1:** AERODAS max drag coefficient for various airfoil thickness and AR Spera (2008)

These two empirical relations are again based on different sets of test data resulting in the following expressions.

$$F1 = 1.19[1 - (t/c)^2] \quad (\text{A.8a})$$

$$F2 = 0.65 + \exp[-(9/AR)^{2.3}] \quad (\text{A.8b})$$

Combining these equation the post-stall lift coefficient is determined. In figure A.2 the post-stall lift coefficient is illustrated for different aspect ratios.

At 90 degrees it can be seen that the AERODAS model slightly underestimates the lift coefficient and that the aspect ratio hardly has any influence. At 41° it can be seen that the effect of the aspect ratio becomes more significant. Here the AERODAS model gives an insufficient accurate result for an infinite aspect ratio where for smaller aspect ratio the result is comparable to the test data. This mismatch at high aspect ratio will result from the 'N2' exponent which defines the shape at CL2max. N2 depends upon CL2max which is determined by equation A.8. It is plausible that a different empirical relation, based on the larger data set, for equation A.8b could improve the model for higher aspect ratios.

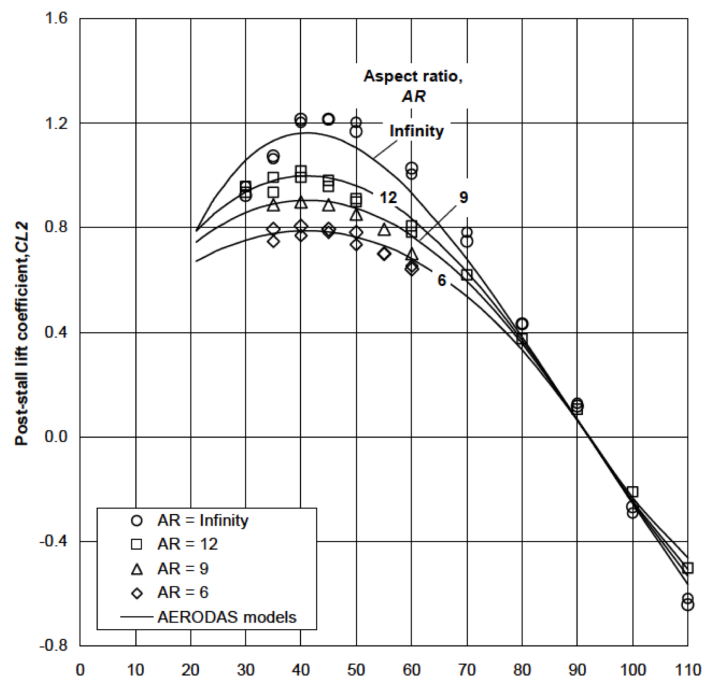


Figure A.2: post-stall lift coefficient for different aspect ratios Spera (2008)

---

## Appendix B

---

### Maskell correction factor

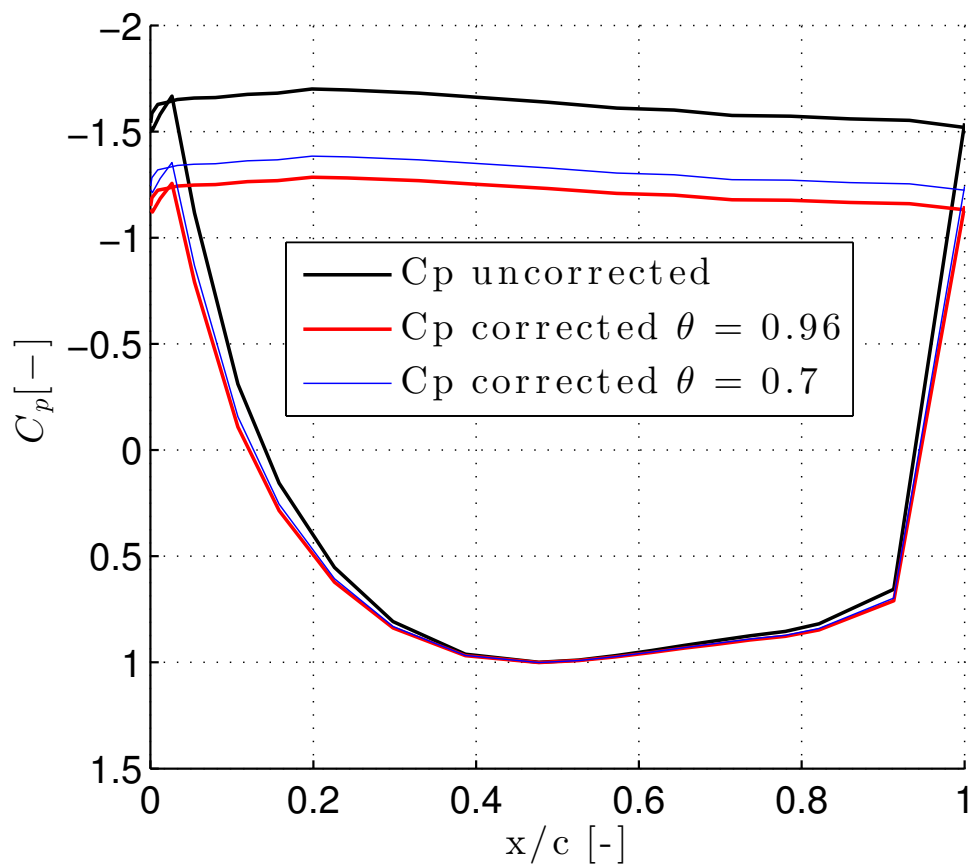


**Figure B.1:** Effect of the Maskell correction factor on the Pressure coefficient of the DU91-W2-250 at an AOA of  $90^\circ$ ,  $Re = 5 \times 10^5$

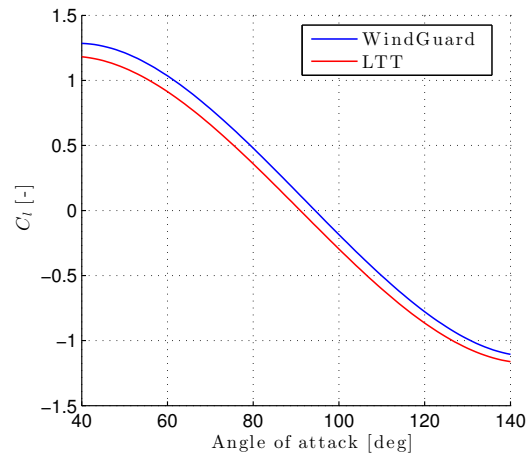


---

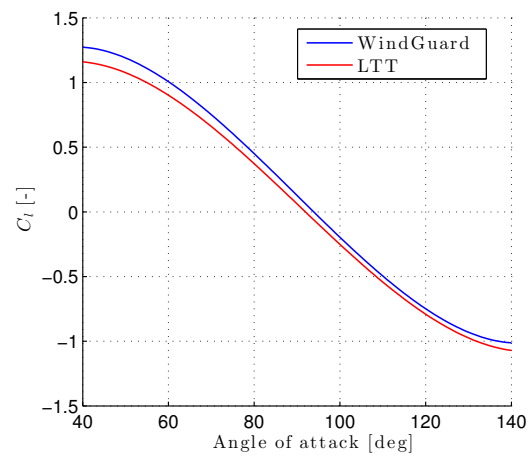
# Appendix C

---

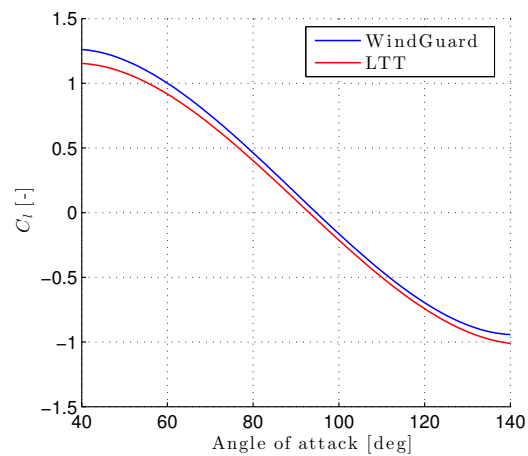
## Windguard



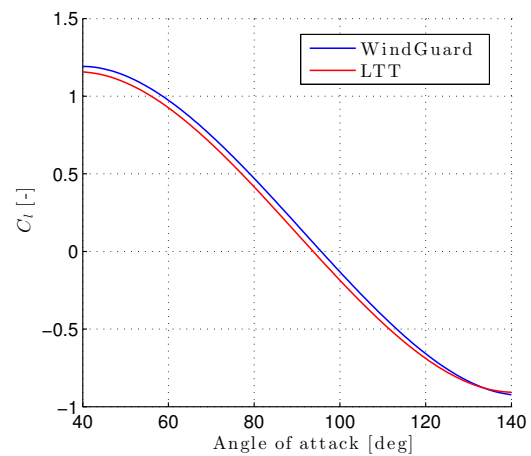
(a) DUT-10-35



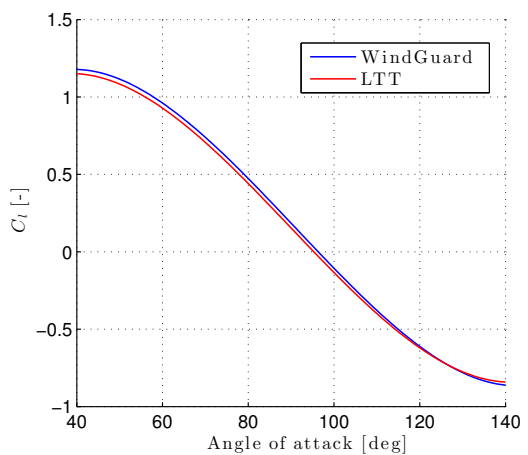
(b) DUT-15-30



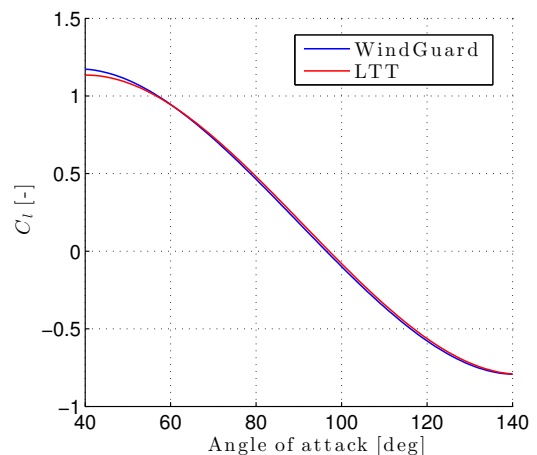
(c) DUT-20-25



(d) DUT-25-20

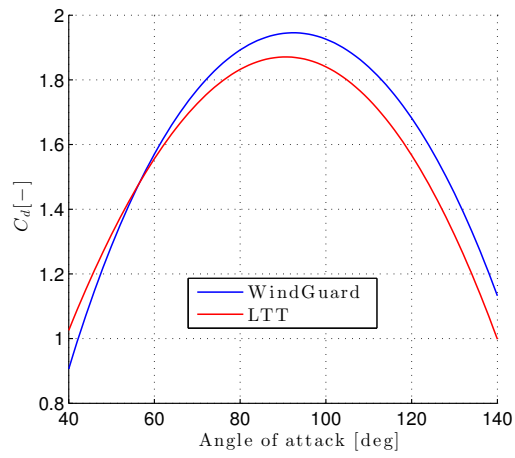


(e) DUT-30-15

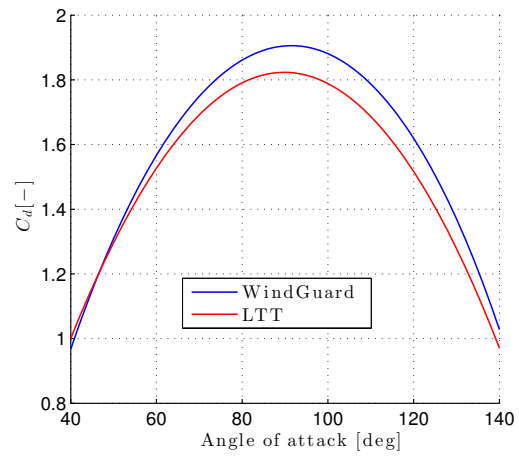


(f) DUT-35-10

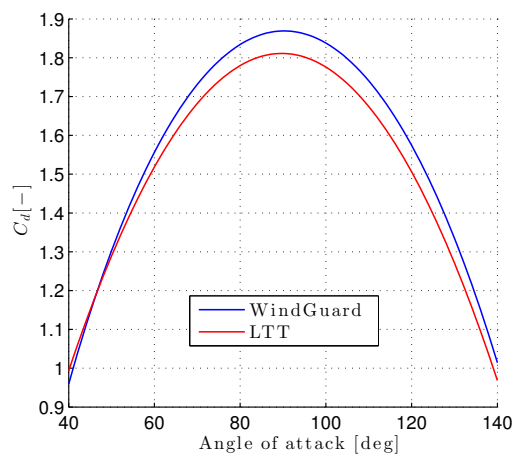
**Figure C.1:** Lift coefficient for all DUT airfoils from WG ( $Re = 6 \times 10^5$ ) and LTT ( $Re = 1.5 \times 10^5$ )



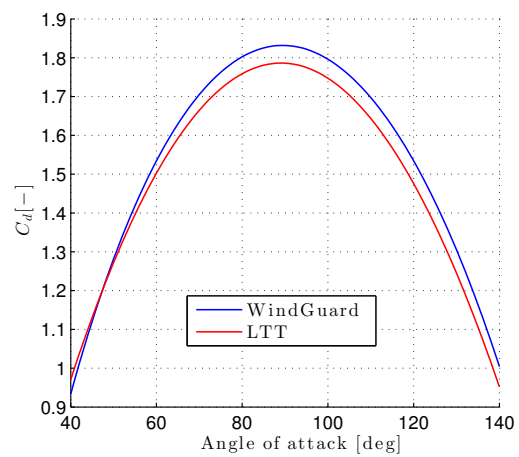
(a) DUT-10-35



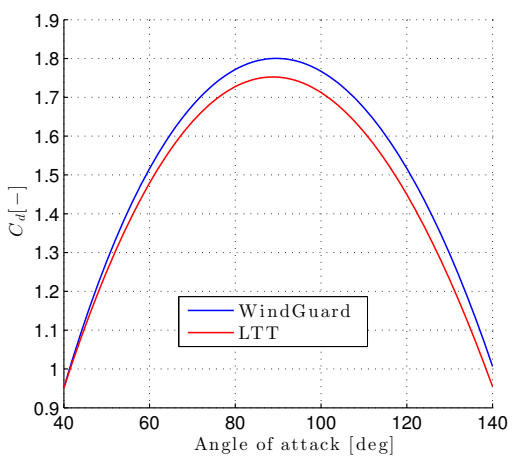
(b) DUT-15-30



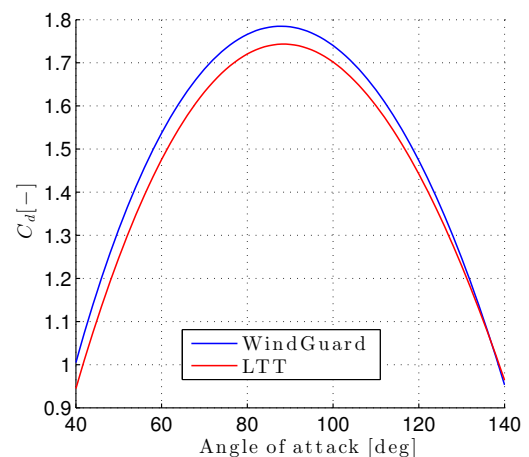
(c) DUT-20-25



(d) DUT-25-20

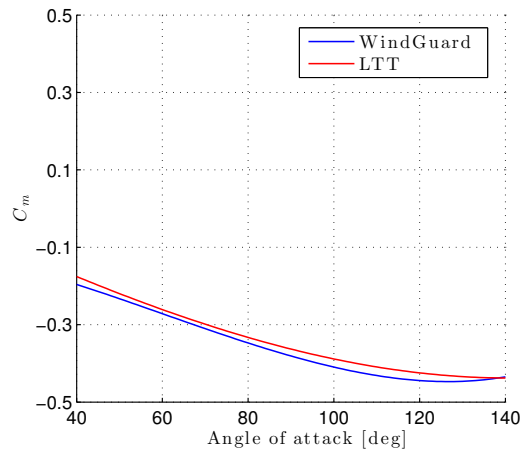


(e) DUT-30-15

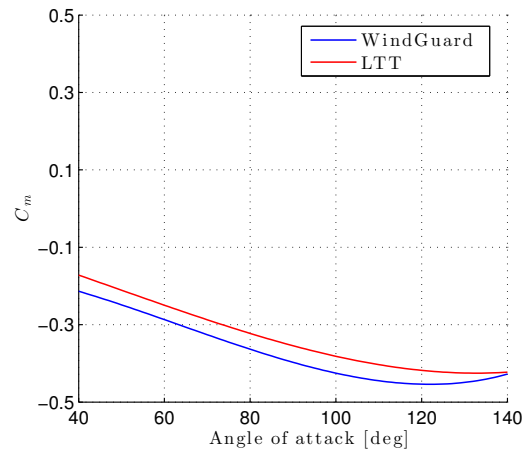


(f) DUT-35-10

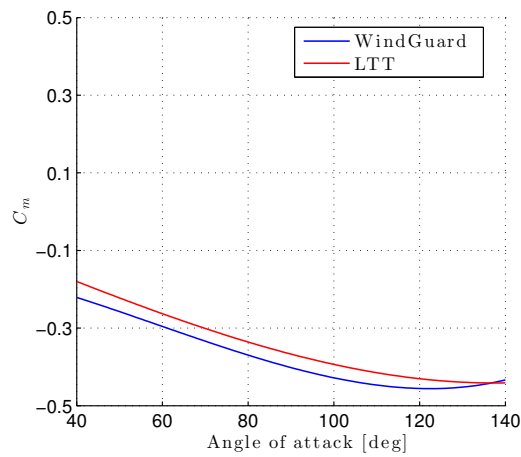
**Figure C.2:** Drag coefficient for all DUT airfoils from WG ( $Re=6 \times 10^5$ ) and LTT ( $Re=1.5 \times 10^5$ )



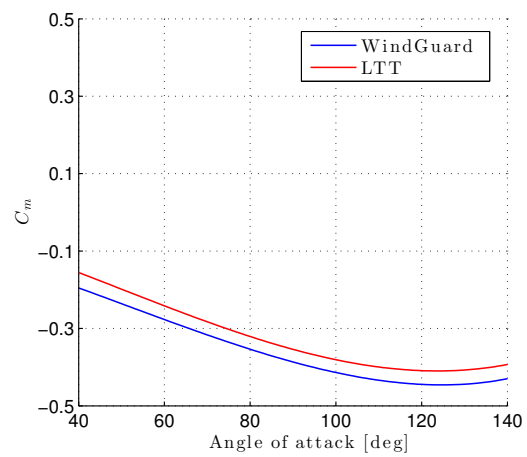
(a) DUT-10-35



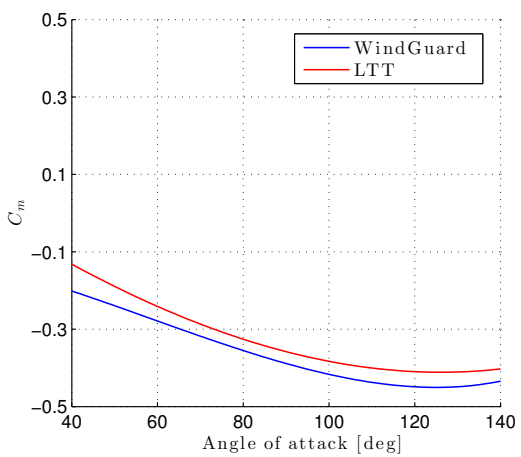
(b) DUT-15-30



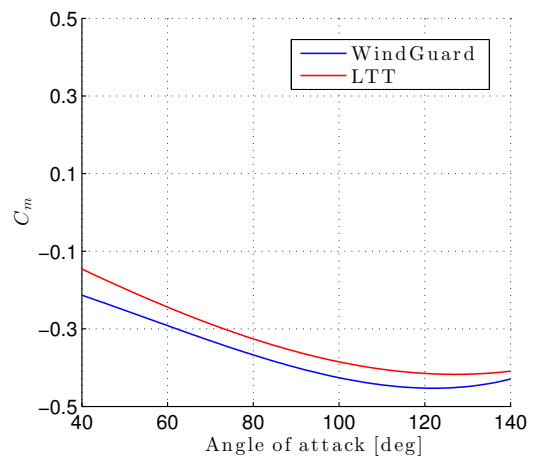
(c) DUT-20-25



(d) DUT-25-20



(e) DUT-30-15



(f) DUT-35-10

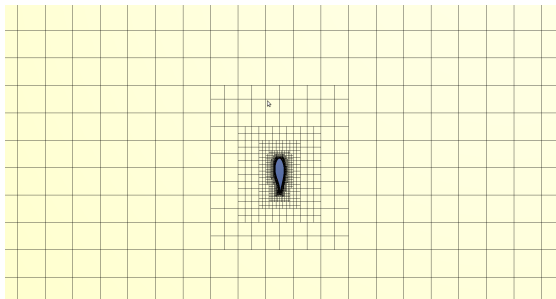
**Figure C.3:** Moment coef. for all DUT airfoils from WG ( $Re=6 \times 10^5$ ) and LTT ( $Re=1.5 \times 10^5$ )

---

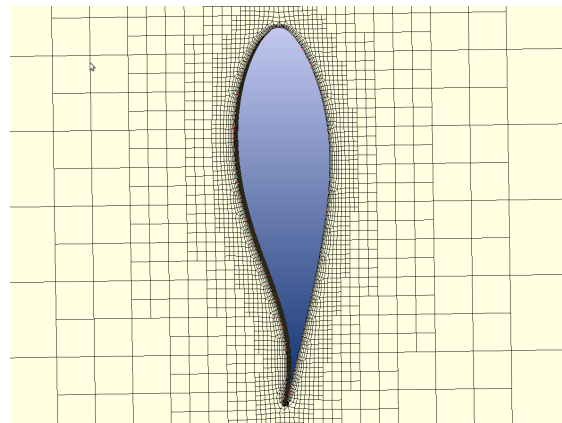
# Appendix D

---

## Meshes

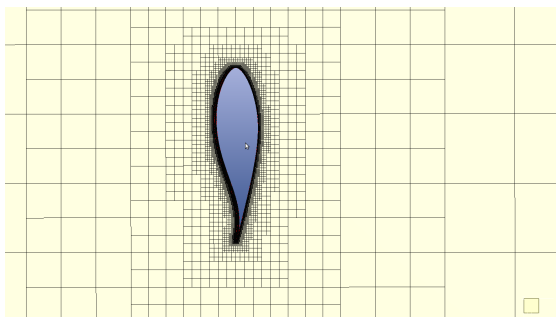


(a) Mesh 1

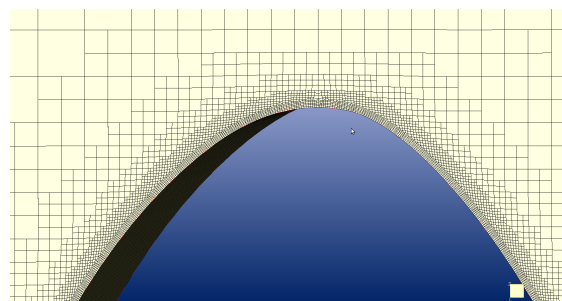


(b) Mesh 1

**Figure D.1:** Coarse mesh



(a) Mesh 2



(b) Mesh 2

**Figure D.2:** Medium mesh

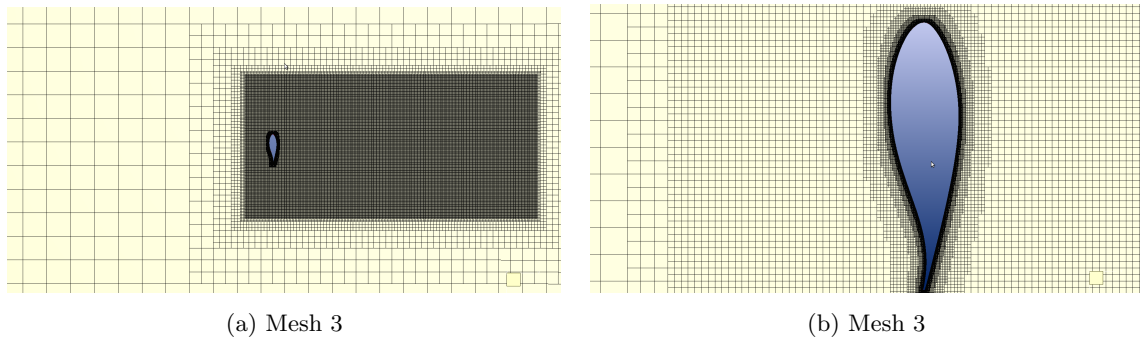


**Figure D.3:** Mesh with wake refinement

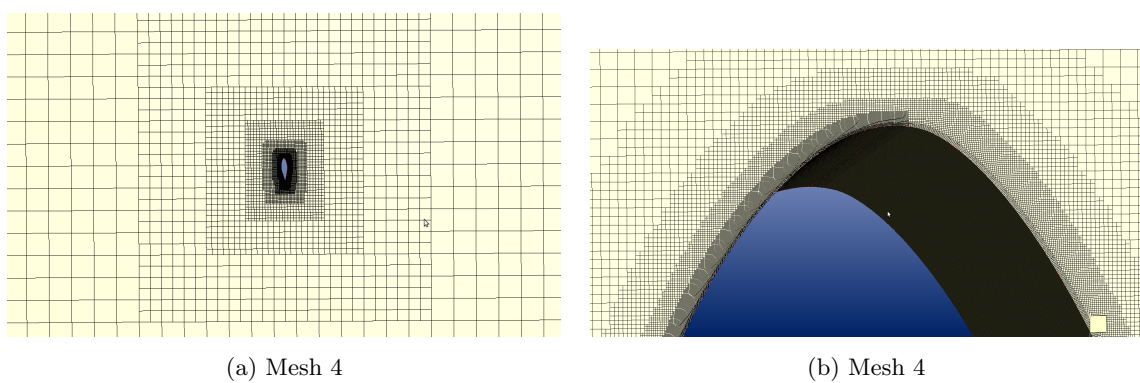


**Figure D.4:** Mesh 4

---

# Appendix E

---

## Pressure along surface

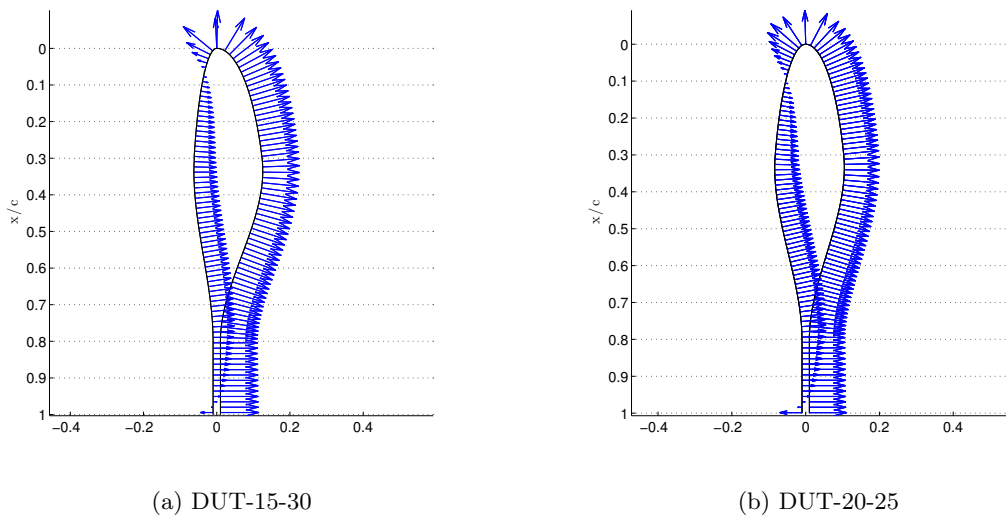


**Figure E.1:** Pressure distribution along the surface contour,  $Re = 1.5 \times 10^5$

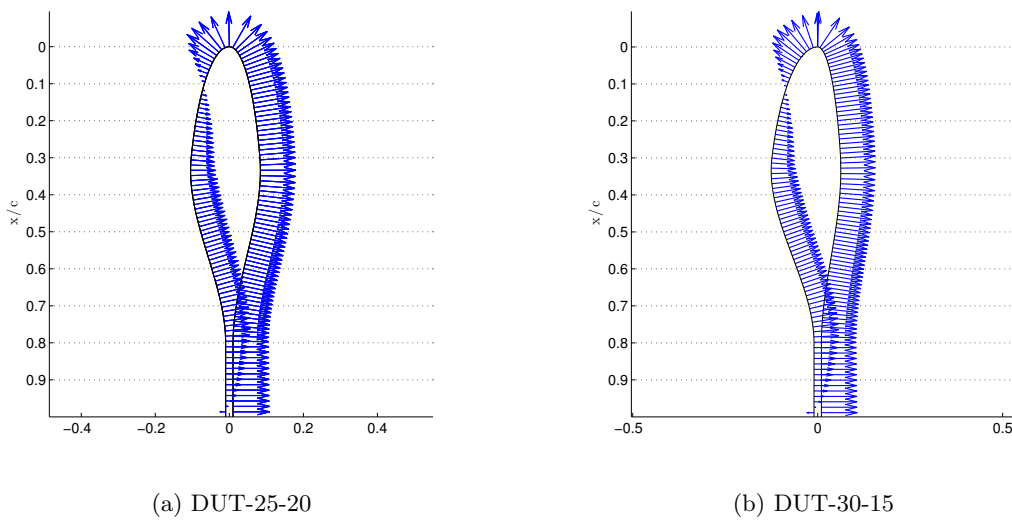


**Figure E.2:** Pressure distribution along the surface contour,  $Re = 1.5 \times 10^5$



